Heterogeneous vortex dynamics in high temperature superconductors

Feng Yang

ÉCOLE POLYTECHNIQUE
ParisTech

Thèse pour obtenir le grade de

DOCTEUR DE L'ÉCOLE POLYTECHNIQUE

Specialité : Physique

par

Feng YANG

Heterogeneous vortex dynamics in high temperature superconductors

Soutenue le 18 juin 2009 devant le jury composé de :

Gilles Montambaux	*Président*
Rinke J. Wijngaarden	*Rapporteur*
Alain Pautrat	*Rapporteur*
Takasada Shibauchi	*Examinateur*
Julien Bobroff	*Examinateur*
Kees van der Beek	*Directeur*

Thèse préparée au Laboratoire des Solides Irradiés,
Ecole Polytechnique, 91128 Palaiseau, France.

To my parents ...

Remerciements

Je tiens à remercier Guillaume Petite et Martine Soyer, pour leurs accueils chaleureux et leurs encouragements constants pendant toute la durée de la réalisation de cette thèse au Laboratoire des Solides Irradiés (LSI, CEA-CNRS-Ecole Polytechnique, UMR 7642) où ils président. J'exprime mes sincères remerciements à Rinke J. Wijngaarden et Alain Pautrat qui ont accepté d'être mes rapporteurs, ainsi qu'à Gilles Montambaux, Takasada Shibauchi, Julien Bobroff et Kees van der Beek, d'avoir accepté de faire partie de mon jury de thèse.

Marcin Konczykowski, chef du groupe "supraconductivité et matériaux nanostructurés" au LSI jusqu'en avril 2009, je te remercie pour ton aide et tes conseils précieux dans la réalisation de ma thèse, ainsi que pour tes efforts d'animation de notre groupe dont j'ai bénéficié.

Kees van der Beek, mon directeur de thèse, je te suis reconnaissant de m'avoir enseigné les techniques de mesures physiques, et la physique de vortex, et de m'avoir fait partager ta vision de la recherche scientifique.

Tout au long de cette thèse, j'ai bénéficié d'un environnement de collaboration scientifique de proximité et internationale. En voici un aperçu chronologique :

Mon premier contact avec la magnéto-optique se fait par Iryna Abal'osheva, de l'Institut de Physique à Varsovie (Académie des Sciences de Pologne), pendant sa visite au LSI au sujet d'un film magnétique. Piotr Gierlowski, membre de ce même institut, a élaboré les masques de nickel, éléments indispensables pour créer la structure "canaux" par l'irradiation aux ions lourds.

Les échantillons de *BSCCO* sur lesquels j'ai travaillé sont fournis par Peter H. Kes et Ming Li, du laboratoire Kamerlingh Onnes, de l'Universiteit Leiden, Pays-Bas. Le travail présenté en Chapitre 4 de ce manuscrit est à l'initiative de Yuji Matsuda et Takasada Shibauchi, de l'Université de Kyoto. Le monocristal *YBCO* de haute qualité, utilisé dans cette étude, est fourni par Bogdan Dabrowski, de Northern Illinois University.

Comment ne pas remercier deux chercheurs de l'Unité Mixte de Physique CNRS/Thales (UMR 137) : Rozenn Bernard et Javier Briatico? C'est grâce à leur aide précieuse en photolithographie que le courant a enfin pu être injecté correctement dans les monocristaux de *BSCCO* irradiés.

Tatiana Taurines, élève-ingénieur de Supélec, a réalisé des mesures des magnéto-

optiques différentielles pour moi sur les cristaux *BSCCO "24-4"*, *BSCCO "iv"*, et *BSCCO "17"* pendant son stage de $2^{ème}$ année d'ingénieur alors que j'étais occupé à la rédaction de ma thèse. Une partie des images magnéto-optiques présentées dans le Chapitre 5 de ce mémoire sont les fruits de son travail. C'est plus tard[1] que je me suis rendu compte de l'importance des mesures que Tatiana Taurines a réalisées. Comme promis, je lui ferai parvenir ce manuscrit. Je lui exprime mes sincères remerciements pour ses mesures.

En quelques années, je suis passé du statut d'étudiant insouciant à celui de doctorant préparant sa soutenance. Cette expérience m'inspire ces quelques réflexions :

1. Il ne faut pas laisser traîner une chose trop longtemps.
   Peut-être on peut inspirer de vivre chaque jour comme le dernier jour?

2. "Fail to plan is to plan to fail".

3. Comment transformer les idées émanant de "chercheur-amateur" par l'approche d'un "chercheur-confirmé"?
   Souvent un amateur est très libre dans sa pensée et il émet des idées intéressantes mais souvent fausses ou simplistes. Peut-être 1 sur 10 peut franchir la première étape de questionnement, et mérite d'être étudiée avec plus de soin. A partir de ce moment là, c'est l'approche standard et rigoureuse qu'il faut employer pour l'examiner. Je suis encore un débutant et pour moi, il y a encore un long chemin à faire pour mériter la qualification de "chercheur-confirmé".

Je remercie à Travis d'avoir relu une partie de ce mémoire et corrigé mes fautes d'anglais. Je dois à Kees son aide précieuse dans différentes phases de rédaction de ce manuscrit. Panayotis, je pense à te retrouver bientôt au LSI et je te souhaite beaucoup de bonnes choses pour toi. Je remercie à tous les membres du LSI qui ont contribué à une bonne ambiance et une convivialité d'y travailler.

Mes remerciements vont également à tous mes amis qui se trouvent en dehors du laboratoire : à mes amis de promotion (Fatima, Alix, Julien, Olivier, Thibault, Nicolas, Johannès et Eric) avec qui nous avons laissé nos traces en France, en Espagne, en Chine, et bientôt on fera la route de la soie? A ma communauté chinoise à qui j'ai toujours la joie de penser (pas seulement pour la douceur de sa cuisine) : WANG Minmin, REN Jizhao, WU Han, HE Mi, ZHOU Bing, YU Linwei, YU Guosheng, ... aussi à mes amis chinois qui ne se trouvent pas ou plus sur le plateau : ZHANG Jin, HUO Jie, LI Yuan,

[1] J'ai en effet remarqué que les trois faits suivants sont cohérents et se soutiennent mutuellement : (1) les plots irradiés à basses températures résistent plus au champ magnétique; (2) la résistance de l'échantillon de *BSCCO* (contenant les plots irradiés) est linéaire; (3) l'imagerie de circulation du courant a montré que le courant contourne les plots irradiés. A haute température (proche de T_c), la situation est exactement inverse, et cela est également confirmé par toutes les mesures (magnéto-optique différentielle avec modulation en champ et la non-linéarité de la résistance à ce régime proche de T_c).

JIAO Chenyu, HE Yuchan, ZHOU Feng, ZHENG Jin, TAN Xiaolu, XIA Lian, ZHOU Guodong, CHEN Huayi, JIAO Ying, JIN Ming, ... à mes amis avec qui je peux oublier la barrière linguistique et culturelle : Ermias, Giulia, Pedro et Raffaella, et à tous les autres que je n'ai pas mentionné ici.

Je tiens à remercier personnellement Roland Sénéor pour son soutien sans faille, à Christoph Kopper pour ses encouragements et à Madame BAI Gang pour ses conseils avisés.

Ma famille d'accueil française m'a toujours soutenu. Je la remercie du fond du cœur.

Je suis reconnaissant envers mon petit frère Tao resté en Chine et qui a rempli une partie de mon rôle pendant mon absence. Je dédie cette thèse à mes parents qui m'ont tant donné.

Cette thèse est financée par le CEA-Saclay sous le contrat CFR-CEA.

Feng YANG (feng.yang@polytechnique.edu)

Contents

Chapter 1

Introduction

Superconductivity is a phenomenon occurring in certain materials at low temperatures, characterized by the absence of electrical resistance and the exclusion of magnetic fields. A superconductor acts as a *perfect conductor* and a *perfect diamagnet*.

Superconductivity was discovered in 1911 [1] by the Dutch physicist Heike Kamerlingh Onnes (1853 - 1926), who had succeeded in liquefying helium in 1908 at a temperature of 4.2 K. Performing low temperature experiments with liquid helium, he observed that certain metals, such as Hg, Pb, completely lose their electrical resistance below the critical temperature T_c (order of a few degrees in Kelvin).

22 years later, in 1933, Walther Meissner (1882 - 1974) and Robert Ochsenfeld (1901 - 1993) [2] discovered that below the superconducting transition temperature T_c, tin and lead specimens became perfectly diamagnetic, i.e., the magnetic field is completely expelled from the interior of the superconductor. This effect is distinct from zero resistance and is called the Meissner effect.

In 1957, John Bardeen, Leon Cooper, and Robert Schrieffer [3] proposed a microscopic theory of superconductivity (BCS theory): the electronic system becomes unstable with respect to the formation of *electron pairs*, called the *Cooper pairs*, below the critical temperature. These *Cooper pairs* form a coherent macroscopic quantum state. This macroscopic quantum state is refereed to the superconducting condensate.

High-temperature superconductivity was discovered in 1986 in $La_{2-x}Ba_xCuO_4$ [4]. A considerable number of the materials, such as $YBa_2Cu_3O_{7-\delta}$ (*YBCO*) [5] and compounds of the $Bi_2Sr_2Ca_nCu_{n+1}O_{2n+6-\delta}$ (*BSCCO*) and $Tl_2Ba_2Ca_nCu_{n+1}O_{2n+6-\delta}$ families [6], are in the superconducting state at temperatures above the boiling point of liquid nitrogen (77 K or -196 °C). In this thesis, we will consider the electrodynamic properties of two high T_c superconductors $YBa_2Cu_4O_8$ and $Bi_2Sr_2CaCu_2O_{8+\delta}$.

The ability to use relatively inexpensive and easily handled liquid nitrogen for cooling has increased the range of practical applications of superconductivity. For example, the development of cryogenic techniques has allowed the world's first superconductor power transmission cable system, based on *YBCO*, to be integrated in a commercial power grid in Holbrook, New York, United States in June 2008. Superconductor cables can transport much more current than traditional cables and can transport electricity without any energy loss along the cable below the critical temperature (in this case at -200°C) since the electrical resistance is zero.

1.1 Superconductivity as a thermodynamic state

Flux exclusion from superconductors cannot be explained only by zero resistance (Figure 1.1). Suppose that one has two ellipsoid samples: one of which becomes a perfect conductor when cooled below its critical temperature, T_c, and the other becomes a superconductor when cooled below T_c. One finds that when the two specimens are cooled in a magnetic field, the superconductor behaves differently than the perfect conductor. A superconductor expels the magnetic flux while a perfect conductor retains the magnetic flux.

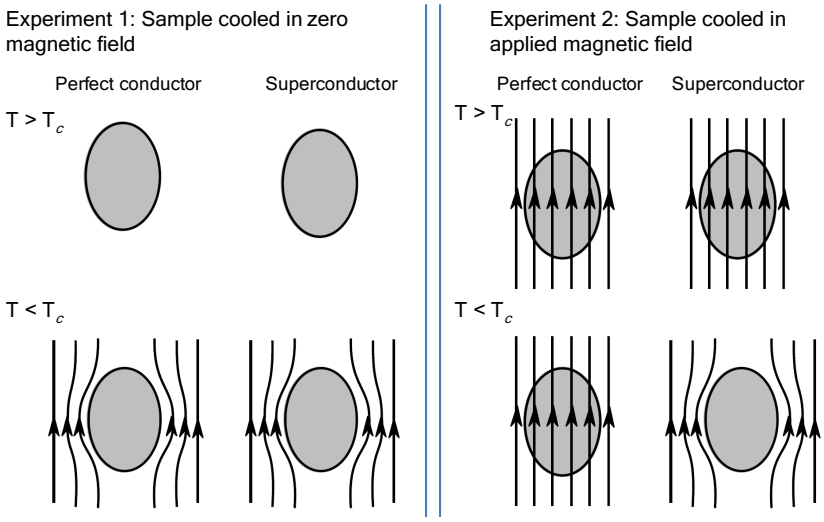

Figure 1.1: A superconductor does not behave as a perfect conductor.

The existence of such a reversible *Meissner effect* implies that *superconductivity* is a *thermodynamical state* which does not depend on previous history. Superconductivity is suppressed by a critical magnetic field H_c, which is related thermodynamically to the

free-energy difference between the normal and superconducting states at zero magnetic field, the so-called condensation energy of the superconducting state. If we denote f_n and f_s the Helmholtz free energies per unit volume in zero magnetic field in normal and in superconducting states respectively, the *thermodynamical critical field* H_c is determined by: $\mu_0 H_c^2/2 = f_n(T) - f_s(T)$. From experiments performed on superconducting metals, it has been found that: $H_c(T) \propto H_c(0)[1-(T/T_c)^2]$.

Since the transport current generates a magnetic field in the superconductors, the existence of a critical magnetic field H_c implies that there also exists a critical current density j_c. However this j_c is not what limits the usefulness of technical superconductors. Researchers on applied superconductivity aim to obtain superconducting materials with high critical temperature, high critical magnetic field and high critical current density. Ideally, the material should be easily manufactured in industry.

1.2 Magnetic properties for superconductors

1.2.1 Magnetization curves for type-I and type-II superconductors

Since the magnetic field is excluded completely from the interior of a superconducting sample (Figure 1.1) until the applied magnetic field exceeds its critical field value H_c, we may expect that the magnetization curve for a superconductor would be the following as shown in Figure 1.2:

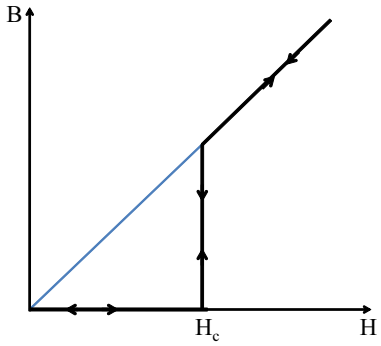

Figure 1.2: Reversible magnetization curve for a Type-I superconductor.

Many superconducting elements' magnetic properties obey the behavior showed in Figure 1.2 and these are called the type I superconductors.

Most superconductors, including the high-T_c superconductors and superconducting alloys, behave differently. There are two critical magnetic fields H_{c1} and H_{c2}. The magnetic field is completely expelled when $H < H_{c1}$ and only partially expelled when $H_{c1} < H < H_{c2}$ (Figure 1.3).

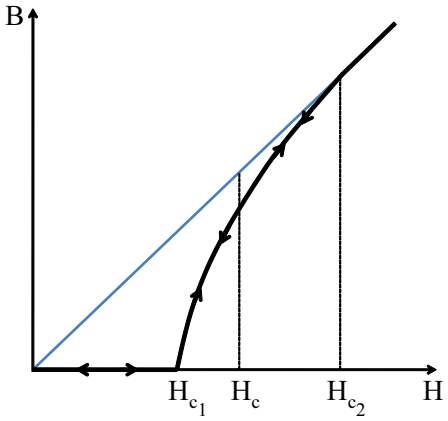

Figure 1.3: Reversible magnetization curve for a Type-II superconductor.

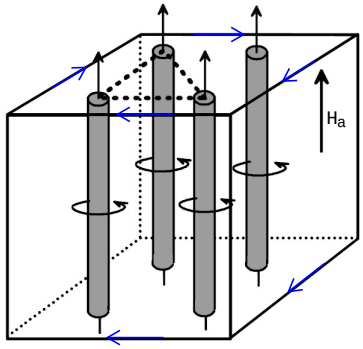

Figure 1.4: The flux quantum passes through the core of each vortex surrounded by supercurrents. The arrows along the edges indicate the surface screening current flow.

In a type-II superconductor, the magnetic field penetrates the bulk as quantized flux lines: each flux line, represented by the cylinders in Figure 1.4, corresponds to one *flux quantum*, of $\phi_0 = h/2e$. Its numerical value in *cgs* units is: $\phi_0 = 2.07 \times 10^{-7}$ $Gauss \cdot cm^2$ and in SI units: $\phi_0 = 2.07 \times 10^{-15}$ Wb. One thus has: $B = n_v \phi_0$, where B is the magnetic flux density, n_v is the vortex number density.

Each flux line is surrounded by a *vortex* of supercurrent. Therefore one says that a type-II superconductor is in the *vortex state* when $H_{c1} < H < H_{c2}$. The core of the vortex, is in the normal state and is surrounded by dissipationless supercurrent. The *vortex state* is also called the *mixed state* since the superconducting regions and the normal regions coexist, the latter in the core of the vortices.

The interface separating a *normal region* from a *superconducting region* cannot be a sharp surface, but must be a domain wall. The magnetic field decreases continuously from a finite value to zero, and the density of superconducting electrons increases continuously from zero to the value found in the interior of the superconducting region. The domain wall energy comes from two parts: (1) the decrease of the magnetic field energy as the magnetic field penetrates within a depth of λ in the superconducting region, $-\mu_0 \lambda H^2/2$ per unit area of surface, and (2) the increase of the condensation energy as the density of superconducting electrons decreases within a length ξ (called the *coherence length*), $\mu_0 \xi H_c^2/2$ per unit area of surface.

1. If $\xi > \sqrt{2}\lambda$, the wall energy is positive for $H < H_c$. It is not favorable to form a domain wall in this case which corresponds to type-I superconductors.

2. If $\xi < \sqrt{2}\lambda$, the wall energy is positive for $H < H_{c1}$ but negative for $H_{c1} < H < H_{c2}$, and the formation of the domain walls are favorable. These correspond to the vortex lines characterizing the mixed state in type-II superconductors.

Both ξ and λ are temperature dependent. According to the Ginzburg-Landau theory [7], $\lambda(T)$ and $\xi(T)$ vary as $(T_c - T)^{-1/2}$ when T approaches T_c, while their ratio $\kappa = \frac{\lambda(T)}{\xi(T)}$ remains finite at T_c and is practically temperature independent [7]. κ is known as the Ginzburg-Landau parameter of the material.

1.2.2 Magnetic measurements

From the point of view of an experimenter, one can generate a uniform magnetic field $\mathbf{H}_{ext}$ by a solenoid: $H_{ext} \propto nI$, where n is the number of turns per unit length, and I is the current through the solenoid. The superconducting sample understudy is immersed in this uniform field. By using, for example, SQUID magnetometer, one measures the magnetic moment $\mathbf{m}$; With micro-Hall probe sensors, one measures the local magnetic flux density $\mathbf{B}$ above the sample.

In the ideal situation where $\mathbf{B}$ is uniform in the entire sample, the information that one obtains by a global magnetic measurement faithfully reflects the magnetic properties of the material. However, this is nearly never the case. In particular, the superconductor samples to be used are thin platelets, most often measured in perpendicular fields.

For superconductors, there are no microscopic magnetic moments and the difference between the measured magnetic flux density $\mathbf{B}$ and the applied external field $\mu_0\mathbf{H}_{ext}$ is produced by the supercurrents circulating in the sample. For this reason, this difference is called the self-field $\mathbf{H}_s$, defined by:

$$\mathbf{H}_s \equiv \mathbf{B}/\mu_0 - \mathbf{H}_{ext} \tag{1.1}$$

If one denotes the current density in a superconducting sample as $\mathbf{j}(\mathbf{r})$, the self-field $\mathbf{H}_s$ can be determined by Biot-Savart's law if $\mathbf{j}(\mathbf{r})$ is known, i.e.,

$$\mathbf{H}_s(\mathbf{r}) = \frac{1}{4\pi}\int_V \frac{\mathbf{j}(\mathbf{r}') \times (\mathbf{r} - \mathbf{r}')}{(\mathbf{r} - \mathbf{r}')^3} d^3r', \tag{1.2}$$

and so is the magnetic moment $\mathbf{m}$ of the whole superconductor sample:

$$\mathbf{m} = \frac{1}{2}\int_V \mathbf{r} \times \mathbf{j}(\mathbf{r}) d^3r. \tag{1.3}$$

1.3 Vortex lattice

Vortices of the same vorticity repel each other and the vortices of opposite vorticity attract each other [8]. In a type-II superconductor, the applied external magnetic field maintains the vortices inside the superconductor. Taking into account the mutual repulsion of the vortices, without other forces, the vortices form a lattice to keep each vortex in equilibrium and to maximize the average vortex spacing in order to arrange themselves into a state of

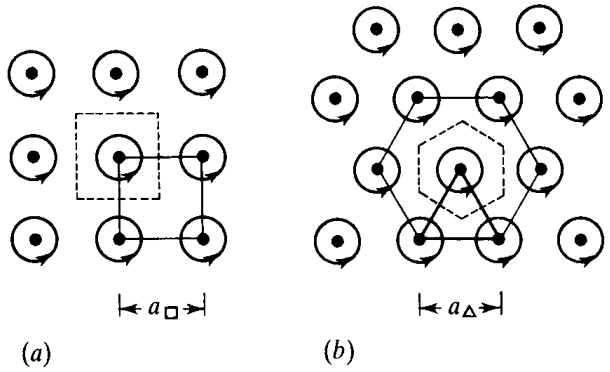

Figure 1.5: Schematic diagram of square and triangular vortex lattices. The dashed lines outline the basic unit cell. The magnetic field is directed out of the paper (Figure from [10]).

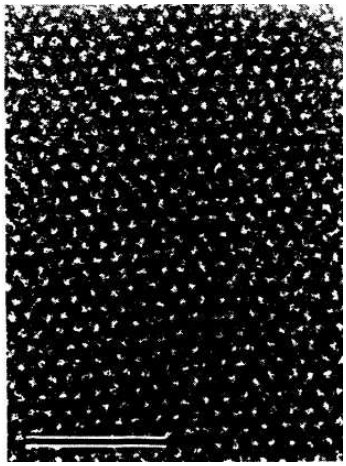

Figure 1.6: Triangular flux lattice observed by Bitter decoration method on a $Bi_{2.1}Sr_{1.9}Ca_{0.9}Cu_2O_{8+\delta}$ single crystal at T = 4.2 K, B = 20 G, the bar is 10 μm in length (Figure from [11]).

low energy [9]. The two natural possibilities to form a *close-packed* arrangement are the square and the triangular lattices, shown in Figure 1.5.

One defines a distance a_0 by the following expression: $a_0 \equiv (\frac{\phi_0}{B})^{1/2}$, where B is the average flux density. For the square lattice, the area for a basic unit cell is $S_\square = a_\square^2$, which associates a single vortex. Compared to the definition of a_0, the lattice spacing, i.e., the nearest neighbor distance between vortices, $a_\square = a_0$.

In the triangular lattice, each vortex is surrounded by a hexagonal array of other vortices. In this lattice, the area for a basic unit cell which associates a single vortex is $S_\triangle = \frac{\sqrt{3}}{2}a_\triangle^2$. The lattice spacing $a_\triangle = (\frac{2}{\sqrt{3}})^{1/2}(\frac{\phi_0}{B})^{1/2} = 1.075a_0$.

Thus for a given flux density, $a_\triangle > a_\square$. Taking into account the mutual repulsive force between vortices, the structure with the greatest separation of the nearest neighbors has the lowest energy and would be favored. This argument explains why the triangular lattice is the most favorable structure observed in the vortex state of many type-II superconductors (Figure 1.6).

Taking into account the vortex lattice structure, one can model the constitutive behav-

ior that relates the thermodynamical value for **B** and **H** [10], [12].

$$B = \frac{2\phi_0}{\sqrt{3}\lambda^2}\{ln[\frac{3\phi_0}{4\pi\mu_0\lambda^2(H-H_{c1})}]\}^{-2} \quad \text{Regime near } H_{c1} \tag{1.4}$$

$$H \approx B/\mu_0 + H_{c1}\frac{ln(\mu_0 H_{c2}/B)}{ln\kappa} \quad \text{Intermediate: } H_{c1} \leq B/\mu_0 \ll H_{c2} \tag{1.5}$$

$$B/\mu_0 = H - \frac{H_{c2}-H}{2\kappa^2-1} \quad \text{Regime near } H_{c2} \tag{1.6}$$

For high-κ materials like *BSCCO* ($\kappa > 100$), one can make the approximation $B \approx \mu_0 H$ for $H >> H_{c1}$.

1.3.1 Surface barriers: the Bean-Livingston surface barrier and the geometrical barrier

The reversible magnetization curves illustrated in Figure 1.3 can be only obtained in an ideal sample without pinning or barriers that prevent the motion of the vortices. In real superconducting samples, i.e., of finite spatial extent, the vortices necessarily interact with the Meissner current. This phenomena is at the origin of surface barriers. Two types of entrance barriers exist for field penetration in high-T_c superconductors: the so-called Bean-Livingston surface barrier and the geometrical barrier.

The Bean-Livingston surface barrier is caused by the competition between an attractive force to the surface and a repulsive force due to the Meissner current exerted on a vortex. The presence of the Bean-Livingston surface barrier leads to a vortex-free region of extent $\xi < x < \lambda$, at the sample boundary [13]. It is believed that the sample boundary should be smooth on this scale for the Bean-Livingston surface barrier to be effective and experimentally observable.

The geometrical barrier [14] is a macroscopic entrance barrier related to the cross sectional shape of the sample. It should therefore not be sensitive to small defects on the surfaces, i.e., it is much more robust to disorder than the Bean-Livingston surface barrier. The geometrical barrier results from the competition between the vortex line tension at the corners of non-ellipsoidal samples and the repulsive force due to the Meissner current.

Both kinds of barriers exist only for vortex entry but not for vortex exit[1]. Due to the surface barriers, a hysteresis on magnetization curves (or self-field) can thus occur even in the absence of bulk pinning.

[1] There is a small barrier for vortex exit in the sense that the zero magnetization branch is not at thermodynamic equilibrium. Being at a constant field, the vortex system would evolve toward the equilibrium vortex distribution.

Magnetic properties for superconductors with a platelet shape

The magnetization behavior for samples of platelet geometry is discussed here since it is this geometry that we encounter for the experiments that follow.

The geometrical barrier in a platelet shape crystal was studied and observed experimentally with micro-Hall probe sensors by E. Zeldov et al. [14]. Figure 1.7 shows the vortex concentration in the center of the sample due to the geometrical barrier for a platelet-shaped *BSCCO* crystal.

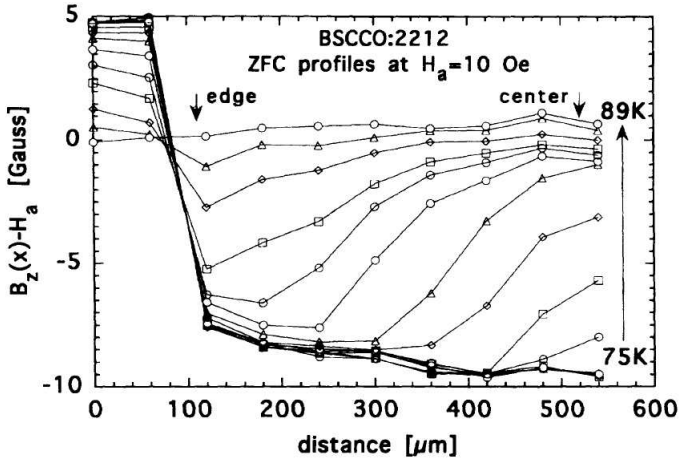

Figure 1.7: Geometrical barrier revealed by micro Hall probe sensors (Figure from [14]).

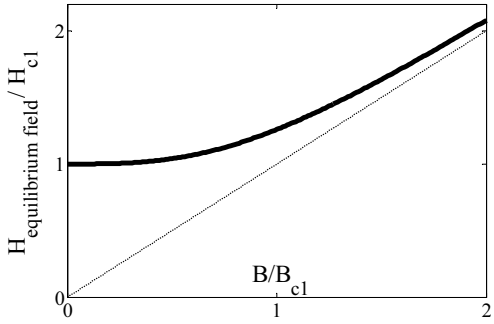

Figure 1.8: The relation between the equilibrium field $H_{equilibrium\ field}$ (also called the thermodynamic field) and the magnetic flux density according to Equation (1.7): $H(B) = (H_{c1}^{\alpha} + B^{\alpha})^{1/\alpha}$ with $\alpha = 3$.

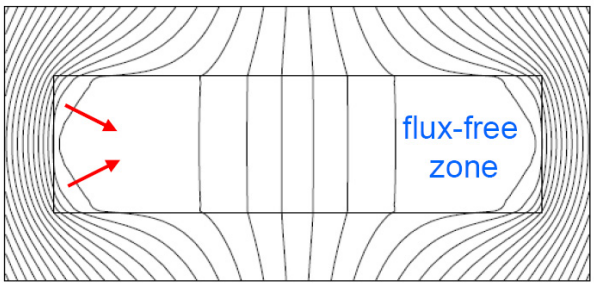

Figure 1.9: Magnetic field lines in pin-free superconducting strip, calculated by E. H. Brandt. (Figure from slides provided by E. H. Brandt).

E. H. Brandt ([15], [16]) and J. R. Clem [17] have extensively studied this subject. The numerical simulation work performed by E. H. Brandt on platelet-shaped supercon-

ductors describes the hysteresis behavior in the magnetization loop and shows the vortex concentration in the center of the sample (Figure 1.9). The approach and the notations employed by E. H. Brandt is the "Method II" approach as discussed in the Appendix A. The magnetization $\mathbf{M} \neq 0$ in this approach and one has $\mathbf{M} = \frac{1}{2V}\int_V \mathbf{r} \times \mathbf{j}(\mathbf{r}) d^3 r$. $\mathbf{M}$ is related with the thermodynamic magnetic field $\mathbf{H}$ and $\mathbf{B}$ through the relation: $\mathbf{M} = \mathbf{B}/\mu_0 - \mathbf{H}$.

The model constitutive laws $H = H(B)$ and $E = E(J)$ that E. H. Brandt employed in [15] and [16] are listed below:

$$H(B) = (H_{c1}^{\alpha} + B^{\alpha})^{1/\alpha}, \qquad \alpha = 3 \tag{1.7}$$

$$\mathbf{E}(\mathbf{j_H}, \mathbf{B}, \mathbf{r}) = \rho(j_H, B)\mathbf{j_H}(\mathbf{r}), \qquad \rho(j_H, B) = \rho_0 B \frac{(j_H/j_c)^{\sigma}}{1 + (j_H/j_c)^{\sigma}} \tag{1.8}$$

where $\mathbf{j_H}$ refers to the current that drives the vortices (Lorentz force) and can be calculated via:

$$\mathbf{j_H} = \mathbf{j} + curl\ (\mathbf{H} - \mathbf{B}/\mu_0) \tag{1.9}$$

E. H. Brandt remarked that if one approximates $\mathbf{H}(\mathbf{B})$ by its high-field value $\mathbf{H} \approx \mathbf{B}/\mu_0$, the geometric edge barrier effect cannot be obtained. One should use the forms which describe this low-field behavior: $|\mathbf{H}(\mathbf{B})| \to H_{c1}$ for $\mathbf{B} \to 0$. The boundary conditions on $\mathbf{H}(\mathbf{r})$ is set by $\mathbf{H} = \mathbf{B}/\mu_0$ at the surface and div $\mathbf{B} = 0$. For example, Equation (1.7) (plotted in Figure 1.8) has been applied in E. H. Brandt's calculations in [15] to obtain the geometrical barrier result. One can see that the low-field behavior is actually the Meissner response of a superconductor. It is consistent with the fact that the geometrical barrier is related with the Meissner current.

Because of the Meissner current, the vortices concentrate in the center of the sample. This effect can influence strongly the transport measurements since the edges become less resistive than the bulk and the current may flow only at the surfaces of a superconductor sample [18].

1.3.2 Vortex motion in type-II superconductors

The most important application right now for type-II superconductivity is in producing stable magnetic fields in large volumes. Thus, there is a need of superconducting solenoids which can provide steady fields of over 10 T without dissipation of energy because of the persistent current.

The current density which determines the net driving force on a vortex is not the total current but only the non-equilibrium part [10]. Denoting this current by $\mathbf{j}_{ext}$, the *net* force per unit length on a single vortex $\mathbf{f}_L$ is given by:

$$\mathbf{f}_L = \mathbf{j}_{ext} \times \phi_0 \hat{z}, \tag{1.10}$$

where $\hat{z}$ is the unit vector of the $\mathbf{B}$-field direction.

This force is directed perpendicularly to the current and to the **B**-field direction. Assuming that the vortex motion is impeded only by damping [10], and that, the friction force per unit length is $\gamma \mathbf{v}_L$, one has, in the steady state,

$$\mathbf{j}_{ext} \times \phi_0 \hat{z} = \gamma \mathbf{v}_L \tag{1.11}$$

The motion of flux lines induces a spatially averaged electric field **E**:

$$\mathbf{E} = \mathbf{B} \times \mathbf{v}_L, \tag{1.12}$$

parallel to $\mathbf{j}_{ext}$. A voltage drop $\int \mathbf{E} dl$ is thus established over the sample, yielding a non-zero dissipated power $\int_V \mathbf{E} \cdot \mathbf{j}_{ext} dV$. Combining Equation (1.11) and (1.12), one has:

$$\mathbf{E} = \frac{B\phi_0}{\gamma} \mathbf{j}_{ext} \tag{1.13}$$

Therefore, due to flux flow, the superconductor obeys Ohm's law, with the so-called *flux-flow resistivity* ρ_f given by:

$$\rho_f = \frac{E}{j_{ext}} = B\frac{\phi_0}{\gamma} \tag{1.14}$$

If γ is independent of B, ρ_f should be proportional to B.

To understand how the dissipation actually occurs due to a moving vortex, J. Bardeen and M. J. Stephen proposed a model based on a local approximation for a superconductor applying Ohm's law in the core of the vortex and using London equations outside the core [19]. They found a relation between the flux-flow resistivity ρ_f and the normal state resistivity ρ_n:

$$\rho_f \approx \frac{B}{\mu_0 H_{c2}} \rho_n \tag{1.15}$$

As M. Tinkham has pointed out [10], this simple form shown in Equation (1.15) does not result from a static distribution of normal cores, even if the fraction of normal part were $B/\mu_0 H_{c2}$. If the vortices are in a static configuration, the current would simply avoid the normal cores and flow only through the superconducting regions. The results given by the Bardeen-Stephen flux-flow model show that the normal current density in the core just equals the applied transport current density driving the motion of the vortices. Thus the transport current flows right through the moving cores and produces dissipation. If there are other contributions to the force balance, such as the Magnus force or forces from the linear or planar extended defects leading to guided vortex motion, the vortices move at an angle smaller than 90° with respect to the transport current. Also, in the presence of a pinning force due to crystalline defects in the material, the current density through the core is less than the applied transport current density[2]. One then has less dissipation in the core and thus a lower resistance.

[2] M. Tinkham proposed the following image: the transport current is uniform in the whole sample, while there exists a backflow of current at pinning vortices. The superposition of the uniform transport current and the backflow current yields that the current density through the core is less than the applied transport current density [10].

1.3.3 Vortex pinning in type-II superconductors and irreversible magnetization

If the vortices are completely pinned, there is no measurable resistance. Denoting the pinning force by f_p, if $f_L < f_p$, the vortices are prevented from motion and there is no resistance. As the current density is increased, f_L becomes larger. At the critical current density j_c, $f_L > f_p$ and the pinned vortices begin to move and cause power dissipation. This critical current density j_c is called the *depinning* critical current density[3].

The pinning force opposing vortex motion is the origin of the irreversible magnetization (or self-field) of type-II superconductors. The hysteresis in the *M-H* loop is due to pinning and the width of the hysteresis is proportional to the pinning force and therefore the depinning critical current density.

Critical state model (Bean's model)

One considers an infinite slab which has a width $2w$ along the x-axis and extends in the y-direction. The magnetic field H_a is applied along the z-axis (Figure 1.10 (a)). In Bean's model, the current density can only take three values: $\pm j_c$ and 0 [20]. For "field-free" regions or for "field-invariant" regions, $\mathbf{j} = 0$ and for "critical" regions, $|\mathbf{j}| = j_c$. The critical state behavior as the applied field H_a is increased for a sample initially in the virgin state is given by Equation (1.16) for current distribution and by Equation (1.17) for field distribution.

$$j_y(x) = \begin{cases} j_c & -w < x \leq -a, \\ 0 & -a < x < a, \\ -j_c & a \leq x < w. \end{cases} \tag{1.16}$$

$$B_z(x) = \begin{cases} 0 & 0 \leq |x| < a, \\ \mu_0(|x| - a) j_c & a \leq |x| < w. \end{cases} \tag{1.17}$$

with a determined by: $a = w - \frac{H_a}{j_c}$.

The situation is more complicated in other geometries, but the gradient of the magnetic flux density remains proportional to the critical current density j_c. Here we report the calculated results for a thin film of thickness d under the same field configuration as that

[3] There is another critical current density which has the name *depairing* critical current density since above this current density, the *Cooper* pairs would be broken. In general, the *depairing* critical current density is a factor of 100 higher than the *depinning* critical current density. For practical reasons, the critical current density for type-II superconductors always refers to the *depinning* critical current density.

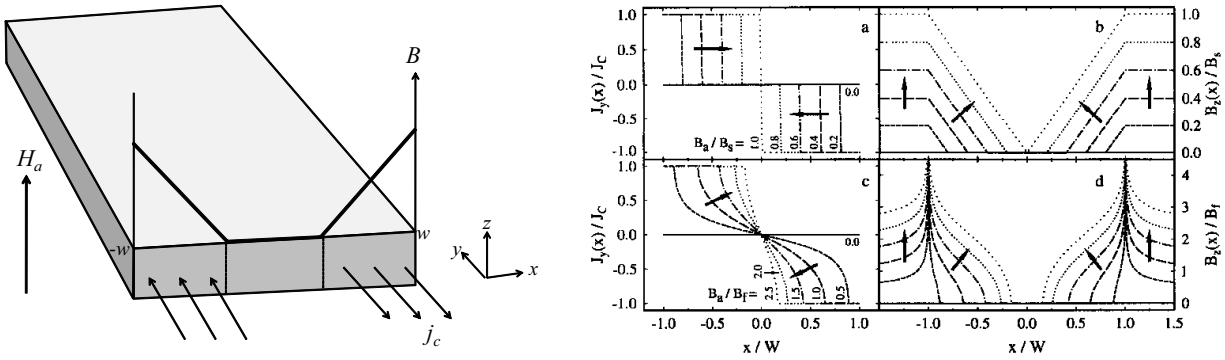

(a) (b)

Figure 1.10: (a) An infinite type-II superconducting slab immersed in a magnetic field H_a. H_a is along the z-axis. In the Bean's model, the slope of $B_z(x)$ is proportional to the critical current density j_c. (b) Current and field profiles for a slab (top) and a thin film (bottom) which are initially in the virgin state. Arrows indicate the progression of field penetration (Figure from [21]).

of the slab illustrated in Figure 1.10 (a) [21]:

$$j_y(x) = \begin{cases} j_c & -w < x \leq -a, \\ -\frac{2j_c}{\pi} \arctan\left(\frac{x}{w}\sqrt{\frac{w^2-a^2}{a^2-x^2}}\right) & -a < x < a, \\ -j_c & a \leq x < w. \end{cases} \tag{1.18}$$

$$B_z(x) = \begin{cases} 0 & |x| \leq a, \\ B_f \ln \frac{|x|\sqrt{w^2-a^2}+w\sqrt{x^2-a^2}}{a\sqrt{|x^2-w^2|}} & |x| > a. \end{cases} \tag{1.19}$$

where $B_f = \frac{1}{\pi}\mu_0 d j_c$ and a is determined by: $a = \frac{w}{\cosh(\mu_0 H_a / B_f)}$. The above results are plotted in Figure 1.10 (b).

1.4 High-T_c superconductors

In 1986, J. G. Bednorz and K. A. Müller discovered "high-T_c superconductivity" in $La_{2-x}Ba_xCuO_4$ at 30 K [4]. Soon thereafter, M. K. Wu et al. discovered superconductivity at 93 K in $YBa_2Cu_3O_{7-\delta}$ [5]. The attractive paring interaction in high-T_c superconducting cuprates is thought to be magnetic in origin. Its paring symmetry is *d-wave* in *YBCO* and *BSCCO*. The phase diagram for the vortex system in high-T_c is more complicated than conventional superconductors. Besides the vortex lattice phase, there exists a vortex liquid phase at higher temperature and field part. Now we discuss the general properties of $Bi_2Sr_2CaCu_2O_{8+\delta}$.

The crystal structure of $Bi_2Sr_2CaCu_2O_{8+\delta}$ is shown in Figure 1.11 (a). The thickness of the CuO_2 bilayer is s = 3 Å and the thickness of the $Bi_2Sr_2O_4$ isolating layer between two conducting layers is d = 12 Å. The material cleaves easily between two BiO planes and we have used this property for obtaining good quality of $BSCCO$ single crystals for study.

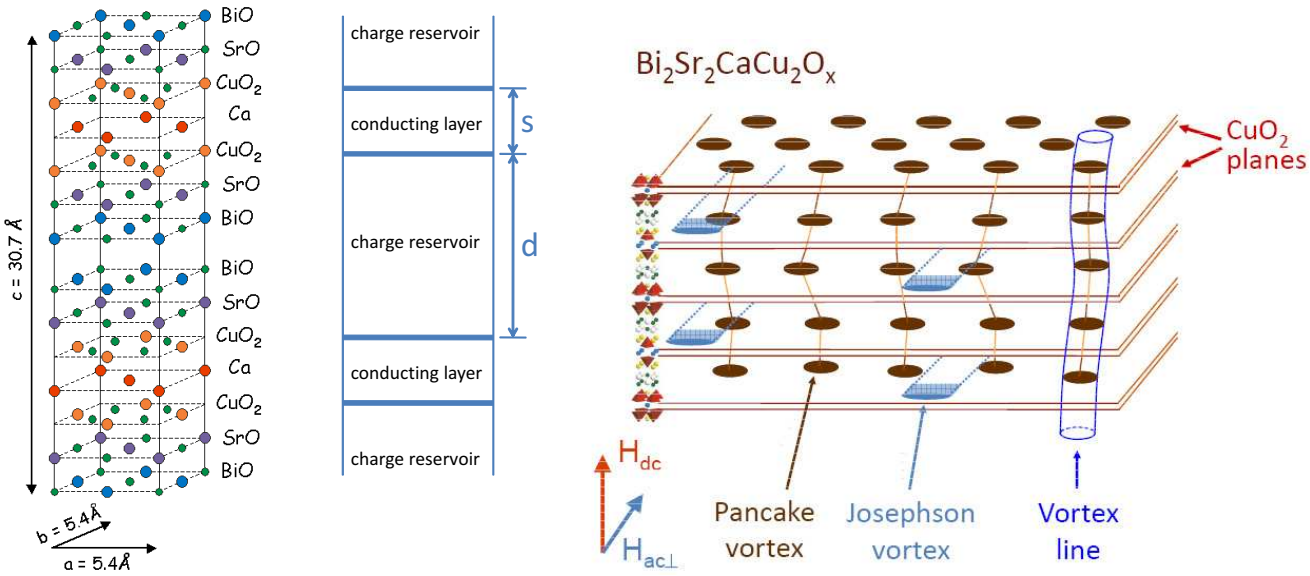

(a) (b)

Figure 1.11: (a) Crystal structure for $Bi_2Sr_2CaCu_2O_{8+\delta}$ (Figure provided by E. W. Hudson). (b) Koshelev crossing lattices: Josephson vortices and pancake vortices (Figure provided by A. Koshelev).

It is believed that only the CuO_2 double layers are superconducting. Consequently, the superconducting order parameter is higher there, while it is small or zero in the rocksalt-like BiO blocking layers. The coherence length parallel to the ab plane is denoted as ξ_{ab} and the coherence length along the c-axis is denoted as ξ_c. The ratio ξ_{ab}/ξ_c is called the anisotropy constant. For optimally doped $Bi_2Sr_2CaCu_2O_{8+\delta}$ crystals, this anisotropy constant is between 350 and 500 [22], [23]. The Abrikosov vortex lines in $BSCCO$ can be regarded as a stack of Josephson coupled pancakes vortices in each of the CuO_2 planes (Figure 1.11 (b)).

Since the *ab plane* is isotropic for $Bi_2Sr_2CaCu_2O_{8+\delta}$ crystals, which is the subject of this thesis, from now on, the term *"in-plane"* means parallel to the *ab plane*; the term *"out of plane"* means perpendicular to the *ab plane*. Experiments show that in the normal state, the *out of plane* electrical resistivity ρ_c is much higher than the *in-plane* resistivity ρ_{ab}. Approximately, one has: $\xi_{ab}/\xi_c \approx \sqrt{\rho_c/\rho_{ab}}$.

1.5 Melting of the vortex lattice

Similar to real crystals, the Abrikosov vortex lattice melts to a vortex liquid when the temperature is increased under a fixed external magnetic field H_{ext}. This first-order melting transition of the vortex lattice melting has been discovered through the observation of a discontinuity in the local magnetic induction (vortex density) in $Bi_2Sr_2CaCu_2O_8$ single crystals [24] and later confirmed to exist in $YBa_2Cu_3O_{7-\delta}$ single crystals through the measurement of the latent heat [25].

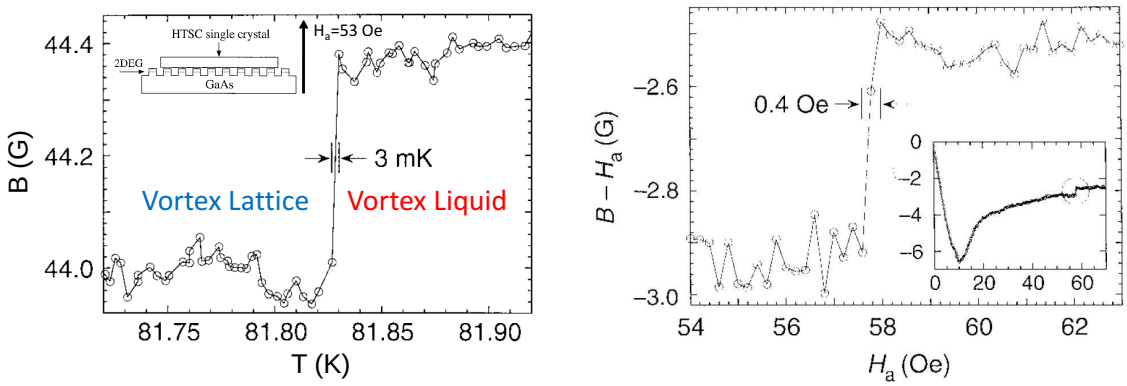

(a) (b)

Figure 1.12: Vortex lattice melting observed through the local magnetic induction measurements. (a) Temperature scan: local magnetic flux density step at the first-order vortex-lattice melting (freezing) transition in $Bi_2Sr_2CaCu_2O_8$ measured with Hall sensor technique by decreasing the temperature at constant field of 53 Oe. The sample was cooled very slowly ($5 \sim 15$ mK/min) (b) Field scan: local magnetic flux density step as the melting line is crossed by increasing the applied field at 80 K. Inset: the entire local magnetization curve (also called the self-field curve), $B - H_a$, as a function of increasing applied field H_a (Figures from [24]).

E. Zeldov et al. observe [24] that in swept field measurements (Figure 1.12 (b)), the step occurs at the same value of the local induction B_z at various locations across the sample, but at different values of H_{ext} due to the non-uniformity of the B_z profile across the sample.

As a result, in standard global magnetization measurement, the observed step is actually an value averaged over the entire sample; the variation of the magnetic moment with external field is in general broader and smoother, masking the underlying physical phenomena [24].

The microscopic Hall probe sensors used in [24] have an active area of 3×3 μm^2 and the active layer of these sensors were located only ~ 0.1 μm below the surface. Therefore a very accurate measurement of the local magnetic field with the spatial resolution corresponding to the size of the active area, 3 μm, was obtained.

Experiments show that the vortex density in its liquid state is higher than that in its

lattice state (Figure 1.12). By temperature scans as shown in Figure 1.12 (a), one can define the melting temperature T_m above which the magnetic induction (increasing) step occurs; Similarly, by field scans as shown in Figure 1.12 (b), one can define the melting field B_m above which the magnetic induction (increasing) step occurs. Plotting the corresponding values of (T_m, B_m) on a *T-B* diagram, one obtains a line that separates the vortex liquid state and vortex lattice state (Figure 1.13). This line is called the first-order melting (freezing) transition line.

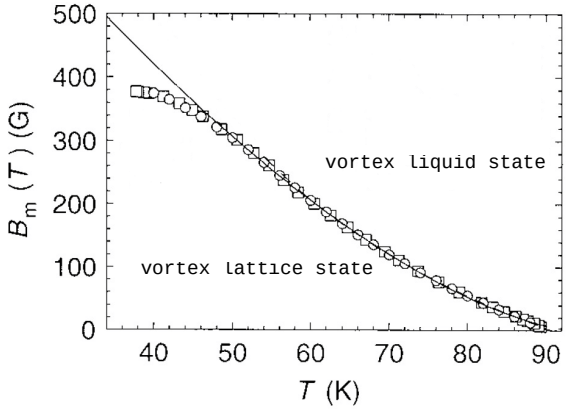

Figure 1.13: Vortex liquid to lattice transition line in $Bi_2Sr_2CaCu_2O_8$ as measured by field scans (◯) and temperature scans (□). The solid line is a fit to $B_m(T) = B_0(1 - T/T_c)^{\alpha}$, where α = 1.55, B_0 = 990 G, and T_c = 94.2 K (Figure from [24]).

1.6 Phase diagram for vortex system in *BSCCO* with disorder and vortex shaking experiments

The phase diagram for $Bi_2Sr_2CaCu_2O_8$ is shown in Figure 1.14. On this phase diagram, the blue line, which also corresponds to a first order transition and seems to the continuation of the melting transition at lower temperature, separates two phases: a rather weakly pinned vortex lattice at low fields, and a more strongly pinned vortex liquid or glass at high fields [26], [27].

At high temperatures, vortex system is influenced by thermal fluctuations and pinning by defects in the superconductor is relatively weak. When temperature is decreased, the defects begin to pin the vortices and therefore it is more and more difficult to reach thermodynamic equilibrium in the sense of achieving a ground state with lowest energy. Experiments with micro-Hall probe sensors performed by E. Zeldov et al. [24] on *BSCCO* showed that the local magnetic induction step at melting was no longer observed when the temperature was decreased below a certain value (38 K for their sample shown in

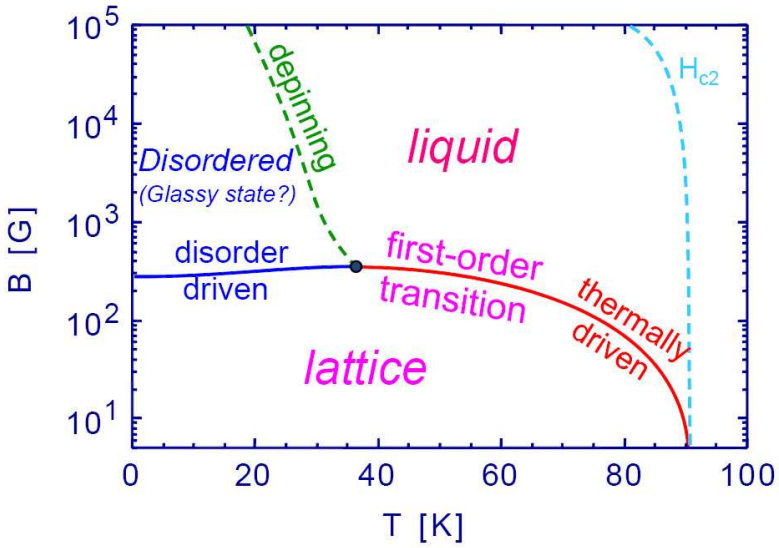

Figure 1.14: BSCCO phase diagram (Based on the phase diagram provided by E. Zeldov).

Figure 1.15), called the critical point. If the same measurement is repeated in presence of an in-plane ac field, one finds a fully reversible magnetization and the self-field step characteristic for a first order transition can be once again observed [28] (Figure 1.16).

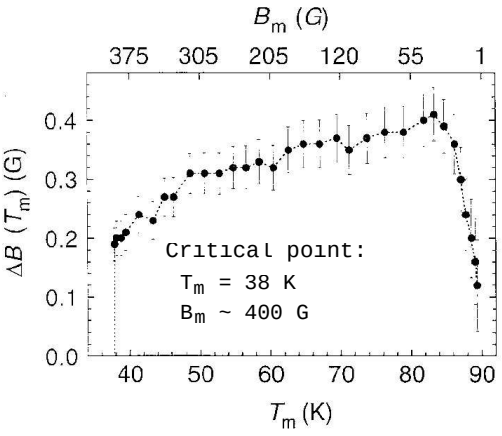

Figure 1.15: Magnetization step, characteristic for a first order transition, was not any more observed below 38 K in *BSCCO* single crystals measured by E. Zeldov et al. (Figure from [24]).

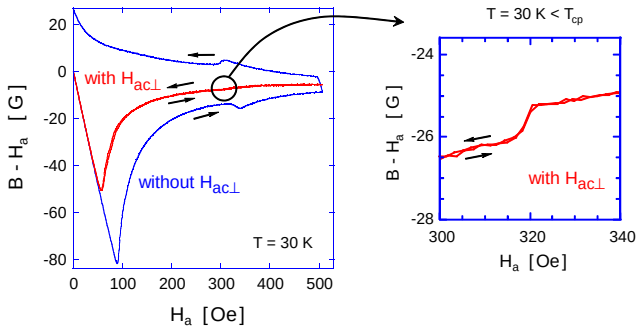

Figure 1.16: Magnetization loop with "vortex shaking". With the application of an in-plane ac field, the hysteresis is suppressed and the reversible magnetization step is observed (Figure based on slides provided by E. Zeldov).

Questions remain about the nature of the *"shaken"* equilibrium compared to a real thermodynamic equilibrium. As P. Gammel has pointed out, the unique properties of

shaken equilibrium can lead to phase diagrams determined by the shaking itself, rather than by a thermodynamic variable such as temperature [29].

The existence of the *"vortex glassy state"* is not yet confirmed, i.e., whether the dashed depinning line is a *vortex liquid* to *"vortex glass"* phase transition or just a continuous variation of the vortex mobility. If one can probe the dynamics of the vortex motion near to the depinning line, one can thus obtain information on the nature of the vortex state in this region.

1.7 Scope of this thesis

Three different length scales can be defined in high-T_c superconductors:

1. Microscopic level: properties of single flux lines and interaction of individual flux lines with defects.

2. Mesoscopic level: length scales ≥ 1 μm, i.e., defined on length scales larger than the correlation length of collective behavior of vortices.

3. Macroscopic level: the entire superconductor.

It is extremely important to obtain experimental information on mesoscopic level in high-T_c superconductors since it is on this length scale that the distribution of critical currents is defined [30]. Moreover, the macroscopic inhomogeneities can be revealed by observation on this level, which permits one to verify whether the intrinsic properties of material under study have been obtained [31].

In this thesis, two experimental techniques have been employed and combined. Chapter 2 is devoted to the magneto-optical imaging technique, which corresponds to mesoscopic-level observation on superconducting samples. Differential magneto-optical imaging with different kinds of modulation are discussed in this Chapter. Magneto-optical imaging has been used for sample selection, verification after irradiation experiments, characterization, and transport current visualization in this work.

Chapter 3 deals with the experimental aspects of transport measurements. A good quality of electrical contacts on single *BSCCO* crystals is essential for performing transport measurements. We used photolithography to achieve electrical contacts on the surface of the crystals. This permits us to visualize the transport current flow in our *BSCCO* samples.

Chapter 4 studies the field and current distribution for a superconductor in a NMR field configuration. Conclusions drawn from this chapter are useful to correctly interpret the NMR data on type-II superconductors.

Chapter 5 is the main part of this thesis. In order to investigate the mechanisms that govern the vanishing of linear resistance, we have measured the vortex shear viscosity

in a 20 μm-wide channel confined structure [32]. The vortex confinement effects among different kinds of confinements are compared. The heavily irradiated contact pads remote from the edges allow one to probe vortex bulk properties. The shear flow resistivity data are compared with two models describing vortex liquid-solid transitions: the two dimensional melting mediated by separation of dislocation pairs and the three dimensional Bose-glass transition.

Chapter 2

Magneto-optical imaging

In global magnetic measurements, one obtains an averaged value for the magnetic flux density over the entire sample. However, the physical phenomena under study are often masked or otherwise inaccessible because the averaging masks out small local changes of the flux density. A good example is the magnetization of a ferromagnet which contains the averaged information of flux density variations associated with the presence of magnetic domains. It is thus important to perform local magnetic field measurements. Magneto-optical imaging is a powerful tool since it permits one to obtain an image of the local magnetic flux density at the surface of the entire sample. The physical principe underlying magneto-optical imaging is the Faraday effect.

2.1 Faraday effect

The Faraday effect is a consequence of the fact that the magnetic field removes the symmetry for the propagation of left-handed and right-handed circularly polarized light.

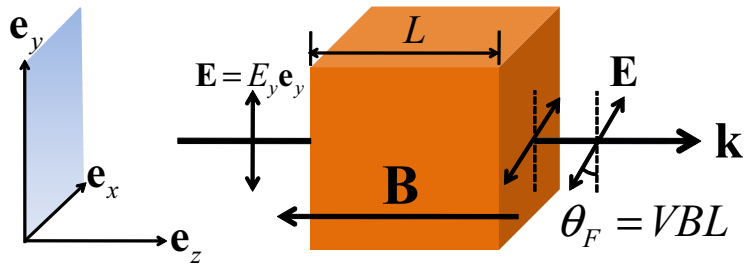

Figure 2.1: Linearly polarized incident light traverses the media (from the left to the right) in the presence of an axial magnetic field **B** (along the z-axis). **k** denotes the wave vector of the light. The electric field vector **E** rotates an angle $\theta_F = \mathcal{V}BL$. This effect was discovered by M. Faraday (1791 - 1867) in 1845.

Linearly polarized light can be seen as a combination of a right circularly polarized

wave and a left circularly polarized wave with the same phase. When linearly polarized light propagates through certain media with different indices of refraction for waves of the two polarizations (right circular and left circular) in the presence of a magnetic field, at exit the right and left circularly polarized waves will have acquired different phases. The transmitted light at the exit is still linearly polarized but its electric field vector **E** has been rotated over an angle θ_F which is proportional to the magnitude of the axial magnetic field B and the length L that the light has traversed in the media: $\theta_F = \mathcal{V}BL$, where $\mathcal{V}$ is called the Verdet constant, which is material and wavelength dependent.

There is a simple relation between the Verdet constant and the wavelength dependence of the index of refraction which was first derived by J. Larmor using a semi-classical calculation in 1898 [33]:

$$\mathcal{V} = -\frac{e}{2mc}\lambda\frac{dn}{d\lambda}, \tag{2.1}$$

where e is the charge of an electron, m is the mass of an electron, c is the speed of light, λ is the wavelength of light and n is the index of refraction of the medium. This relation works very well for gases, while for solids, one needs to add a dimensionless constant $\mathcal{C}$ to include the deviation of the Verdet constant from the value predicted by Equation (2.1):

$$\mathcal{V} = -\mathcal{C}\frac{e}{2mc}\lambda\frac{dn}{d\lambda} \tag{2.2}$$

In *cgs units*, the Verdet constant has units of $radians \cdot Gauss^{-1} \cdot cm^{-1}$.

The Verdet constant for most materials is extremely small. For example, $\mathcal{V} = 3.80 \times 10^{-6}$ $radians \cdot Gauss^{-1} \cdot cm^{-1}$ for water at 20 °C and for light at 589 nm.

The Faraday effect can be used for magnetic measurements. As most of the superconductors have very small Verdet constant, one places an *"indicator film"* which presents a high Verdet constant on the top surface of the superconductor in question. This indicator film detects the magnetic field at the surface of the superconductor. The Faraday active layer in the magneto-optical indicators that we use in our laboratory is a ferrimagnetic bismuth doped yttrium-iron garnet (*Bi:YIG*) layer.

Now we discuss the properties of magneto-optical indicators and the characteristics that we look for in a magneto-optical indicator.

2.2 Magneto-optical indicators

The *YIG* layers used in this work are a few microns thick. They are grown by liquid-phase epitaxy on a transparent gadolinium-gallium-garnet (*GGG*) substrate so that it can stand alone. To use it in a reflection mode, a very fine layer of *Al*, serving as a mirror, is evaporated on top of the *YIG* surface. The mirror is covered by a thin protective *Ti-TiN* layer and an anti-reflective layer is added to the substrate layer (Figure 2.2 (a)).

The indicators that we use have a thickness of 4 μm for the *YIG* layer and a thickness of 0.5 *mm* for the substrate. Figure 2.2 (b) shows that a wafer of magneto-optical film was cut into different sizes adapted to samples of different dimensions.

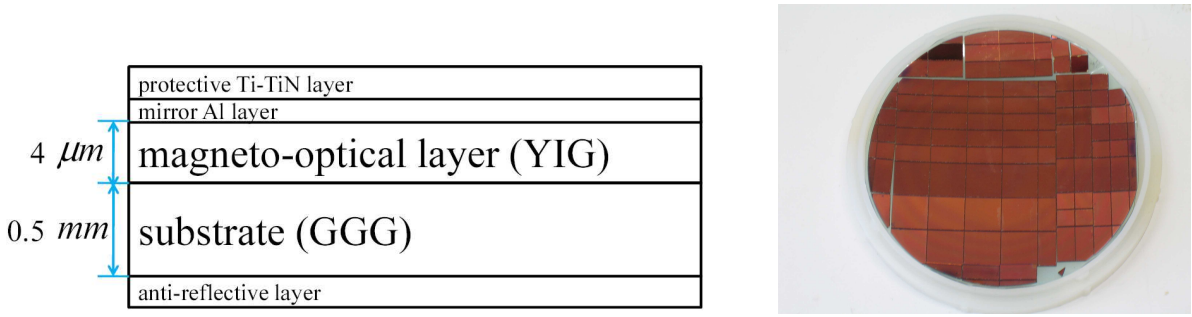

(a) (b)

Figure 2.2: (a) Schematic representation for different layers in a magneto-optical indicator. (b) A wafer of magneto-optical indicators.

2.2.1 Magnetic properties of the layer Bi: YIG

The MO indicator material is ferrimagnetic with a spontaneous magnetization, $\mathbf{M}_s$, and the easy axis lying in the film plane. A magnetic field $\mathbf{B}$ applied at an angle α (see Figure 2.3 (b)) will force the magnetization vector to turn out of the plane. We decompose $\mathbf{B}$ into the in-plane field component B_x and the out-of-plane field component B_z: $B_x = B cos\varphi_B$, $B_z = B sin\varphi_B$. The Faraday rotation angle is given by: $\theta_F = \mathcal{V} L M_s sin\phi$. There exists a saturation rotation angle: $\theta_{sat} = \mathcal{V} L M_s$. The presence of a parallel magnetic field yields a reduced Faraday rotation angle θ_F. This behavior can be explained as follows.

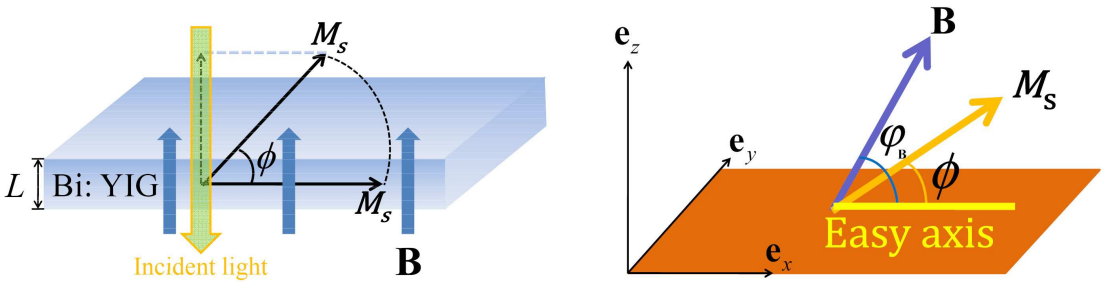

(a) (b)

Figure 2.3: (a) The perpendicular magnetic field $\mathbf{B}$ induces the rotation of the magnetization vector $\mathbf{M}_s$. The perpendicular component of $\mathbf{M}_s$ produces the Faraday rotation. (b) The equilibrium tilt angle ϕ of the magnetization $\mathbf{M}_s$ is determined by the balance between the magneto-crystalline anisotropy of the Bi-YIG layer and its tendency to align with the external field $\mathbf{B}$.

Adopting the simplest form to find the equilibrium tilt angle ϕ, one minimizes the total magnetic energy composed of the anisotropy energy $E_A(1-\cos\phi)$ and the dipolar energy:

$$E(B,\phi) = E_A(1-\cos\phi) + BM_s[1-\cos(\varphi_B-\phi)].$$

The condition $\frac{\partial E}{\partial \phi} = 0$ yields:

$$\tan\phi = \frac{B_z}{B_A + B_x},$$

where the anisotropy field $B_A \equiv E_A/M_s$. As the Faraday rotation angle is proportional to the component of $\mathbf{M}_s$ parallel to the propagation direction of the light (z-axis) it follows that:

$$\theta_F \propto \sin\phi = \frac{B_z}{\sqrt{(B_A+B_x)^2+B_z^2}}.$$

This model describes both the reduced Faraday rotation angle θ_F by a parallel field and also the saturation for large B_z ($sin\phi \to 1$ for $B_z \gg B_A$). Under normal operation conditions for magneto-optical imaging, B_x is small and the Faraday rotation angle is given by:

$$\theta_F = \mathcal{V}LM_s sin\phi = \mathcal{V}LM_s \frac{B_z}{\sqrt{B_A^2+B_z^2}}.$$

The relation between θ_F and B_z is approximately linear for a not too large value of B_z (compared to B_A defined by $B_A \equiv E_A/M_s \sim$ 600 - 1000 G, depending on the indicator film):

$$\theta_F = B_z L \mathcal{V} \frac{M_s}{B_A} \equiv B_z L \mathcal{V}_{MO}, \tag{2.3}$$

where the Verdet constant for a MO indicator $\mathcal{V}_{MO}$ is defined by:

$$\mathcal{V}_{MO} = \mathcal{V}\frac{M_s}{B_A} = \mathcal{V}\frac{M_s^2}{E_A} \tag{2.4}$$

2.2.2 Doubled Faraday rotation to enhance the sensitivity

If, after passing through the magneto-optical layer, the light is reflected by a mirror and travels through the media again (the axial magnetic field is always present), the Faraday rotation will be doubled (Figure 2.4).

Denoting I_{in} as the incident light intensity, I_r as the reflected light intensity of the magneto-optical indicator, of thickness L and absorption coefficient β (if one takes into account the optical absorption by the magneto-optical layer), one has: $I_r = I_{in}e^{-2\beta L}$. The doubled Faraday rotation angle $\theta = 2\theta_F$, where $\theta_F = \mathcal{V}_{MO}BL$. One defines a characteristic constant k for an "*indicator film*" in reflection mode by: $k \equiv \theta/B = 2\mathcal{V}_{MO}L$, k has the unit °/G. To reveal the Faraday rotation effect, one places an analyzer which is in crossed

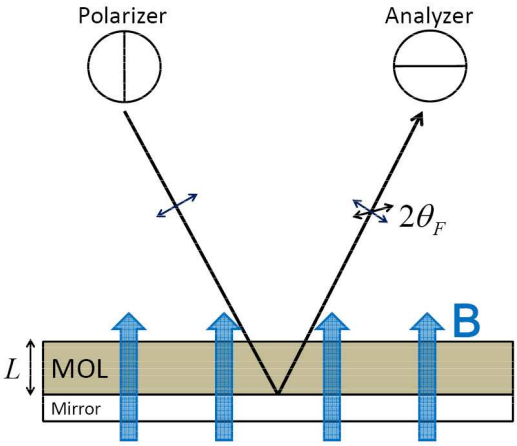

Figure 2.4: Faraday rotation doubled by a mirror. The Faraday rotation effect takes place at the Magneto-Optic Layer (MOL).

position to the polarization of the incident light. According to Malus's law, the light intensity I_{out} behind the analyzer is then:

$$I_{out} = I_r sin^2(2\mathcal{V}BL) = I_{in}e^{-2\beta L}sin^2(2\mathcal{V}_{MO}BL). \tag{2.5}$$

As one wishes to have a large signal I_{out}, Equation (2.5) shows that a magneto-optical indicator should have a high Verdet constant and a low absorption coefficient.

If one takes into account the imperfection of the polarizer and the analyzer, the intensity measured once the light has passed the analyzer is: $I = K_0 + E_0^2 sin^2\theta$, where $\theta = kB$ is the Faraday rotation angle due to the presence of the magnetic field $\mathbf{B}$, K_0 corresponds to the background intensity, which describes the stray light and noise contribution to the signal, and $E_0^2 \equiv I_{in}e^{-2\beta L}$. For a given indicator, β and L are constants, for convenience, one uses E_0^2, which has already taken into account the optical absorption by the magneto-optical layer, to denote the incident light intensity. The polarizer and analyzer are usually not perfectly crossed, their relative angle is denoted as $90^\circ - \alpha$. The light intensity measured after the analyzer is then:

$$I = K_0 + E_0^2 sin^2(\theta + \alpha). \tag{2.6}$$

2.3 Magneto-optical imaging

The magneto-optical (MO) indicator is placed with the mirror side in contact with a flat sample (magnetic or superconductor, etc.). The linearly polarized light is incident on the indicator film from above, and is reflected from the aluminium layer placed in contact with the sample surface. While traveling in the indicator film, the light experiences a Faraday

rotation proportional to the perpendicular component of the local magnetic field. The local magnetic field information is obtained by observation through an analyzing polarizer, allowing one to detect the angle of Faraday rotation at each point on the sample surface. The image formed by the light, after it has passed through the analyzer is observed by an optical microscope (Figure 2.5 (a)). The intensity of the light is determined by the local perpendicular field B_z at the sample surface: bright regions in the magneto-optical image corresponds to high B_z, while dark regions in the magneto-optical image corresponds to low B_z (Figure 2.5 (b)).

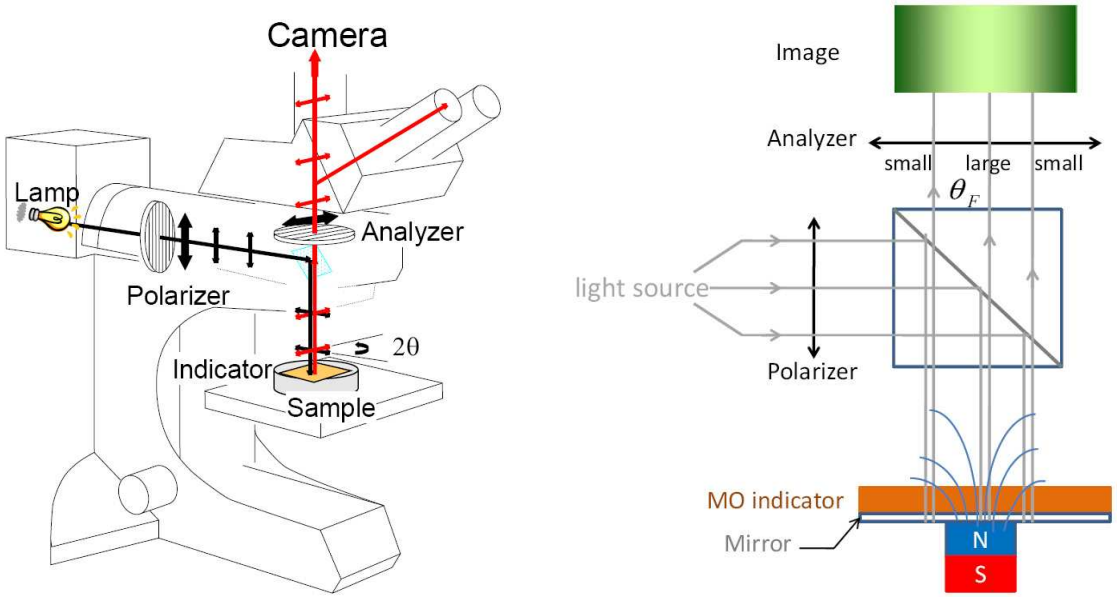

(a) (b)

Figure 2.5: (a) Magneto-optic set-up for local magnetic flux density imaging at LSI (figure kindly provided by Minoru Uehara, based on a photo of the real set-up at LSI). (b) Magneto-optical image formation: the contrast of the light intensity at the exit of the analyzer reflects the variation of the magnetic flux intensity of the surface covered by the MO indicator.

θ and α are usually less than 4°, i.e., 0.07 in radian units, very small compared to $\pi/2$. Applying $sin(x) \approx x$ for $x \ll 1$, one has[1]:

$$I = K_0 + E_0^2 sin^2(\theta+\alpha) \cong K_0 + E_0^2(\theta+\alpha)^2 \tag{2.7}$$

[1] In our study, we always work in this situation with magneto-optical imaging. The maximal value of the magnetic field generated by the coils that we use is about 400 Oe, this corresponds to a maximum rotation angle of 4° (0.07 in radian units). The maximal difference between $sin(x)$ and x in our study is thus $|sin(0.07) - 0.07| = 5.71 \times 10^{-5}$, which is negligible.

2.3.1 Magneto-optical indicators characterization: determination of the absolute rotation angle

Equation (2.7) has three unknowns, K_0, E_0^2 and θ. In order to recover the absolute value of θ, one should perform three independent measurements of the intensity. For example, one chooses to measure at $\alpha = -\alpha_0$, 0, and $+\alpha_0$ ($\alpha_0 \approx 2^\circ$), the corresponding light intensities are denoted by I_- , I_0, and I_+.

Using Equation (2.7), the Faraday rotation angle can be obtained by the following equation [34]:

$$\theta = \frac{\alpha_0}{2} \frac{I_+ - I_-}{I_+ - 2I_0 + I_-} \tag{2.8}$$

To perform this measurement, a Faraday active film (*YIG* garnet with perpendicular anisotropy) inserted in a copper coil is added in the optical path. The incident light experiences a Faraday rotation due to the nonzero magnetization of this *YIG* film when a current is applied to the coil. By changing the current, we modulate the angle α. We have used this method to characterize the magnetic response of our MO indicators.

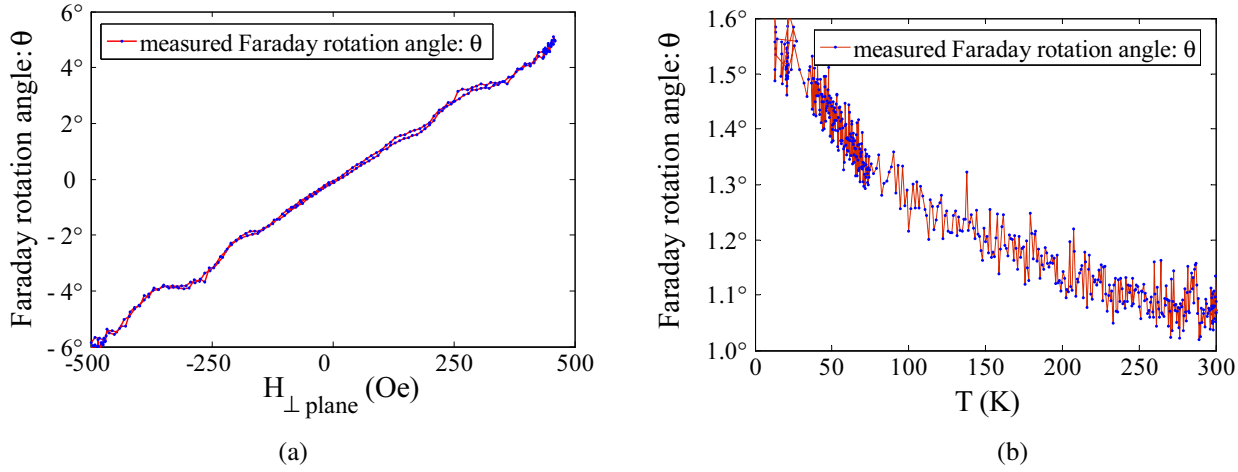

Figure 2.6: Magneto-optical indicator film characterization on the indicator denoted as *"VS-55-K"*. (a) Measured Faraday rotation angle as a function of the external field, perpendicular to the plane of the garnet film, at T = 315 K and with white light. The relation is approximately linear and the proportionality constant is about 0.01°/Oe. (b) Measured Faraday rotation angle as a function of the temperature at $H_{\perp plane}$ = 90 Oe with green light (wavelength $\lambda \approx 530$ nm) by using a filter equipped in the interior of the microscope.

The measurements demonstrate (Figure 2.6 (a)) that our magneto-optical indicators present a significant Faraday rotation (1° per 100 Oe). The response of the indicators is approximately linear with very weak magnetic hysteresis. The value of the saturation field is about 900 Oe.

The indicator was cooled to T = 20 K with the presence of a constant perpendicular field of 90 Oe and then the liquid helium flow was stopped. A temperature was read every

5 seconds and its corresponding rotation angle was measured during warm-up.

Figure 2.6 (b) shows that at low temperatures, our indicator presents a larger Faraday effect. This is consistent with the ferrimagnetic nature of the *YIG* layer: as the spontaneous magnetization $\mathbf{M}_s$ decreases when temperature is raised, one has a lower Verdet constant $\mathcal{V}_{MO}$ due to the Equation (2.4).

2.3.2 Optimization of image contrast

The field sensitivity of magneto-optical (MO) imaging is typically several Gauss. The non-uniform illumination, inhomogeneity of the MO indicator and dust presented on the optical path (dust on the indicator, infra-red filter, polarizers and other optical parts of the microscope) are the factors limiting the effective field resolution of the MO imaging technique.

Taking into account the imperfection of the analyzer, to optimize the image contrast, the analyzer and polarizer are set a little deviated from the crossed position. This angle was denoted as α in Equation (2.7).

E_0^2 denotes the incident light intensity; $T_{//}$ and $T_\perp$ denote the transmittance of the light polarized parallel and perpendicular to the transmission direction of the analyzer.

The light intensity received by the camera without (I_1) and with (I_2) application of the magnetic field are:

$$I_1 = E_0^2 sin^2\alpha \cdot T_{//} + E_0^2 cos^2\alpha \cdot T_\perp \tag{2.9}$$

$$I_2 = E_0^2 sin^2(\alpha+\theta) \cdot T_{//} + E_0^2 cos^2(\alpha+\theta) \cdot T_\perp \tag{2.10}$$

Developing Equation (2.10) as the first order in θ, one gets:

$$I_2 = E_0^2 sin^2\alpha \cdot T_{//} + \theta \cdot E_0^2 T_{//} sin2\alpha + E_0^2 cos^2\alpha \cdot T_\perp - \theta \cdot E_0^2 T_\perp sin2\alpha$$

We define a contrast parameter $C = \frac{I_2 - I_1}{I_1}$ and maximize it. Assuming $\frac{T_\perp}{T_{//}} \ll 1$ and $\alpha, \theta \ll 1$ yields

$$C_{opt} \approx 2\theta \sqrt{\frac{T_{//}}{T_\perp}}$$

for $\alpha_{opt} = \sqrt{\frac{T_\perp}{T_{//}}}$.

The value for polarizer extinction varies typically from 20 dB to 40 dB. We can thus estimate that the optimal deviation angle lies between $0.57\,^\circ \sim 5.7^\circ$.

The above calculation was presented in [35]. In practice, we determine the derivation angle α by the maximum contrast perceived by eye. The main reason is that we need to adjust the definition of the contrast parameter as a function of our experimental goal: revealing inhomogeneity and macroscopic defects (contrast between different regions within one sample), or the diamagnetic behavior revealed by the superconducting

sample as a whole (contrast between the sample and the background) in order to determine, e.g., the critical temperature T_c or the critical current density j_c.

2.4 Experimental setup for magneto-optics

The sample covered by the magneto-optical indicator is mounted in a special cryostat (Oxford Instruments MicrostatHe®) providing temperatures as low as 6 K with optical access from above. The sample can be viewed through a window (it is also an infra-red filter in order to avoid the thermal radiation) in the cryostat and details of the magnetic flux distribution could be studied using a microscope with polarized light. Focusing and XY-translation are enabled by mounting the cryostat on an adjustable XYZ-stage.

The MO indicator and the sample are placed on a OFHC (Oxygen-Free High Conductivity) copper sample holder, which is directly fixed to the cold finger of the flow cryostat. An indium foil is crushed between the sample holder and the cold finger in order to improve thermal contact. The whole mount is inserted into the cylindrical vacuum space.

A split coil copper magnet is mounted on the aluminium lids of the vacuum chamber. These coils are used for the application of a magnetic field component (up to 550 Oe) perpendicular to the sample plane. In addition, one can also apply a magnetic field parallel to the sample plane by using another copper wire magnet. An iron core can be added into this wire magnet in order to strengthen the magnetic field. The whole setup is mounted on an optical table to minimize mechanical vibrations (Figure 2.7).

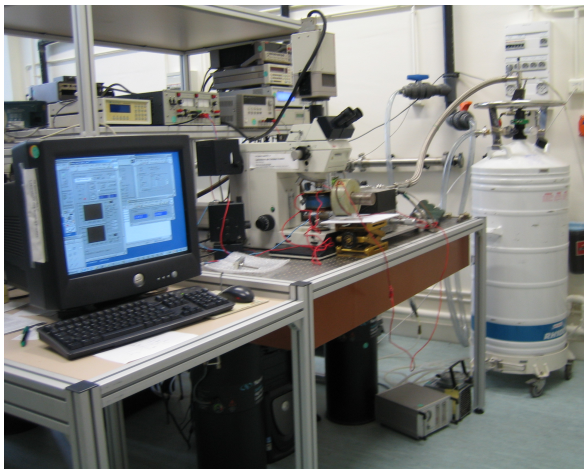

(a)

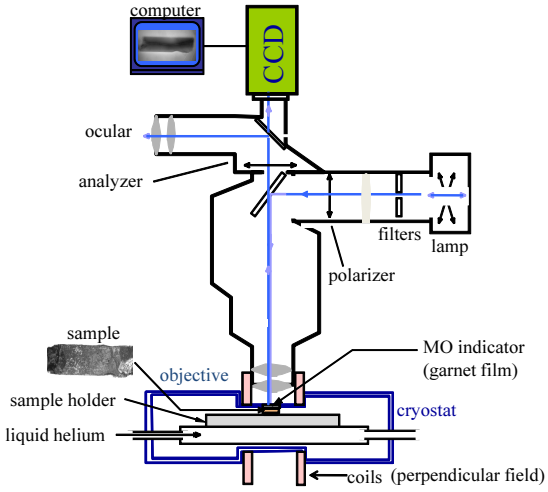

(b)

Figure 2.7: (a) Photo of the experimental set-up at LSI for magneto-optics. (b) Scheme of the experimental setup.

(1) Cooling system and temperature control

A transfer line links a helium storage dewar to the cryostat. Liquid helium flows through the inner tube of this line to the heat exchanger of the cryostat. The returning helium gas flows along the outer tube of the line to the exhaust port. The exhaust line is linked to a helium gas flow controller and a small diaphragm pump. With the controlled flow of helium, the MicrostatHe® cools down quickly. The set-up permits us to reach a minimum temperature of 6 K. The temperature of the sample holder could be stabilized (variation ≤ 0.02 K) in a broad range (from 10 K to 500 K) using a temperature controller (Lakeshore 340). However, the liquid helium flow rate must be regulated by the experimenter depending on the temperature range.

(2) Probes for measuring the temperature and the magnetic fields

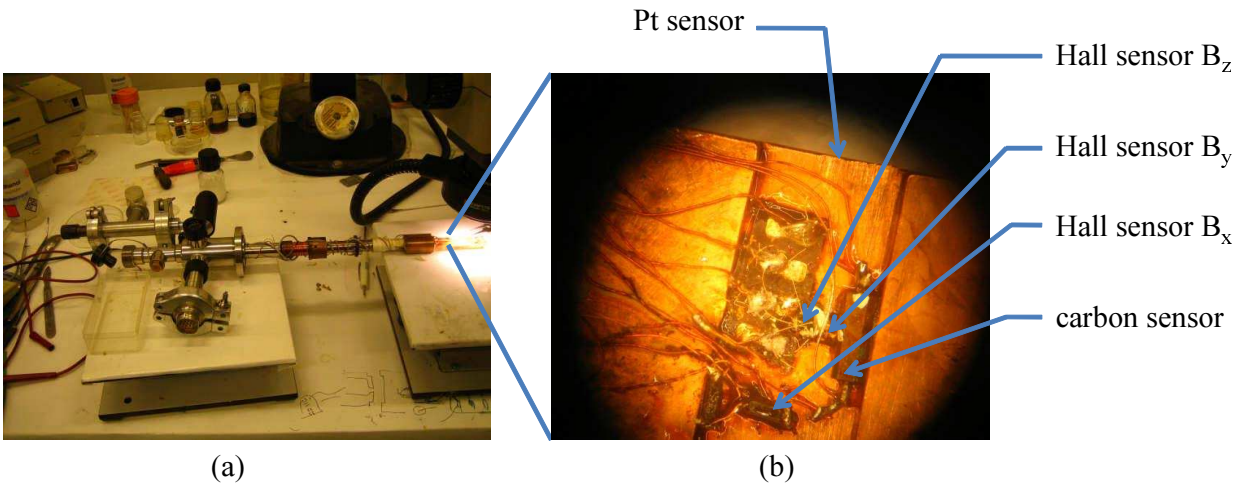

Figure 2.8: (a) Photo of the MicrostatHe®. (b) Photo of the sample holder and placement of the sensors. The sensors are situated near to the sample, but in the opposite side of the sample holder.

Two temperature sensors (Pt-sensor and Allen-Bradley carbon sensor) were glued on the sample holder in order to measure the temperature. Three Hall probes are used for measuring the magnetic field components (B_x, B_y,B_z). These are positioned near to the sample on the opposite side of the sample holder (see Photo 2.8 (b)).

The electrical access onto the MicrostatHe® system (see Photo 2.8 (a)) is via a 10-pin connector and an additional 19-pin Amphenol connector. The connections (1, 2, 3, 4) are for carbon sensor, (5, 6, 7, 8) are for Schlumberger Hall probe to measure the B_z field, (9, 10, 13, 14) and (11, 12, 13, 14) are for two Toshiba Hall probes to measure the B_x and the B_y fields. (15, 16, 17, 18) are reserved for 4-wire resistivity measurements. 19 is not connected.

(3) Camera system

We use a Hamamatsu C4742-98 peltier cooled gray-scale charge-coupled device (CCD) camera. Images acquired by the camera are digitized by 16-bit analog-to-digital converters located on the CCD chip and then transferred to the computer. With this camera, the scale conversion factor for objective $10\times$ of the microscope is about 1 pixel/μm.

(4) Spatial resolution

In our case, the spatial resolution is determined by the thickness of the indicator. Because the magnetic field contrast is significantly attenuated with increasing distance from the sample surface, it is important that the magneto-optical film side is placed in intimate contact with the surface of the sample for maximum spatial resolution. Our apparatus permits a spatial resolution about $5 \sim 10\ \mu m$.

(5) Time resolution

The magneto-optical imaging technique has a great advantage for the study of dynamic processes. In principe, the time resolution is only limited by the spin reversal in the indicator, which occurs on a time scale of nanoseconds. In practice, when we record the magneto-optical images with a CCD camera and transfer to a computer for processing, the time resolution is limited by the image detector and image transfer time (about 40 ms for our apparatus).

2.4.1 Application of direct magneto-optical imaging to superconductors

If a magneto-optical image is acquired in a single shot, one calls it as a *direct magneto-optical* image. One can also perform differential measurements by subtracting two direct magneto-optical images acquired under different conditions, e.g., at two different magnetic fields, or two different temperatures, with or without a transport current, etc. Images acquired in this manner are called *differential magneto-optical* images. We present the direct magneto-optical imaging to superconductors first, then the differential magneto-optical imaging to superconductors with different kinds of modulation is discussed.

We carefully glue the superconductor samples to a copper sheet with n-$C_{19}H_{40}$, a polymer the melting temperature of which is around 30 °C, then we mount them in the cryostat. The MO-indicator is placed with mirror side down on the superconductor sample. The magneto-optical image in Figure 2.9 shows that the field does not penetrate into the superconductor (black corresponds to zero field). The magnetic field lines bend

around the superconductor due to the screening effect, and thus concentrate near the edges which are the brightest areas on the image.

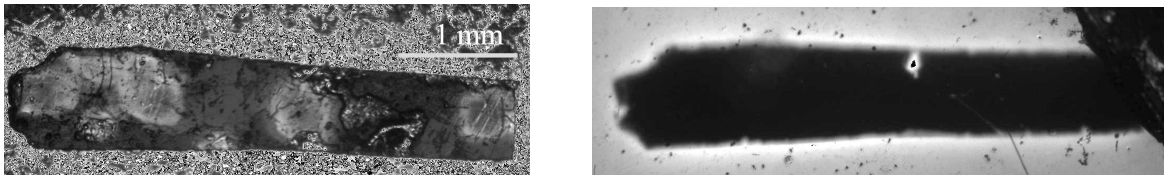

(a) (b)

Figure 2.9: Screening of magnetic field by a superconducting sample observed with magneto-optical imaging. (a) Photograph of the crystal *BSCCO "24-2"*. (b) Direct MO image of *BSCCO "24-2"* acquired at T = 7 K, $H_{//c}$ = 456 Oe, zero-field cooling.

The magnetic flux penetrates a sample from outside to the inside. In a superconductor, flux pinning counteracts flux penetration into the bulk. In Bean's model, also called the *critical state model*, only three values are allowed for the electric current density: zero current for regions where no magnetic flux has penetrated and $\pm j_c$ elsewhere; the sign is determined by Lenz's law and the progression of the current reversal front from the sample boundary. The flux density gradient is constant and given by the value of the critical electric current through the Equation: $\nabla \times \mathbf{B} = \mu_0 \mathbf{j}_c$.

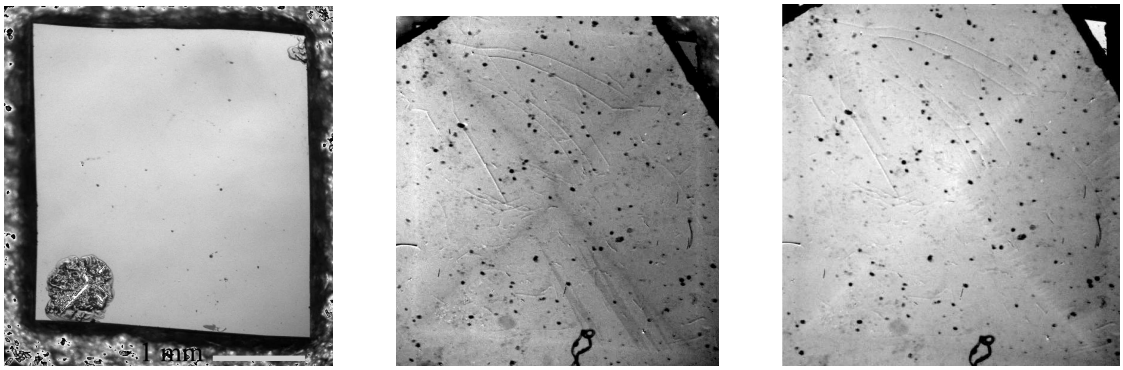

(a) (b) (c)

Figure 2.10: (a) Photograph of the NbN film. (b) Direct magneto-optical image at full penetration, T = 11 K. (c) Direct magneto-optical image at its remanent state after full penetration, T = 11 K.

Here we report the experimental results performed on a NbN thin film (T_c = 14 K). The film was prepared by IFPAN (Institute of Physics of Polish Academy of Sciences) in Warsaw. The NbN film has a thickness of 76 nm and is deposited on a 12 nm thick Pt-Co layer. These two layers are grown on Si substrate. Figure 2.10 (b) shows a direct MO image at full penetration state of this film and Figure 2.10 (c) shows a direct magneto-optical image at its remanent state after full penetration. The magnetic field is applied perpendicular to the plane of the NbN film.

2.4.2 Interpretation of magneto-optical imaging at its differential mode

The influences due to the inhomogeneity of the indicator and the non-uniform illumination can be strongly reduced by a subtraction of the background. Also, an increased signal-to-noise ratio can be obtained by repeating this differential measurement. A. Soibel et al. have used this technique that they pioneered to observe the vortex-lattice melting process in $Bi_2Sr_2CaCu_2O_8$ in the presence of disorder [36] with field and temperature modulations. The measurement can be done in different ways. First of these is the Differential Magneto-Optical (DMO) imaging with field modulation, since this is the most widely employed method in our further study.

The field modulation protocol is as follows: one acquires a magneto-optical image denoted as M_1 at a magnetic field H_1, and another magneto-optical image denoted as M_2 at another magnetic field H_2; then one subtracts M_1 from M_2, pixel by pixel, to obtain the differential image $M_{Diff} = M_1 - M_2$.

We follow the notation of section 1.2.2: K_0 denotes the background intensity; E_0^2 denotes the incident light intensity; The angle α denotes the deviation angle from the fully crossed relative orientation between the analyzer and the polarizer; $\theta(B)$ is the Faraday rotation angle created by the perpendicular magnetic field at the position of the garnet film (the so-called MO indicator).

Let us now consider the differential signal yielded by subtraction of two direct MO images acquired under two different magnetic fields H_1 and H_2. I_1 and I_2 denote the light intensities of the two magneto-optical images respectively. B_1 and B_2 denote the corresponding local magnetic flux density at the top surface of the sample under consideration, which is covered by the MO indicator. Remember that H_1 and H_2 are the applied external magnetic field strengths, and they take constant values in space while B_1 and B_2 depend on the positions in the sample. Since the magneto-optical image is a map of the local magnetic flux density at the sample surface (lying in the xy plane), the spatial dependence of $B(x,y)$ can be derived explicitly from:

$$I_1(x,y) = K_0 + E_0^2 sin^2[\alpha + \theta_{B_1}(x,y)] \tag{2.11}$$

and

$$I_2(x,y) = K_0 + E_0^2 sin^2[\alpha + \theta_{B_2}(x,y)]. \tag{2.12}$$

The differential intensity I_{diff} is:

$$\begin{aligned} I_{diff}(x,y) &= I_1(x,y) - I_2(x,y) \\ &= E_0^2\{sin^2[\alpha + \theta_{B_1}(x,y)] - sin^2[\alpha + \theta_{B_2}(x,y)]\} \\ &= E_0^2\{[\frac{1}{2} - \frac{1}{2}cos(2\alpha + 2\theta_{B_1}(x,y))] - [\frac{1}{2} - \frac{1}{2}cos(2\alpha + 2\theta_{B_2}(x,y))]\} \\ &= E_0^2 sin(\theta_{B_1}(x,y) - \theta_{B_2}(x,y)) \cdot sin(2\alpha + \theta_{B_1}(x,y) + \theta_{B_2}(x,y)) \end{aligned} \tag{2.13}$$

We recall the linear relation: $\theta = kB$, where k is a characteristic constant of the indicator film ($k \approx 0.01^\circ$/G for the indicator film that we use).

Equation (2.13) can thus be written as:

$$I_{diff}(x,y) = E_0^2 sin[k(B_1(x,y) - B_2(x,y))] \cdot sin[2\alpha + k(B_1(x,y) + B_2(x,y))] \tag{2.14}$$

Using the approximation: $sin(x) \doteq x$ for $x \ll 1$, one gets:

$$I_{diff}(x,y) \doteq kE_0^2(B_1(x,y) - B_2(x,y)) \cdot [2\alpha + k(B_1(x,y) + B_2(x,y))] \tag{2.15}$$

If one defines $\Delta B(x,y) \equiv B_1(x,y) - B_2(x,y)$ and $B(x,y) \equiv \frac{B_1(x,y)+B_2(x,y)}{2}$, then Equation (2.15) reads:

$$I_{diff}(x,y) \doteq 2kE_0^2 \Delta B(x,y) \cdot [\alpha + kB(x,y)] \tag{2.16}$$

The *apparent differential magnetic permeability* μ is defined as[2]: $\mu_H \equiv \frac{dB(H)}{dH}$. Applying this definition locally, one replaces $\Delta B(x,y)$ by $\mu_H(x,y)\Delta H$ in Equation (2.16), where $\mu_H(x,y)$ is called the *local differential apparent magnetic permeability*, or *local "permeability"* for short, measured under an external magnetic field H, and then one obtains:

$$I_{diff}(x,y) \doteq 2kE_0^2 \mu_H(x,y) \Delta H \cdot [\alpha + kB(x,y)] \tag{2.17}$$

If H_1 and H_2 are sufficiently close, $B_1(x,y)$ and $B_2(x,y)$ should be close also to their average value $B_H(x,y) \equiv \frac{B_1(x,y)+B_2(x,y)}{2}$. For simplicity, one defines a constant $C \equiv 2kE_0^2$ and then Equation (2.17) reads:

$$I_{diff}(x,y) \doteq C\Delta H \cdot [\alpha + kB_H(x,y)]\mu_H(x,y). \tag{2.18}$$

Equation (2.18) provides the following interpretation concerning the DMO image with field modulation: the differential signal with field modulation is the square root of the direct image intensity (ignoring the background intensity K_0) multiplied by the *local apparent differential magnetic permeability*.

In a typical measurement, α is set around 2°. Analysis shows that in order to achieve an optimal image contrast, the value of α should be set between $1^\circ \sim 6^\circ$ depending on the extinction ratio of the polarizer. Furthermore, $k \approx 0.01^\circ$/G, and the field range of our experiments lies between 0 and 400 Oe. The value of $kB_H(x,y)$ is thus between 0 and 4°, which is of the same order as the value of α and therefore cannot be neglected.

The interpretation of DMO (differential magneto-optical) images with field modulation as a map of the *local "permeability"* is valid in the situations listed below:

[2] As a matter of fact, the definition of this *apparent local differential magnetic permeability* is not necessary for the discussions. While defining this quantity permits one to compare with magnetic materials.

1. The spatial variation of $B(x,y)$ can be ignored in Equation (2.18). Consequently, $B_H(x,y)$ is replaced by a constant $C^{'}$ and Equation (2.18) reduces to $I_{diff}(x,y) \doteq CC^{'}\Delta H\mu_H(x,y) \propto \mu_H(x,y)$. This is the case for the study of magnetic films by the magneto-optical imaging technique. For high-T_c superconductors, the screening current density is nearly zero when sufficiently close to their irreversibility lines; Then, $B_H(x,y)$ is almost uniform and the DMO images with field modulation can be interpreted as a map of the local "permeability".

2. $B_H(x,y)$ is sufficiently small compared to α/k, i.e., $B_H(x,y) << \alpha/k$, then the spatial variation of $\alpha + kB_H(x,y)$ due to $B_H(x,y)$ can be ignored and Equation (2.18) reduces to $I_{diff}(x,y) \doteq C\Delta H \cdot \alpha \cdot \mu_H(x,y) \propto \mu_H(x,y)$.

In the case that the spatial variation of local "permeability" is negligible, the differential image resembles the direct image. Furthermore, since the differential measurement can significantly reduce perturbations due to the inhomogeneity of the indicator film and the non-uniform illumination, one obtains a neater magneto-optical image using the differential measurement. By repeating this differential operation, the signal-to-noise ratio S/N_N is raised ($S/N_N = S/N_0 \cdot \sqrt{N}$, where S/N_0 is the signal-to-noise ratio of one single frame, N is the number of averaged frames) and a resolution of 0.1 G can be attained in our set-up with this differential image acquisition procedure[3].

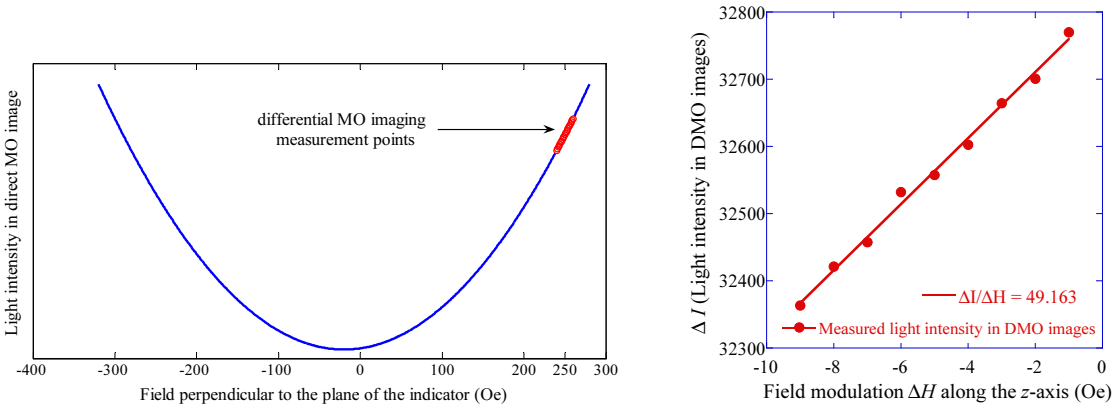

Figure 2.11: (a) Quadratic relation between the light intensity I and the magnetic field H perpendicular to the plane of the indicator in direct magneto-optical image. (b) Averaged intensity of the acquired calibration DMO images as a function of the modulation field. DMO images are acquired at T = 85 K, base field H_z = 250 Oe, modulation field varied from -1 Oe to -9 Oe (along the z-axis).

In direct image mode, there is a quadratic relation between the light intensity I and the magnetic field intensity H perpendicular to the plane of the garnet film (MO indicator):

[3] Normally 200 frames are averaged to obtain this resolution.

$I = K_0 + E_0^2(\alpha + kB)^2$, as illustrated in Figure 2.11 (a). Since the polarizer and the analyzer are nearly crossed, i.e., $\alpha \approx 0$, the bright regions in a direct MO image correspond to high field regions. In differential mode, if the magnetic flux density $B_H(x,y)$ is uniform, e.g., when one acquires an image of the sole indicator film only or of the superconducting sample in the normal state covered by the indicator, Equation (2.18) yields $\Delta I \propto \Delta H$. This linear relation between the light intensity ΔI in DMO image and the value of the modulation field ΔH has been verified experimentally (see Figure 2.11 (b)).

2.4.3 Differential magneto-optical imaging of superconductors

For superconductors, bulk pinning and surface barrier govern the dynamics of vortex motion, as well as the spatial distribution of the vortex density, i.e., the spatial distribution of the magnetic flux density. The critical-state model (Bean's model) incorporates the bulk pinning effect and permits one to study the distribution of magnetic flux density. In the following, we apply Bean's model into Equation (2.15) and provide interpretations of DMO images with field modulation perpendicular to the sample plane.

DMO imaging with field modulation perpendicular to the sample plane

The differential intensity given by Equation (2.15) can be rewritten as:

$$I_{diff}(x,y) \doteq k^2 E_0^2 [B_1(x,y) - B_2(x,y)] \cdot [2\alpha/k + B_1(x,y) + B_2(x,y)] \tag{2.19}$$

If one considers the case for a thick sample and a one dimensional approximation is justified (e.g., slab), using the Bean's model: $dB/dx \sim j_c$, one thus has:

$$d[2\alpha/k + B_1(x) + B_2(x)]/dx \sim 2j_c \tag{2.20}$$

and

$$d[B_1(x) - B_2(x)]/dx \sim C_0 j_c \sim 0 \tag{2.21}$$

where C_0 is a constant and $C_0 \sim 0$.

Applying the above results to Equation (2.19) to calculate the gradient of the differential intensity I_{diff}, one obtains:

$$dI_{diff}(x)/dx \sim 2k^2 E_0^2 \mu_H \Delta H \cdot j_c \tag{2.22}$$

where one uses the definition of the local magnetic permeability μ_H and replaces $B_1(x,y) - B_2(x,y)$ by $\mu_H \Delta H$, with $\Delta H \equiv H_1 - H_2$. The gradient of the intensity in the field modulated DMO images is thus related to the critical current density value. If this gradient is no longer discernable, i.e., when one can no longer distinguish the superconducting region from the surrounding background in a field modulated DMO image, the critical

current density value vanishes to zero. The irreversibility line can thus be determined in this manner from field modulated DMO images.

The DMO images in Figure 2.12 are obtained on the same NbN film as that in Figure 2.10. Figure 2.12 shows the partial magnetic field penetration pattern into this NbN film at T = 11.65 K at different applied magnetic fields perpendicular to its plane with a fixed modulation field ΔH_a = 5 Oe.

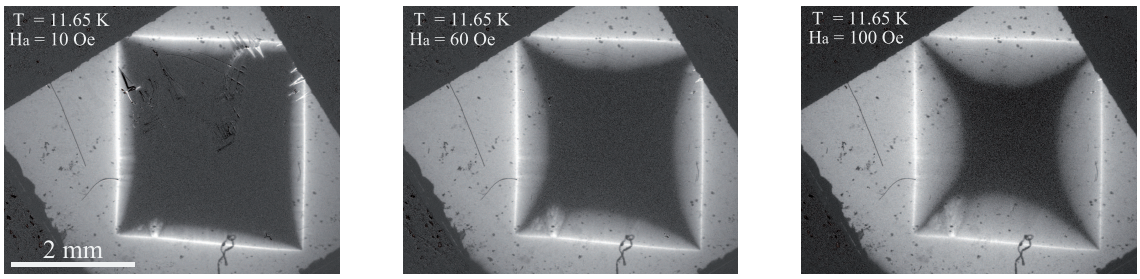

(a) (b) (c)

Figure 2.12: Differential magneto-optical images acquired at T = 11.65 K. The modulation field is 5 Oe. (a) Base field H_a = 10 Oe. (b) Base field H_a = 60 Oe. (c) Base field H_a = 100 Oe.

As we have pointed out previously, field modulated DMO imaging can be used to determine the irreversibility line for superconductors. Figure 2.13 shows the DMO images with base field H_a = 0 at different temperatures in the vicinity of T_c on the same NbN film (T_c = 14 K) as in Figure 2.10 and 2.12. Figure 2.13 shows that approaching T_c, the gradient of the intensity in DMO images vanishes.

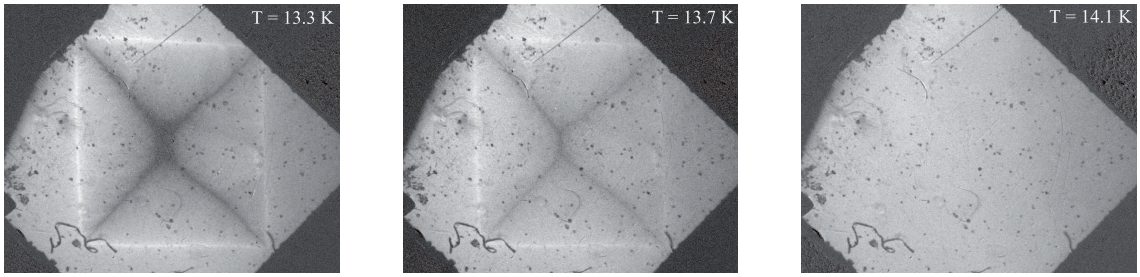

(a) (b) (c)

Figure 2.13: Differential magneto-optical images acquired at different temperatures. (a) The image was acquired at T = 13.3 K, base field H_a = 0 Oe, and modulation field ΔH_a= 5 Oe. (b) The image was taken at T = 13.7 K, base field H_a = 0 Oe, and modulation field ΔH_a= 5 Oe. (c) The image was acquired at T = 14.1 K, base field H_a = 0 Oe, and modulation field ΔH_a= 5 Oe.

DMO imaging with field modulation parallel to the sample plane

In a direct MO image, the light intensity I is:

$$I \approx K_0 + E_0^2(\alpha+\theta)^2$$

where K_0 is the off-set light intensity, E_0^2 is the incident light intensity, $\theta = kB_\perp$, the proportionality constant $k \approx 0.01^\circ/G$, $B_\perp$ is the magnetic flux density perpendicular to the garnet film (MO indicator). Now we discuss the situation with field modulation, denoted as H_{ac} in Figure 2.14, parallel to the sample plane.

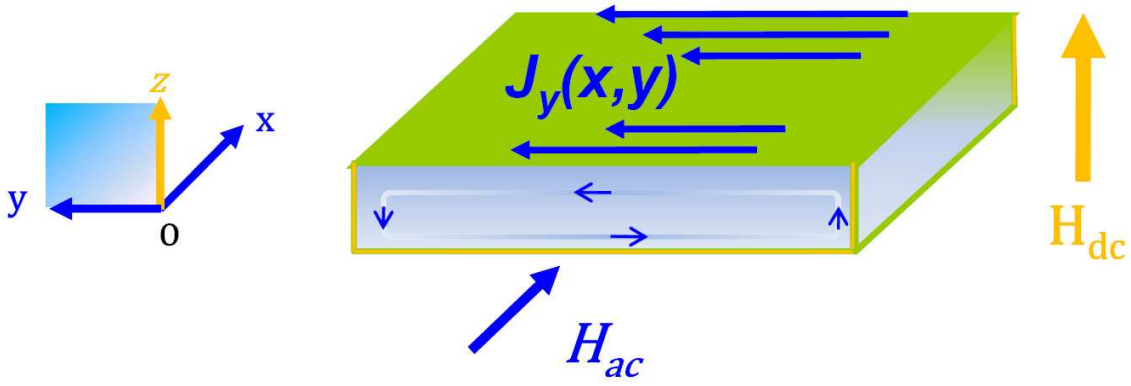

Figure 2.14: Field configuration: dc magnetic field is applied along the z-axis; The modulation field H_{ac} is applied along the x-axis.

The dc field H_{dc} induces a shielding current I_{dc} in the superconducting sample. The ac field H_{ac} induces an ac screening current I_{ac} in the superconducting sample. B_{ac} denotes the z-component of magnetic field generated by I_{ac} and B_{dc} denotes the z-component of magnetic field generated by I_{dc}. Let us denote the Faraday rotation angle due to the dc field as $\theta|_{dc}$ and the Faraday rotation angle due to the ac field as $\theta|_{ac}$, one has: $\theta|_{dc} = kB_{dc}$ and $\theta|_{ac} = kB_{ac}$. In the presence of both of an ac field and a dc field, one has $\theta|_{ac\&dc} = k(B_{ac}+B_{dc})$.

Without the ac field, the light intensity is:

$$I_0 = K_0 + E_0^2(\alpha+\theta|_{dc})^2 \tag{2.23}$$

With the presence of the ac field, the light intensity is:

$$I_{ac} = K_0 + E_0^2(\alpha+\theta|_{ac\&dc})^2 \tag{2.24}$$

The light intensity in the resulting differential image I_{diff} is thus:

$$\begin{aligned} I_{diff} = I_{ac} - I_0 &= E_0^2(\alpha+\theta|_{ac\&dc})^2 - E_0^2(\alpha+\theta|_{dc})^2 \\ &= E_0^2(\theta|_{ac\&dc} - \theta|_{dc})(2\alpha+\theta|_{ac\&dc} + \theta|_{dc}) \\ &= k^2E_0^2B_{ac}(2\alpha/k + B_{ac} + 2B_{dc}) \end{aligned} \quad (2.25)$$

Strictly speaking, the linear relation between I_{diff} and B_{ac} is only achieved once the condition B_{ac}+$2B_{dc} \ll 2\ \alpha/k$ is satisfied. This condition can be met by choosing a large enough value of α. If one defines $I_{diff}|_{ac} \equiv k^2E_0^2B_{ac}$, Equation (2.25) can be rewritten as:

$$I_{diff} = I_{diff}|_{ac}(2\alpha/k + B_{ac} + 2B_{dc}) \quad (2.26)$$

DMO imaging with current modulation

Now we move to discuss the DMO imaging with current modulation: a dc magnetic field is applied perpendicular to the sample plane, while a transport current is applied parallel to the plane of the sample. For example, one can consider that the transport current is applied along the *y*-axis as illustrated in Figure 2.14. Following the same calculations as one has done for DMO imaging with field modulation parallel to the sample plane, one finds that the light intensity difference, with the presence of the transport current and without this transport current, is:

$$I_{diff} = k^2E_0^2B|_{current}(2\alpha/k + B|_{current} + 2B_{dc}),$$

where $B|_{current}$ is the *z*-component of the magnetic field (the so-called *self-field*) generated by the transport current. The differential signal is thus the *self-field* signal of the transport current convoluted with the applied dc magnetic field signal.

2.4.4 Visualization of the vortex-lattice melting transition with differential magneto-optical technique

To visualize the vortex-lattice melting transition with MO imaging technique, the task is to observe a magnetic flux density difference of $0.1 \sim 0.4$ Gauss in a background (on the order of hundreds of Gauss) which appears as a *bright ring* (see Figure 2.15), which indicates the location of the expanding solid-liquid interface, on a dark background of a noise level about 0.5 Gauss with differential magneto-optical imaging technique.

In the studies undertaken by A. Soibel et al. [36]-[38], they discussed the situation where the bulk pinning is absent, i.e., the task is then to observe a magnetic flux density difference of $0.1 \sim 0.4$ Gauss in a unform background where only *white noise* is present.

In the situation where the bulk pinning is present, and the irreversibility line is higher or superposed with the first-order melting transition line on *H-T* phase diagram, then the *dome-shaped* profile shown in Figure 2.15 (a) for the vortex density distribution (with a maximum vortex density at the center) should be replaced by Bean's profile. In this case, the observation of the vortex-lattice melting transition, i.e., the observation of the *bright ring* would be rather difficult.

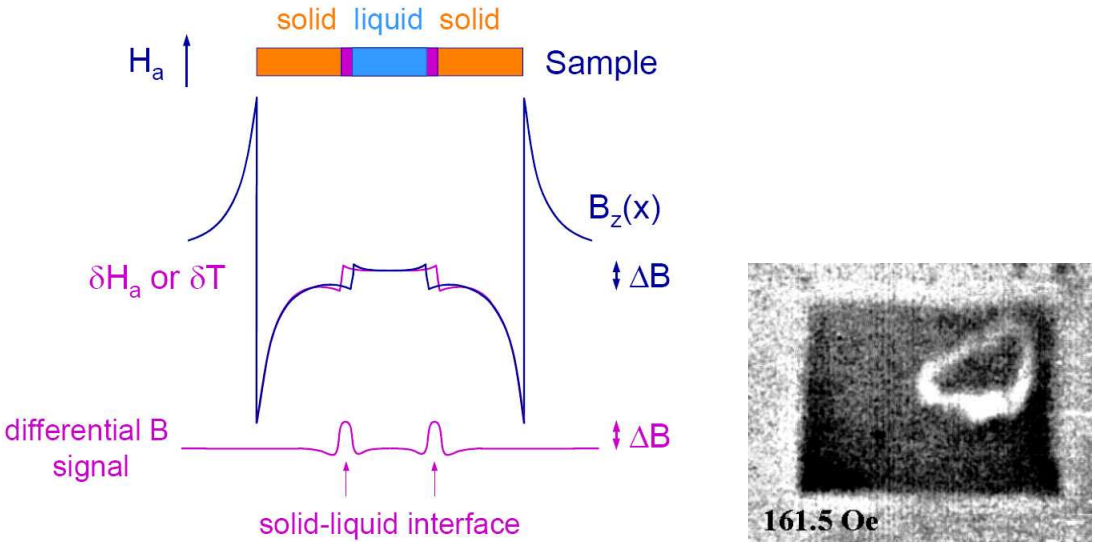

Figure 2.15: (a) Schematic illustration of visualization of vortex-lattice melting by differential magneto-optical technique. The field B in the liquid phase is larger by ΔB than in the solid (blue profile). Figure from Ref. [38]. (b) DMO image of the melting process in a *BSCCO* crystal (T_c = 91 K) of area 0.35×0.27 mm^2 at T = 60 K, δH_a = 1 Oe and H_a is along the c-axis. The *bright ring* indicates the location of the expanding solid-liquid interface. Image from Ref. [38].

For example, as shown in Figure 2.11 (b), a 1 G signal corresponds to a difference of 40 on the gray-level in a DMO image obtained with a 16-bit CCD (gray-level value situates between $0 \sim 65536$). The theoretical magnetic flux density resolution limit is then 1 G/40 = 0.025 G. The spatial resolution of the common optical microscope is 10 μm, which corresponds to 10 pixels with a 10× magnification objective and the 16-bit CCD camera that we use in our measurements. In the presence of bulk pinning and if one applies Bean's approximation, i.e., the vortex density has a gradient $\frac{dB(x)}{dx}$ which is proportional to the critical current density j_c. Then the local vortex density resolution is determined by the product of j_c and the spatial resolution. For example, if the gradient $\frac{dB(x)}{dx}$ is 0.01 G/μm, then the vortex density resolution is 0.01 G/μm × 10 μm = 0.1 G. In this case, to observe the melting by differential magneto-optical imaging, one needs to be able to resolve a magnetic flux density difference of 0.1 G, which yields the *bright ring*,

in a *heterogeneous background* where both a *white noise* and a *vortex density gradient* are present. This is a more difficult task. Following this argument, the *bright ring*, i.e., location of the expanding solid-liquid interface, is easier to observe in a crystal where the bulk pinning is weak (and the surface barrier effect is strong) than that where the bulk pinning is strong (and surface barrier effect is weak).

Chapter 3

Transport measurements for $Bi_2Sr_2CaCu_2O_8$ single crystals

Resistivity measurements permit one to study the motion of vortices in type II superconductors. The resistivity is not a thermodynamic property as the equilibrium is disturbed by the transport current. However, resistivity measurements can show the signature of phase transitions of the vortex system since the resistive properties may change dramatically between different phases. For example, a sharp decrease of resistance may be observed during the vortex liquid to vortex solid transformation. In order to measure a resistance, one needs to inject a current, I, with a current source and measure the voltage, V, through a voltmeter. The resistance R is defined by the formula $R = V/I$. If the ratio is constant over a wide range of currents and voltages, the material is said to be *ohmic*. If the ratio depends on the current and voltage applied, the material is said to be *non-ohmic*. Four-point probe measurements should be used for low resistances.

3.1 Fabrication of the electrical contacts on $Bi_2Sr_2CaCu_2O_8$ single crystals by photolithography

We began by using the silver paint and gold wires of 50 μm to establish the electrical contacts on sputtered gold pads as illustrated in Figure 3.1 (a). The contact resistance is about several Ohms for the best cases, however, the contacts achieved by this way cannot resist cooling.

In order to obtain high quality electrical contacts, we used a method of fabrication with thin Au contacts on the top of the crystals *BSCCO* by photolithography, which do not disturb the magneto-optical imaging. Photolithography is the photographic transfer of a pattern to a surface. During this process the electric contacts have been established using a chromium photomask. This part of work was done in the cleanroom of the laboratory Unité Mixte de Physique CNRS/Thales (UMR 137).

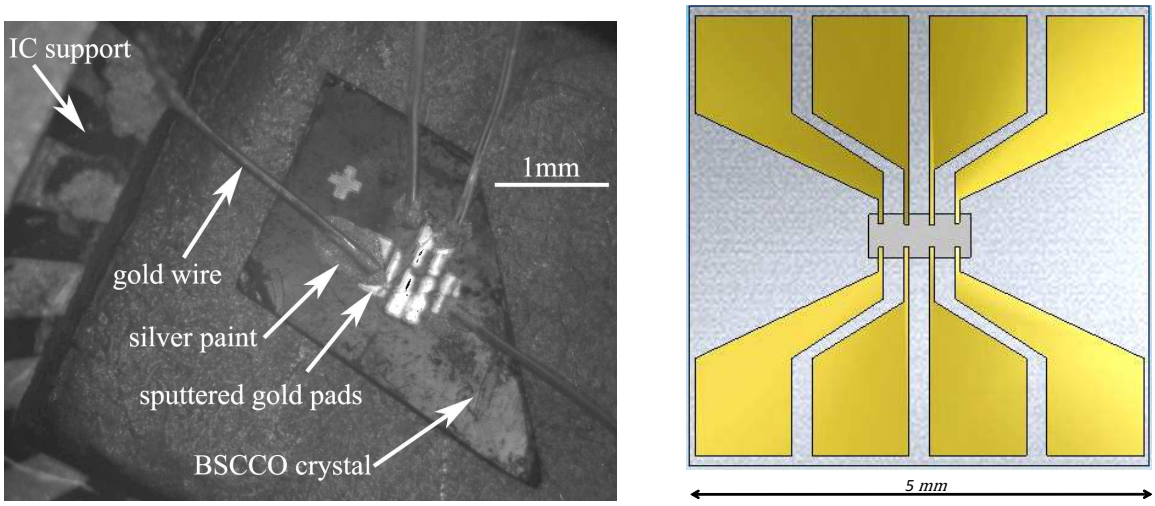

(a) (b)

Figure 3.1: (a) Electrical contacts established with silver paint on the crystal *BSCCO "15"*. (b) Designed mask for photolithography.

We have designed 4 photomasks of the same pattern illustrated in Figure 3.1 (b) for different sizes of the crystals: 500 μm, 750 μm, 1000 μm, and 1500 μm. The outer contact pads are designed for current injection and the inner contact pads are designed for voltage measurements. A shadow mask is fabricated using photolithography and etching and includes designed pattern for 4 different sizes mentioned above.

There are two methods for fabrication of the electrical contacts by photolithography: the *"lift-off method"* and the *"chemical etching method"*. We have tested both and have chosen the "chemical etching method" for our work since we found that with the *"lift-off method"* the gold layer evaporated on the sample seemed difficult to remove (after 2 days immersed in Acetone) from the regions where it was not desired. Before performing photolithography, the *BSCCO* single crystals are glued onto the sapphire substrate.

3.1.1 Gluing the *BSCCO* single crystals onto the sapphire substrate

The *BSCCO* crystals are glued to sapphire substrates[1] using the Norland Optical Adhesive ("NOA 61"). The glue is applied specifically to compensate the thickness of the crystals ($\sim$ 20 μm) and provide a smooth ramp between the sample's top edges to the sapphire surface (Figure 3.2). The steps for the utilization of the NOA 61 glue are detailed as follows:

1. Clean a sapphire substrate (Figure 3.2 (a)).

[1] We choose sapphire as the substrate for its good thermal conductivity and high transmittance for UV light along its *c-axis*.

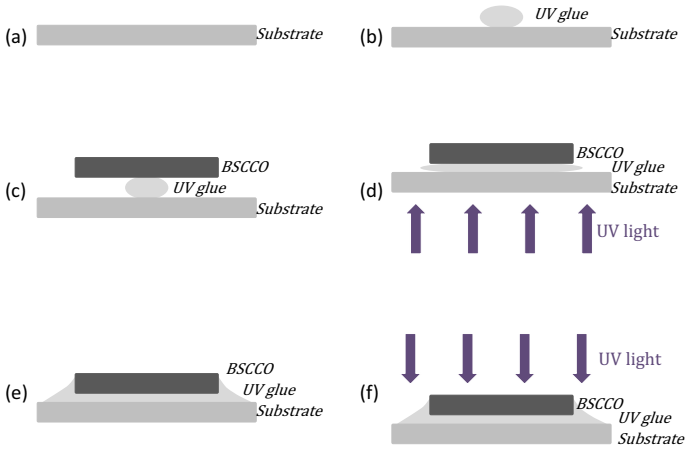

Figure 3.2: Steps for the utilization of the NOA 61 glue.

2. Put a small drop of the "NOA 61" glue onto the sapphire substrate surface (Figure 3.2 (b)).

3. Position the *BSCCO* single crystal on the drop of the "NOA 61" glue (Figure 3.2 (c)).

4. Precure with a 100 Watt UV light for 10 seconds; The precure allows one to fix the single crystal on the sapphire substrate. After the precure, excess adhesive can be wiped up with alcohol or acetone (Figure 3.2 (d)).

5. Add and adjust the quantity of "NOA 61" glue to form a ramp under an optical microscope (Figure 3.2 (e)).

6. Final cure with a 100 Watt UV light for 10 minutes (Figure 3.2 (f)).

3.1.2 Chemical etching process

Here are the steps for the chemical etching process that we used:

1. Plasma etching for cleaning the surfaces of the crystals: 2 minutes in a plasma Ar/O_2 (ratio 1:4) with a pressure of 1×10^{-2} mbar and a power of 15 W.

2. Evaporation of a 500 nm gold layer. (Plasma Ar, 2.5×10^{-3} mbar, DC current 200 mA, deposit speed of 0.8 nm/s)

3. Cover the sapphire (5×5 mm^2) with primer (spun at 6000 rpm for 30 seconds) and then with S1813 photoresist (spun at 6000 rpm for 1 minute). The layer of the photoresist is about 1 μm thick obtained with the above parameters.

4. Heat at 90°C for 1 minute.

5. Expose to UV light through the *negative* mask: 40 mJ. The photoresist in the exposed regions will be dissolved in the developper in the following step. The gold in the exposed regions will be removed later since in these regions, the gold is not protected by the photoresist layer anymore.

6. Development by Microposit Developer MF319 (1 minute and 30 seconds), and rinse with deionized water (3 minutes) to stop the chemical reaction.

7. Verification under an optical microscope.

8. Etching with KI_2 (45 seconds), and rinse with deionized water.

9. Plunge the sample in acetone to dissolve the resist covering the surface of the remaining gold layer, and then plunge the sample in propanol to remove the acetone trace.

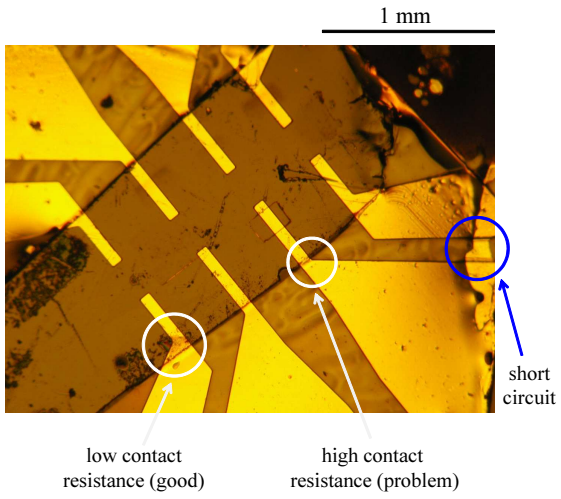

Figure 3.3: Electrical contacts obtained by photolithography for the sample *BSCCO "24-4"*.

Figure 3.3 shows the result achieved by the above method for a *BSCCO* single crystal. The resistance of the contacts is less than several Ohms. The photolithography method described above permits us to obtain sufficiently low resistance contact for a large contact width. While for narrow contact width, the contact resistance could be very high (Figure 3.3). It is possible that some gold is not removed properly during the chemical etching process, one can use a razor blade delicately to remove the gold in the regions where it is not desired, e.g., the short circuit shown in Figure 3.3.

3.1.3 Quality of the contacts

The quality of the contacts manifests itself through the contact resistance. For transport measurements, we expect robust contacts which have sufficiently low contact resistance. Our experience showed that with the method described above, the quality for the narrow width contact is still not satisfactory. We have examined the electrical contacts of the samples with Scanning Electron Microscope. Figure 3.4 shows clearly that there are discontinuities of the gold track at the edges of the sample. In this case, we need to add some silver paint at the edges to *"repair"* the contact for transport measurements.

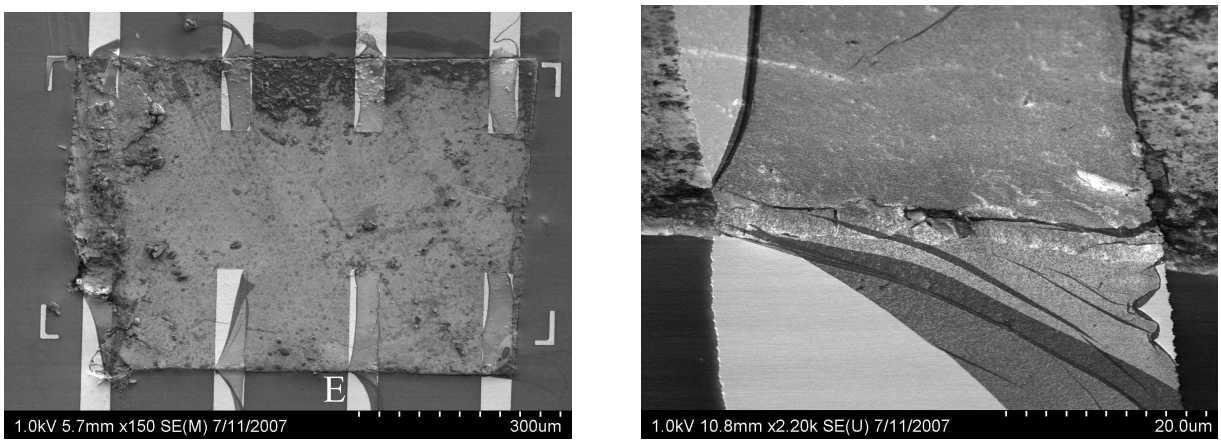

(a) (b)

Figure 3.4: (a) Scanning Electron Microscope (SEM) image for the sample *BSCCO "11"* (150 ×). (b) SEM image for the contact *"E"* marked on the left-hand figure (2200 ×). The SEM images are acquired by Dr. D. Lucot at the Laboratoire de Photonique et de Nanostructures (CNRS-UPR20), Marcoussis, France.

3.2 Experimental set-up for resistivity measurements

3.2.1 Cryogenic system

The cryogenic system (Figure 3.5) is composed of a helium flow cryostat placed inside a 100-liter dewar filled with liquid helium. The Variable Temperature Insert (VTI) designed by Dr. M. Konczykowski was made by the ABT Sorime company, and equipped with a superconducting magnet (NbTi coil) with I_{max} = 19 A and the proportionality constant of 77 Oe/A, calibrated at the position of the sample with a Hall probe (Toshiba THS118) at low temperatures and with a Gaussmeter at ambient temperature.

The flow of gas helium is regulated by a needle valve (C) at the entrance of liquid helium to the cryostat and a flow meter (D) at the exit of helium gas. The sample space (G) is surrounded by a coil heater. A platinum temperature sensor is placed on the sample

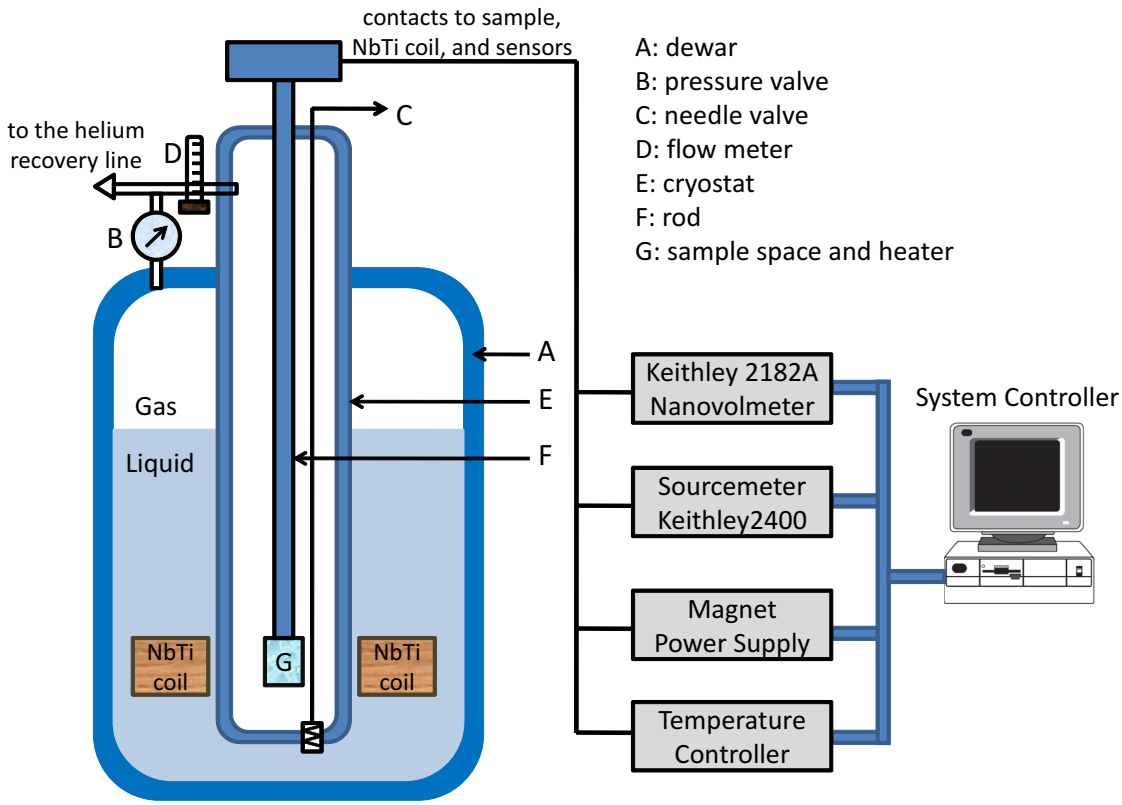

Figure 3.5: The cryogenic and measurement systems.

mount to measure its temperature. We can stabilize the temperature of the sample between 5 K and 300 K with a precision of 20 mK.

3.2.2 Measurement systems

The sample glued to the sapphire substrate ($5 \times 5\ mm^2$) is mounted on a 24-pin IC support. We use a homemade connection box to connect the 24 contacts of the chip to the instruments. The measurement system is composed of (Figure 3.5):

1. Temperature controller Lakeshore 331;
2. Sourcemeter Keithley 2400;
3. Nanovoltmeter Keithley 2182A;
4. Superconducting Magnet Power Supply (Model: CRYOGENIC SMS 10);

5. A computer with a GPIB interface for the control of the instruments and the data acquisition.

In order to cancel the thermal voltage errors in the system, the current is inverted. The final resistance calculation is: $R = (V_1 - V_2)/\mid 2I \mid$ where: R is the resistance of sample understudy, V_1 is the first measured voltage with a current I, and V_2 is the second measured voltage with current of opposite polarity, $-I$. With the trigger link cable between the SourceMeter Keithley 2400 and the Nanovoltmeter Keithley 2182A, the current reversal can be done up to 24 Hz in our set-up.

3.2.3 Noise considerations

In our *dc* resistance measurement, the noise level observed in our resistance data is directly related with the contact resistance. We consider that the main noise in our measurement is due to thermal noise. Thermal noise, also called the Johnson-Nyquist noise ([39], [40]), is the voltage fluctuations caused by the random Brownian motion of charge carriers (usually the electrons) in a resistive medium, which happens regardless of any applied voltage. Thermal noise is a broadband white noise and if modeled by a noise voltage source in series with the resistor of resistance R, the root mean square value of this noise level (nV/$\sqrt{Hz}$) is given by: $V_{noise} = \sqrt{4k_BRT}$, where k_B is the Boltzmann constant and T is the temperature of the resistor.

The resistances of the electrical contacts established between the *BSCCO* single crystals and the Au contacts achieved by photolithography vary from several Ohms to hundreds of Ohms depending on the quality of the contacts. To reduce this noise, we need to achieve low electrical resistance contacts. Our experience showed that with the method described above, very low contact resistance could be obtained for relatively large size *BSCCO* single crystals (for example, for the surface about $1.5 \times 1.5\ mm^2$) while this goal remained difficult to achieve for much smaller *BSCCO* crystals (Figure 3.4). In order to reduce the noise level for small samples with a relatively high contact resistance, the resistance measurements were repeated at a fixed point and the measured values were averaged to give the resistance value for each point of acquisition. For example, for the resistance measurements presented in Chapter 5, in order to achieve a resolution of 10^{-7} Ω with an applied current that does not exceed 10 mA, 1024 measurements had been done at a fixed point and then been averaged to obtain the resistance value.

3.3 The Importance of achieving good quality electrical contacts

When a barrier between the metallic contact (e.g., gold layer in our case) and the superconducting crystals exists, the *V-I* behavior could be perturbed by the presence of this

barrier. In order to obtain good measurements, one wishes to have a low barrier. The following example shows that a sufficient low barrier is primordial to be able to perform resistivity measurements correctly.

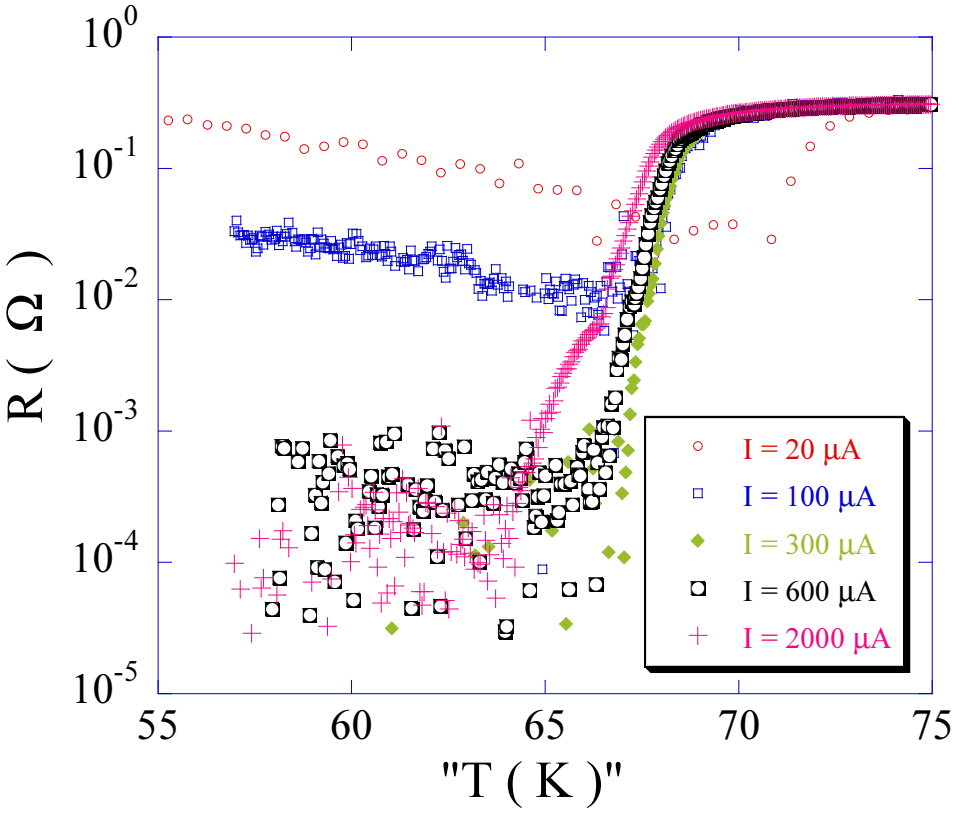

Figure 3.6: Resistance as a function of the temperature measured at zero-field on an optimally doped sample (*BSCCO "20A"*). The thermalization was not good enough and the value for the temperature presented in the above graph was thus not accurate. Since the contact resistance is very high, Joule heating causes the resistance curve shifts with the following currents: 300 μA, 600 μA, and 2000 μA. Due to a barrier between the crystal and the Au layer, current was not injected properly. One can see this from the resistance curves with the applied current of 20 μA and 100 μA.

Figure 3.6 illustrates the perturbation of this barrier to the resistivity measurements. The resistivity curve shifts with the following currents: 300 μA, 600 μA and 2000 μA, are caused by the Joule heating effect due to the large contact resistance while the resistance curve measured with the current of 20 μA and 100 μA indicate clearly that the current was not injected properly. In order to understand this current injection anomaly, we performed *I-V* characterization at T = 60 K (This is the recorded temperature value. Since the thermalization was found to be unsatisfactory, the accurate temperature of the sample was unknown, but from the resistivity curves shown in Figure 3.6, one knows that

the resistance of the *BSCCO* sample $R_{BSCCO} \approx 0$ at this temperature.) as compare with a *bilayer model* detailed below.

The *bilayer model* is shown in Figure 3.7. The electrical contact between the *BSCCO* crystal and Au-layer is contaminated by a barrier. Current should flow through this barrier first, and then flows into the *BSCCO* sample. If one denotes $R_{voltmeter}$ as the internal resistance of the voltmeter, R_{BSCCO} as the resistance of the *BSCCO* crystal, and $R_{barrier}$ as the resistance of the contamination layer (barrier layer), whose value depends on the injection current and can be modeled as: $R_{barrier} = R_0 exp(-I/I_0)$, where R_0 and I_0 are constants, I is the injected current. The measured voltage signal V is then:

$$\begin{aligned} V &= I \frac{1}{\frac{1}{R_{BSCCO}+R_{barrier}} + \frac{1}{R_{voltmeter}}} \\ &= I \frac{1}{\frac{1}{R_{BSCCO}+R_0 exp(-I/I_0)} + \frac{1}{R_{voltmeter}}} \end{aligned} \tag{3.1}$$

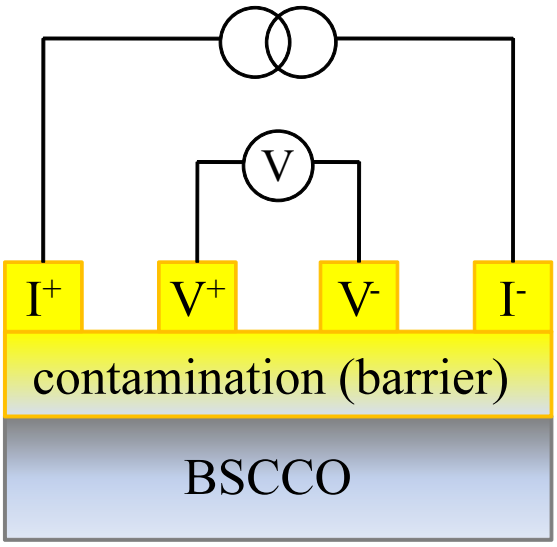

Figure 3.7: Bilayer model for resistance modeling.

When one fits the *I-V* curve with Equation (3.1), one finds very small values for R_{BSCCO}. Setting $R_{BSCCO} = 0$, comparing with the experimental $I-V$ curve, we find the following values for the parameters in Equation (3.1): $R_0 = 0.14858\ \Omega$, $I_0 = 48.291\ \mu$A, $R_{voltmeter} = 1 \times 10^9\ \Omega$. Those values are quite reasonable. Figure 3.8 also shows that this *bilayer model* can explain very well the measured *I-V* characteristics. Combining with the resistance measurement results shown in Figure 3.6, one sees that the quality of electrical

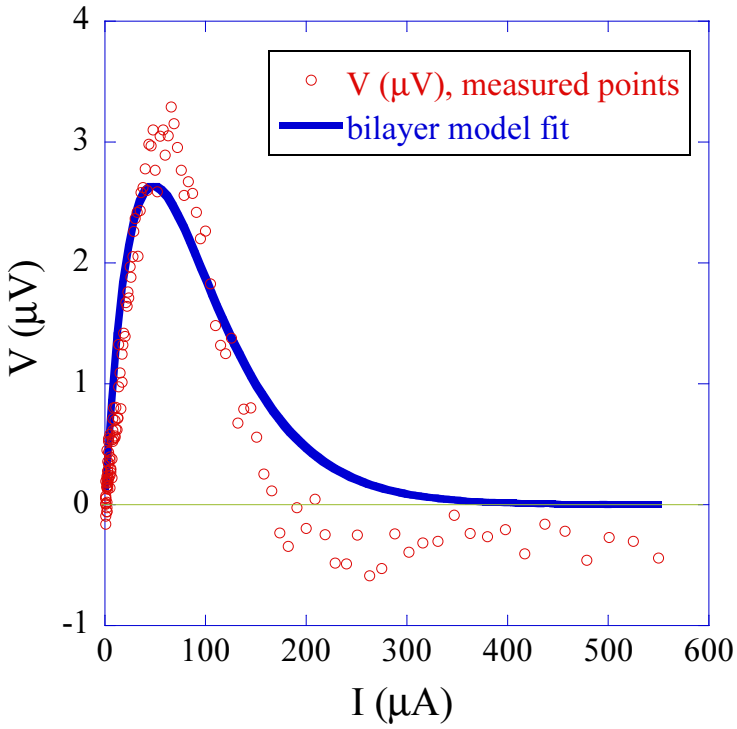

Figure 3.8: Comparison between measured *V-I* curve and the fit according to Equation (3.1).

contacts plays a central role for performing resistance measurements since it not only influences the resolution of the resistance measurements, but also determines whether one can probe correctly the transport properties of the sample understudy.

Chapter 4

Magneto-optical imaging of a superconductor in a NMR experimental configuration

4.1 Motivation

In this chapter, we present a magneto-optical study that aims to clarify the spatial distribution of a time-varying magnetic field and the associated screening current in a superconductor in the geometry where the applied periodic magnetic field is oriented perpendicularly to a static magnetic field. This configuration mimics that used in Nuclear Magnetic Resonance (NMR) experiments. An important question concerning NMR experiments on superconductors is to what extent fields penetrate the material under study, and therefore, to what extent the NMR signal is representative of the material bulk. The motivation of these experiments comes from the recent discovery of certain unconventional superconductors with an anomalous NMR response, mainly, the absence of a modification of the NMR Knight shift at the superconducting transition [41], [42].

Conventional superconductors are well described by the Bardeen-Cooper-Schrieffer (BCS) theory in which, in the presence of the Fermi sea, the Coulomb repulsion between electrons is overcome by the exchange of phonons between electrons of energies ε_k lying in a narrow energy band around to the Fermi energy ε_F. Due to the Pauli exclusion principle, the presence of any attractive interaction between electrons (in three dimensions) renders the Fermi sea unstable towards the formation of two-particle states, or Cooper pairs. In the original BCS theory, these are singlet states with zero total spin, $S = 0$, and orbital part of *s* symmetry (*s-wave* superconductivity). The energy needed to break a Cooper pair is called the superconducting gap Δ. In principle, the gap depends on the wavevector k in reciprocal space, $\Delta = \Delta(k)$, but in the *s-wave* state, Δ is isotropic. The gap is, in fact, a thermodynamic function reflecting the occupation probability of Cooper

pair states. The self-consistency relation for the gap reflects the coherent nature of the superconducting state: a non-zero gap is possible only if sufficiently many Cooper pair states are occupied. The electronic density of states becomes

$$E_k^0 = \sqrt{\xi_k^2 + |\Delta(k)|^2},$$

where $\xi_k = \varepsilon_k - \varepsilon_F$. The gap $\Delta(k)$ in the electronic density of states affects many thermodynamic properties, such as the specific heat, and the Pauli spin susceptibility such as this is measured by the NMR Knight shift. In the BCS *s-wave* theory, the latter is observed to go smoothly to zero as $T \to 0$ [43]-[45].

Different pairing interactions, involving the exchange of bosons other than phonons, may well be responsible for superconductivity in some of the more exotic organic, heavy-fermion, and high-T_c copper oxide superconductors. The superconducting order parameter has an orbital part[1] and a spin part. If the orbital part has odd parity (such as *p-wave*, *f-wave*), the spin part should have even parity (spin-triplet) because of anti-commutation of fermions.

Nuclear Magnetic Resonance (*NMR*) experiments have shown that the Knight shift for $PuCoGa_5$ goes down but does not tend to zero when temperature goes to 0 K [42]. For Sr_2RuO_4, the Knight shift remains constant on passing through the superconducting transition temperature [41]. It is thought that this provides strong evidence for the identification of Sr_2RuO_4 as a spin-triplet superconductor. In spin-singlet superconductors (such as *s-wave* and *d-wave*), the Knight shift decreases below T_c. In contrast, it remains constant in spin-triplet superconductivity (such as *p-wave*, *f-wave*). So if one measures Knight shift, one can distinguish these two types.

However it must be noted that the Knight shift depends on the density of states, which itself is strongly affected by the presence of supercurrent flow. In superconductors with an anisotropic gap, for example, the *d-wave* symmetry of the gap in the $YBa_2Cu_4O_8$ compound to be considered below, the current largely enhances the density of states inside the superconducting gap due to the supercurrent induced Doppler shift. This effect, known as Volovik effect [46], may strongly influence the low temperature Knight shift data. Thus, if conclusions from the *NMR* Knight shift measurements on the pairing mechanism are to be correct, this influence must be properly taken into account in the interpretation of the Knight shift data.

The magneto-optical imaging experiments to be presented below yield the current distribution in a $YBa_2Cu_4O_8$ single crystal (with $T_c = 82$ K) for temperatures varied between 15 and 80 K. With these results, we show that for very low temperatures, the NMR signal comes mainly from the crystal edges where the screening current is flowing. Moreover, the Volovik effect is important and should be considered. For higher temperatures the

[1] The orbital part of the order parameter $\psi(\mathbf{r})$ has the property that $\psi^*(\mathbf{r})\psi(\mathbf{r}) = n_s(\mathbf{r})$, where $n_s(\mathbf{r})$ is the local superconducting electron density.

NMR signal comes from the entire bulk sample and moreover the Volovik effect could be neglected.

4.2 NMR model experiment

4.2.1 Experiment description

In order to model this effect, a model experiment in the NMR configuration was performed on a $YBa_2Cu_4O_8$ single crystal. In the NMR configuration, a time-periodic probing magnetic field H_{rf} is oriented perpendicularly to the static magnetic field H_{dc} used to polarize the nuclear spins. In the case of a superconductor, the *rf* probing field generates large screening supercurrents. The distribution of the *ac* screening current can be visualized using the Differential Magneto-Optical (DMO) technique. In our model experiment, we use the same geometrical arrangement as in a real NMR experiment. However, instead of a *rf* field, we use a very low frequency probing field, $f_{model} \sim 10^{-7} f_{rf}$. This can be justified by the assumption that vortex dynamics in the MHz range is not essentially different from that in the *dc* limit. Since the depinning frequency is several orders higher than that of the *ac* field, it is thus the flux pinning that plays the dominant role in vortex dynamics in both cases [47], [48].

The single crystal used in this experiment is of the $YBa_2Cu_4O_8$ compound, and has $T_c = 82$ K [49]. This has a tetragonal crystalline structure. The crystal is free of impurities and macroscopic defects. It is strip-shaped, of dimensions $1220 \times 328 \times 88\ \mu m^3$ (see Figure 4.1).

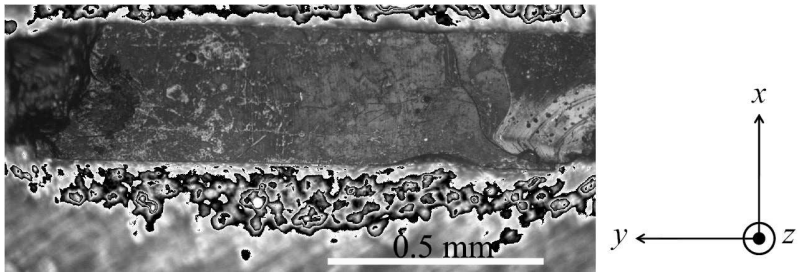

Figure 4.1: Photograph (10 $\times$) of the $YBa_2Cu_4O_8$ single crystal obtained through a polarized light microscope.

We reproduce the field configuration employed in NMR (see Figure 4.2): a dc field of 250 Oe is applied along the z-axis (c-axis of $YBa_2Cu_4O_8$ single crystal) and a periodic transverse field is applied along the x-axis. The periodic field induces a screening current in the superconductor which modifies the local flux density. The z-component of the flux density induced by the presence of this screening current is detected by the Differential

Magneto-Optical (DMO) imaging technique. The screening current due to the ac field has an y-component and a z-component. The screening current flow on the side surfaces is indicated by the narrow arrow and on the top surface, the screening current flows along the y-axis as indicated by $J_y(x,y)$ in Figure 4.2. $J_y(x,y)$ produces a magnetic field in the xOz plane. The z-component of the magnetic field produced by $J_y(x,y)$ can be observed with the DMO imaging technique.

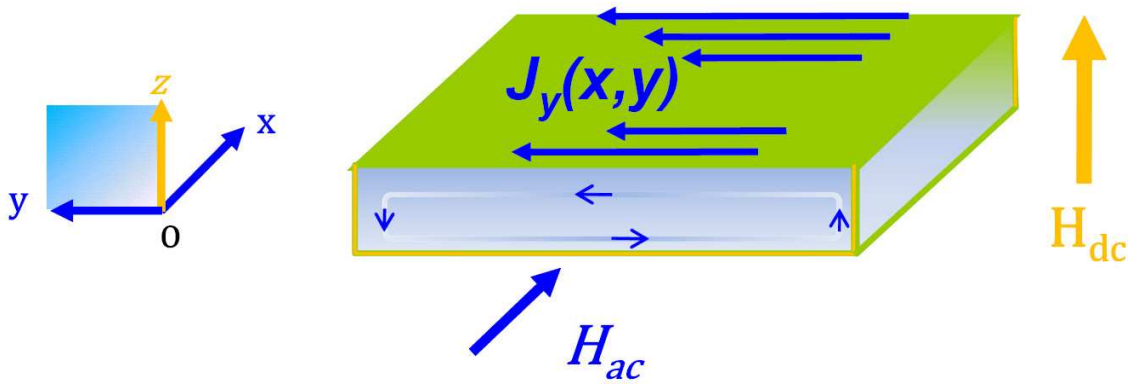

Figure 4.2: Experimental field configuration: dc magnetic field H_{dc} = 250 Oe is applied along z-axis; An ac field H_{ac} is applied along x-axis.

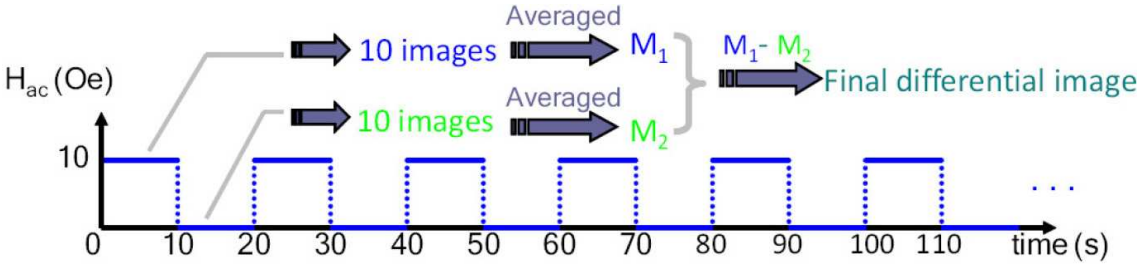

Figure 4.3: Image acquisition procedure for differential magneto-optical imaging with in-plane field modulation.

A transverse field of 10 Oe was applied by a coil with its axis along the x-axis, 10 MO images were acquired and averaged. The transverse field was then removed, another 10 images were collected, averaged and subtracted from the first average. This procedure was repeated 20 times (see Figure 4.3). The self-field due to the screening of a 10 Oe transverse field H_{ac} of frequency 50 mHz can be observed in this manner (see Figure 4.4 (a)).

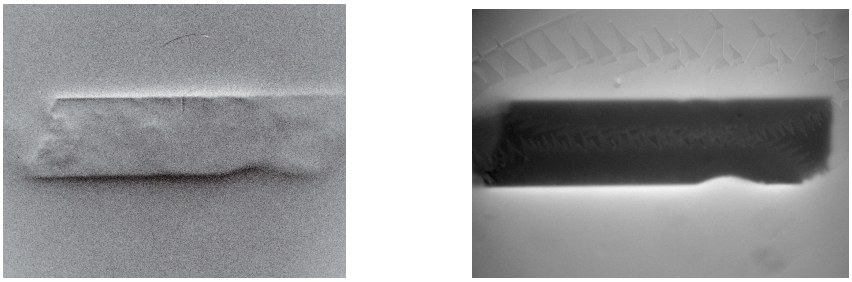

(a) (b)

Figure 4.4: (a) DMO image obtained at T = 45 K with the following parameters: H_z = 250 Oe, H_x = 0, and δH_x = 10 Oe. (b) Direct MO image obtained at T = 27.15 K with the following parameters: H_z = 105 Oe, H_x = 0.

4.2.2 Results: DMO images at varied temperatures

This differential imaging procedure was performed at temperatures varying between 15 K and 80 K with a step up of 5 K. The obtained images are shown in Figure 4.5. Unfortunately, the images obtained at low temperatures below 35 K are strongly perturbed by magnetic domain walls in the indicator (see Figure 4.5 (a-d)).

4.3 Treatment of the obtained DMO images

The sheet current $\mathbf{J}(x,y)$ is defined as $\mathbf{J}(x,y) \equiv \int_0^d \mathbf{J}(x,y,z)$, where $\mathbf{J}(x,y,z)$ is the local current density, d is the thickness of the sample. Since the y-dimension (1220 μm) is considerably larger than the x-dimension (328 μm), one ignores the dependence of the shielding sheet current density on the y-coordinate in order to simplify the treatment that follows. In fact, this approximation was justified through the 2D inversion method [50] to examine the variation of the sheet current density along the y-axis. In the following, the screening current is thus denoted as $J_y(x)$.

Let I denotes the light intensity detected by the camera; H_z denotes the perpendicular magnetic field applied to the sample. As the magneto-optical images were taken in differential mode at $H_z = 250\ Oe$, one needs the value of $\Delta I/\Delta H_z$ at H_z = 250 Oe to convert the gray levels of the differential magneto-optical images into real B_z values. The field was modulated along the z-axis at H_z = 250 Oe. The modulation field varied from -1 Oe to -9 Oe. DMO images were collected at the same condition as those of the experiments performed before (see Figure 4.3) while at a higher temperature T = 85 K. The averaged intensity of the acquired calibration DMO images at T = 85 K as a function of the modulation field was traced in Figure 4.6. The result yields a linear relation with $\delta I/\delta H_z$ = 49.163.

A 16-bit CCD is used for image acquisitions in our set-up. The *zero-value* light inten-

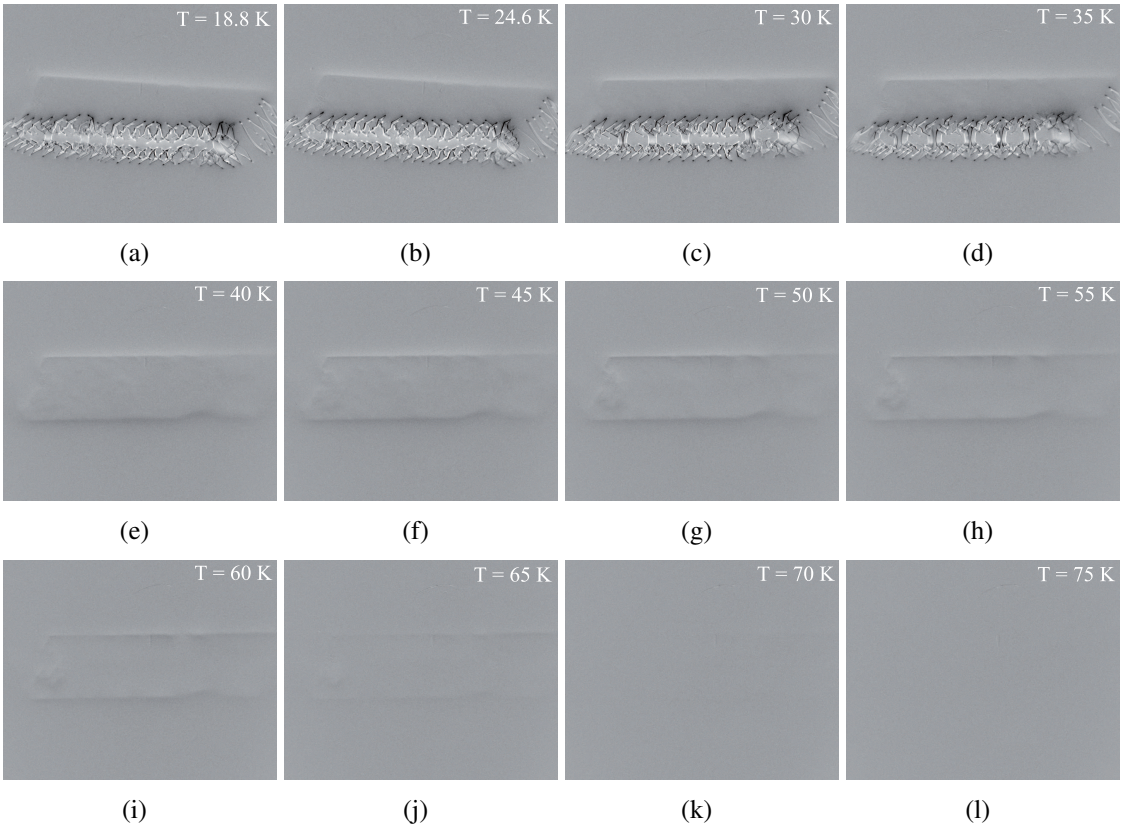

Figure 4.5: *DMO* images obtained at different temperatures with the following parameters: H_z = 250 Oe, H_x = 0, and δH_x = 10 Oe. (a) 18.8 K; (b) 24.6 K; (c) 30 K; (d) 35 K; (e) 40 K; (f) 45 K; (g) 50 K; (h) 55 K; (i) 60 K; (j) 65 K; (k) 70 K; (l) 75 K. An image contrast enhancement was performed to all the obtained raw images with Photoshop. Since the light intensity value of all the pixels lies between 104 and 144, the light intensity value of each pixel is mapped onto the range 0 - 255. This corresponds to a linear relation between the intensities of the raw images and the contrast enhanced images: $y = 6.375(x - 104)$, where x is the intensity value in the raw images and y is the intensity value in the contrast enhanced images.

sity 32809 that we obtained from the calibration is very close to the middle value $2^{16}/2$ = 32768. This is the reason why the opposite signs of the magnetic field can be clearly resolved in DMO images (see Figure 4.7) since the dark and bright regions correspond to the perpendicular fields of opposite directions. Consequently the current direction can thus be revealed in DMO images according to the right hand rule (see Figure 4.7).

A profile of light intensity along a line (see Figure 4.8) across the $YBa_2Cu_4O_8$ strip (x-axis) can be easily obtained from the image. In Figure 4.8, we can see the contour of the sample. The grey levels are converted to colors within the RGB color model in Figure 4.8 by Matlab. The red color and blue color indicate the opposite signs of the magnetic induction B_z at the upper and lower edges. In order to reduce the noise, we average the profiles in a rectangular region where there aren't any curved edges or other defects. The

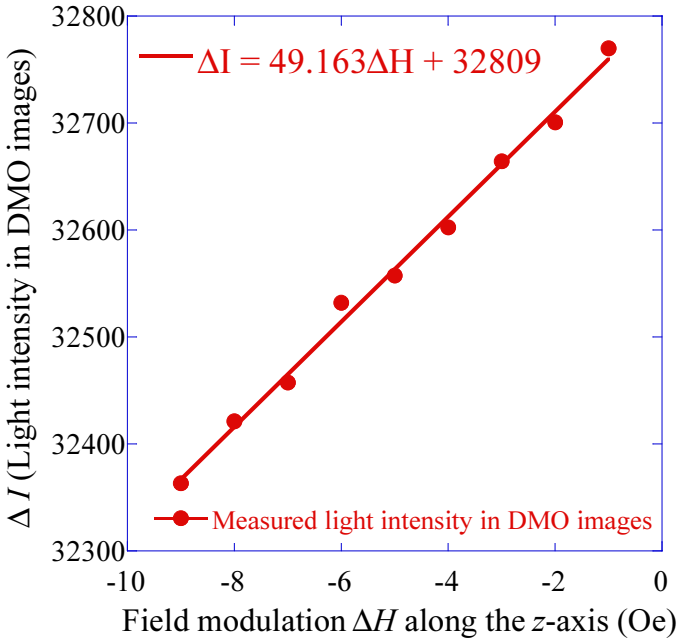

Figure 4.6: Experimental linear relation between ΔI and ΔH for differential MO images at T = 85 K and base field H_z = 250 Oe, with field modulated along the z-axis.

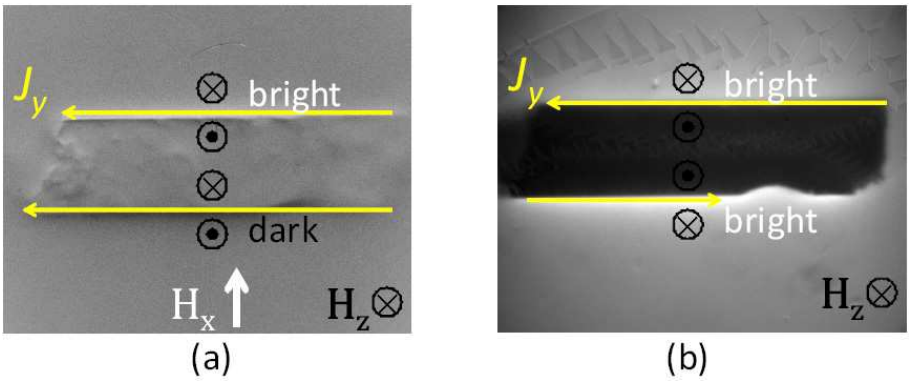

Figure 4.7: Comparison between a DMO image with field modulation along the x-axis (left) and a direct MO image (right). (a) DMO obtained at T = 45 K, H_z = 250 Oe with modulation field along the x-axis (H_x = 0, δH_x = 20 Oe). ΔB_z due to the field modulation along the x-axis can be observed. (b) Direct *MO* image obtained at T = 27.15 K with the following parameters: H_z = 105 Oe, H_x = 0. Screening current due to the static field H_z forming a circle around the sample edges.

light intensity profile along x-axis is shown in Figure 4.9. One can thus convert the grey levels into B_z values with real unit (Figure 4.10 (a)) using the calibration obtained above: $\Delta I/\Delta H_z = 49.163$.

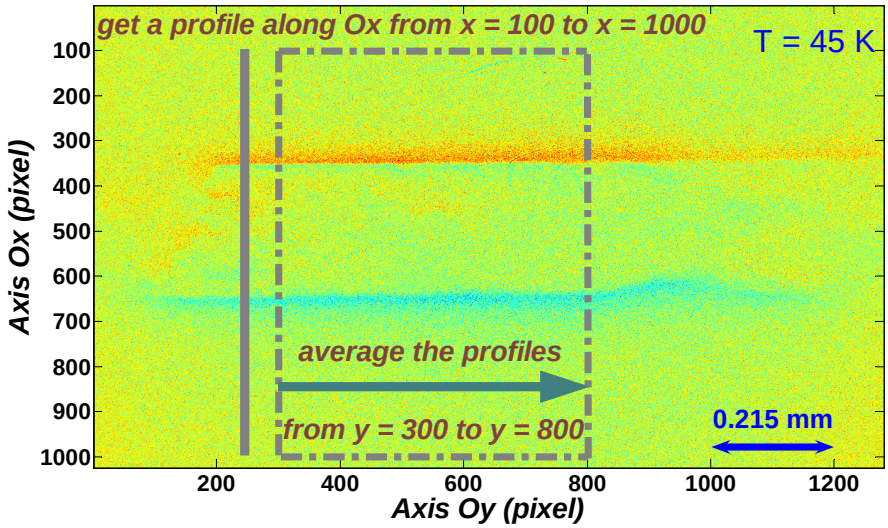

Figure 4.8: Procedure to get the light intensity profile from the magneto-optical image.

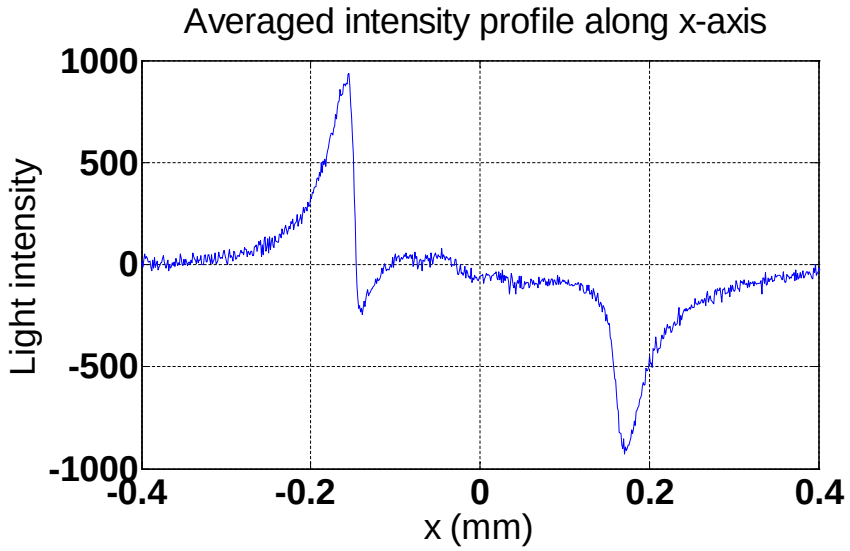

Figure 4.9: Averaged profile of the light intensity from the differential magneto-optical image at T = 45 K and with in-plane modulation of 10 Oe, H_{dc} = 250 Oe. We subtracted 32000 from the absolute value of light intensity in order to set the zero value outside of the sample.

The screening current distribution $J_y(x)$ (Figure 4.10 (b)) is calculated by inversion of the Biot-Savart law using the 1D inversion method provided in the Ref. [51]. The

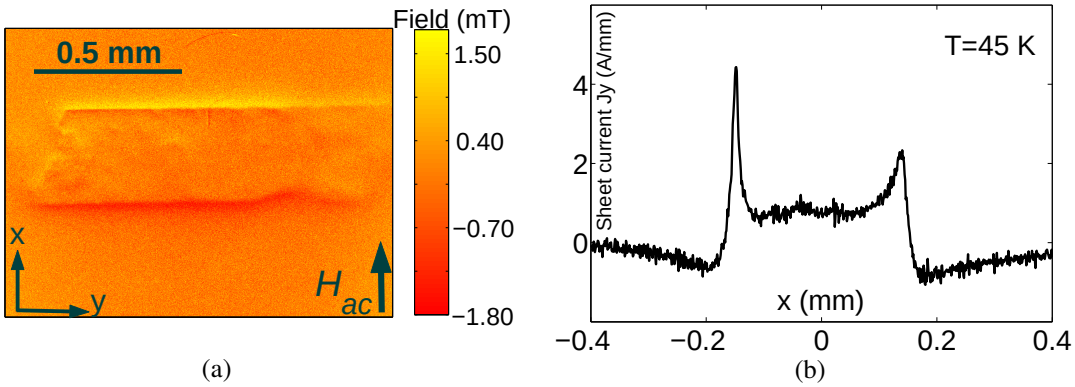

(a) (b)

Figure 4.10: (a) DMO image of the perpendicular component of the induction, induced by $H_{in-plane}$, obtained at T = 45 K with a 10 Oe square wave modulation along the x-axis. (b) Corresponding sheet current $J_y(x)$ (A · mm^{-1}).

distance from the upper surface of the superconductor to the plane of observation, i.e., the indicator's plane, is set as 1 μm in the calculation. As the measured thickness of the crystal is d = 88 μm, the current density at the two edges are respectively 5.04×10^7 (A/m^2) and 2.65×10^7 (A/m^2) for T = 45 K. We have compared this asymmetry with the theoretical calculations provided by G. P. Mikitik et al. in [52]. They have studied the field penetration for a superconducting strip in a magnetic field applied at an angle θ to the normal of their plane. They have found that an asymmetry in flux penetration should occur at the sample edges and this asymmetry is enhanced for large value of tilt angle θ. In our NMR model experiment, $\theta \approx 0.04$ in radian units. Compared with the simulation results in [52], the asymmetry of field penetration at the edges should be less than 10%. While the current density in one edge is almost twice as that of the other edge, we thus attribute the observed asymmetry to the artifact of DMO imaging. Although the signal of the screening current due to the ac field is unambiguously extracted by DMO imaging technique (see Figure 4.4 and 4.7), while due to the quadratic relation between light intensity and magnetic field intensity in a direct MO image, the z-component of the magnetic field generated by the shielding current I_{dc} due to the static field is also present in the DMO images (see the analysis below). The difference of the magnitude decreases when temperature increases (see Figure 4.12 (b)). This can be explained by the analysis presented on Page 48-49 in Chapter 2.

The inversion operation using the Biot-Savart law is performed to I_{diff} (Equation (2.25) in Chapter 2), which is considered to be proportional to B_{ac}, to obtain the current distribution. Examining our situation, $B_{ac} \sim 10$ G, $B_{dc} \sim 250$ G, $\alpha/k \sim 2°/(0.01°/\text{G}) = 200$ G. I_{diff} in the obtained DMO images is thus not only due to B_{ac}, but convoluted with the term $2\alpha/k + B_{ac} + 2B_{dc}$.

At one edge, B_{ac} and B_{dc} are in the same direction; while at the other edge, B_{ac} and B_{dc} are in the opposite direction. The obtained I_{diff} is thus enhanced at one edge and weakened at the other edge compared to the real signal $I_{diff}|_{ac}$.

Nevertheless, the signal of the ac screening current due to the ac magnetic field is unambiguously extracted by DMO imaging technique (see Figure 4.4 and 4.7). Equation (2.25) in Chapter 2 shows that the sign of I_{diff} is determined by the sign of B_{ac} (the sign of $2\alpha/k + B_{ac} + 2B_{dc}$ is fixed since $|B_{ac}| \ll |2\alpha/k + 2B_{dc}|$). Figure 4.7 illustrates this point unambiguously. At high temperatures, B_{ac} and B_{dc} distribute uniformly across the whole sample, Equation (2.26) in Chapter 2 reduces to $I_{diff} \sim I_{diff}|_{ac}$. This can explain the much weakened asymmetry of the current densities at the edges shown in Figure 4.12 (b) at high temperatures.

In the case that the sample itself presents some inhomogeneities at the two edges (different properties between the two edges, e.g., smoothness, purity, sectional geometry, etc.), this factor needs to be taken into consideration if one conducts a rigorous analysis of this asymmetry. But even in this case, the above argument is still valid to explain the large difference of the magnitudes of current densities extracted from DMO images at the edges. We mention that D. G. Gheorghe et al. [53] have studied flux penetration into superconducting Nb_3Sn in oblique magnetic fields by magneto-optical imaging (*direct imaging mode*) and they have found an agreement between their experimental results and the theoretical calculations in [52].

4.4 Screening current distribution and transverse field reconstruction

The profiles of the perpendicular magnetic flux density B_z and the current distribution J_y for T = 40 K to T = 70 K obtained in this manner are presented in Figure 4.11 and Figure 4.12 respectively[2]. Figure 4.12 shows that the current concentration at the edges become more and more important when temperature increases from T = 40 K and reaches its maximum concentration at T = 55 K (i.e., the sheet current J_y is nearly zero in the middle of the sample). When the temperature continues to increase (for example, T = 60 K and T = 65 K), this concentration becomes less important; The current distribution at T = 70 K is nearly uniform across the sample as in a metallic conductor. At low temperatures, material disorder pins the vortices and prevents their motion, resulting in a finite critical current. In this case the transport current is expected to flow in a way similar to the case of the Meissner state where $B_{ac}(x)$ is expelled from the sample. The measured perpendicular flux density B_z profile at T = 18.8 K is shown in Figure 4.13 (a). Without the disturbance of the magnetic domain walls in the indicator, we would have a B_z profile with two peaks at the edges (in unit of mm: x_1 = -0.164, x_2 = 0.164).

[2] The units in the Figure 4.11, 4.12 and 4.13 are not real physical units for B_z and J_y.

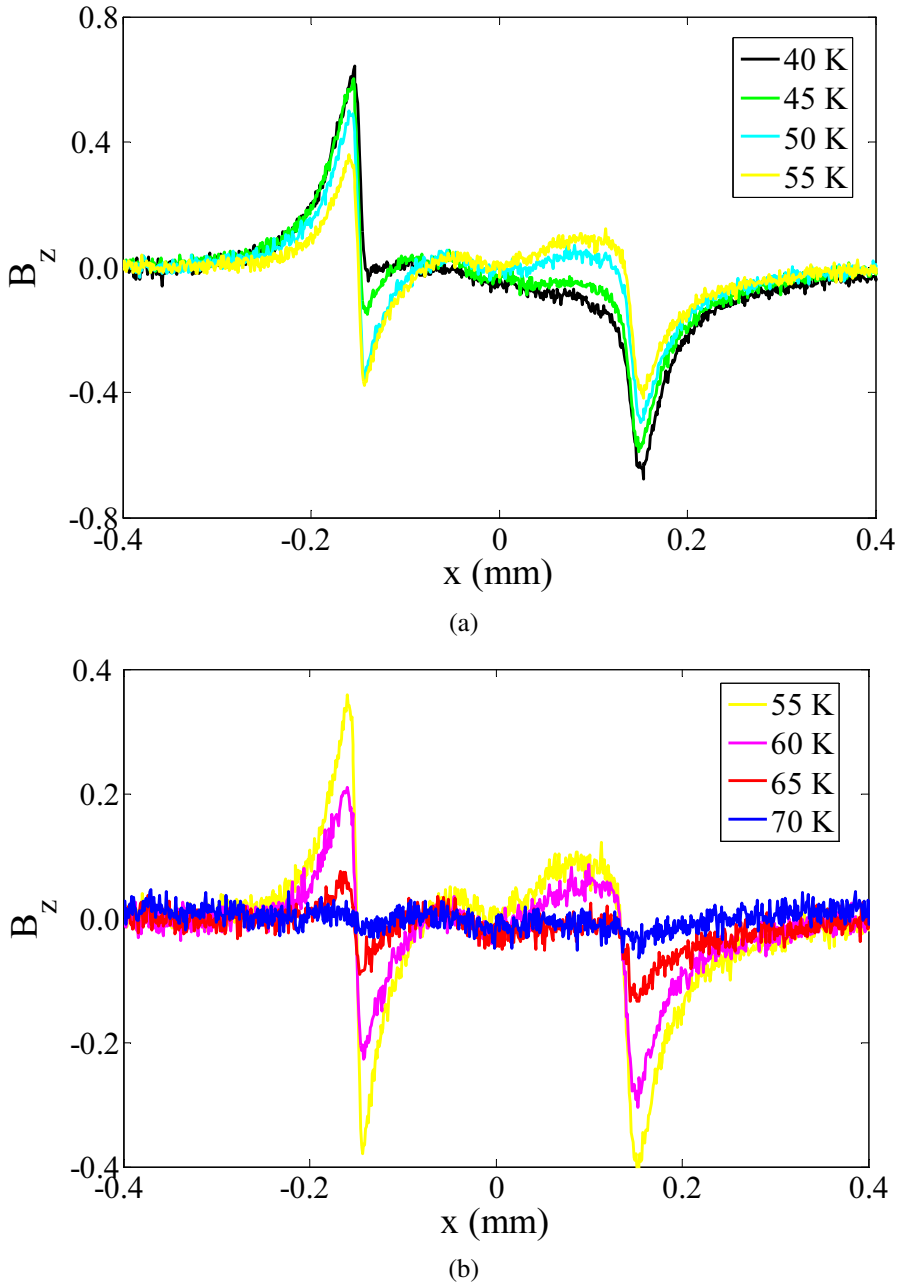

Figure 4.11: Perpendicular flux density B_z profiles extracted from DMO images presented in Figure 4.5: (a) 40 K - black, 45 K - green, 50 K - cyan, 55 K - yellow; (b) 55 K - yellow, 60 K - magenta, 65 K - red, 70 K - blue.

Three regimes for the current flow are clearly manifest: At T > 70 K, current flow is uniform; At T < 20 K, one has the critical state due to bulk flux pinning. The current flows in the regions penetrated by the *ac* field only; At intermediate temperatures 20 K < T <

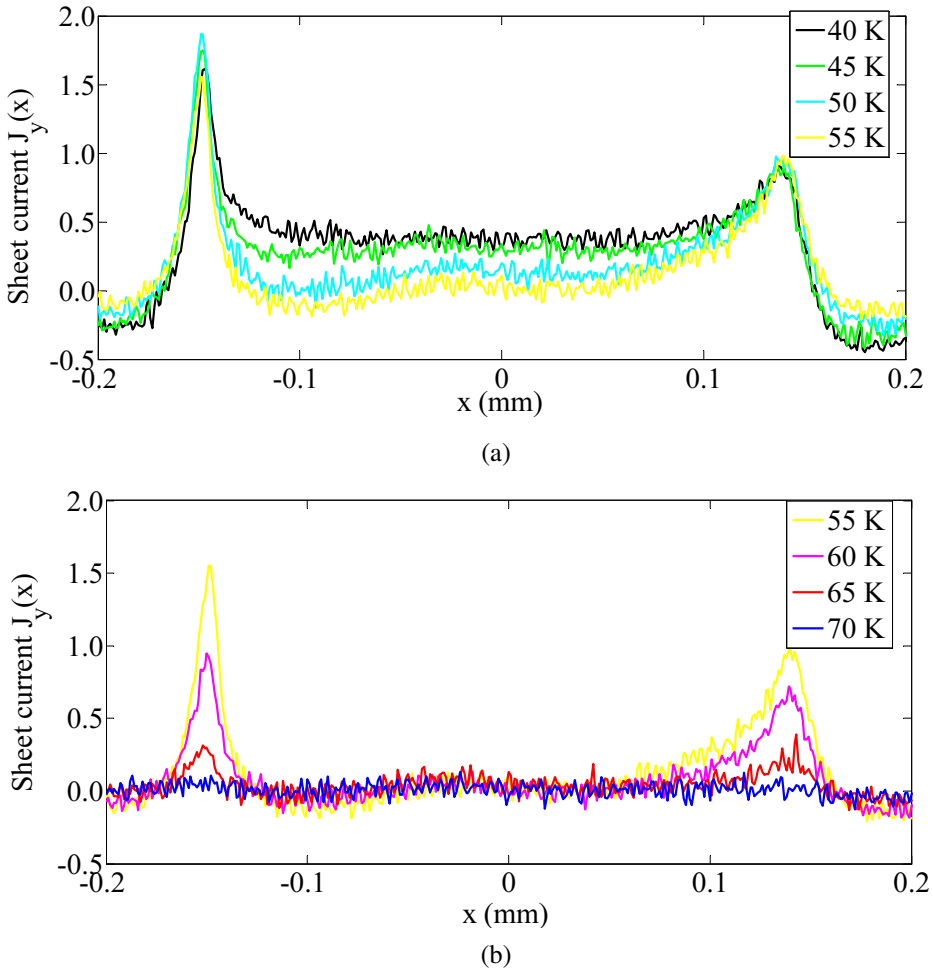

Figure 4.12: The sheet current distribution obtained by the 1D inversion method of the Ref. [51] with h = 1 μm (h is the distance from the upper surface of the superconductor to the plane of observation) to the B_z data of Figure 4.11. (a) 40 K - black, 45 K - green, 50 K - cyan, 55 K - yellow; (b) 55 K - yellow, 60 K - magenta, 65 K - red, 70 K - blue.

70 K, current flows only at the sample edges due to the surface barrier effects (see Figure 4.12) [54].

From the current distribution, one can reconstruct the magnitude of the transverse field H_x modulation normalized to H_{ac} (see Figure 4.14). This corresponds to the *local* probing field in NMR. For T > 20 K, the transverse field is almost homogenous, the whole sample contributes to the NMR signal. For T < 20 K, only a thin surface layer is probed by the NMR measurements.

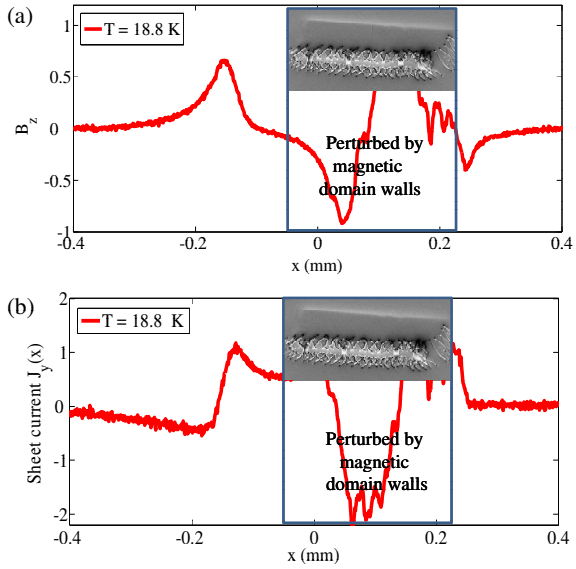

Figure 4.13: (a) Perpendicular flux density B_z profile at T = 18.8 K obtained from Figure 4.5 (a). (b) The sheet current distribution obtained by the 1D inversion method applied to the B_z data shown in Figure (a). The region enclosed in the rectangle is perturbed by magnetic domain walls in the MO indicator (garnet film).

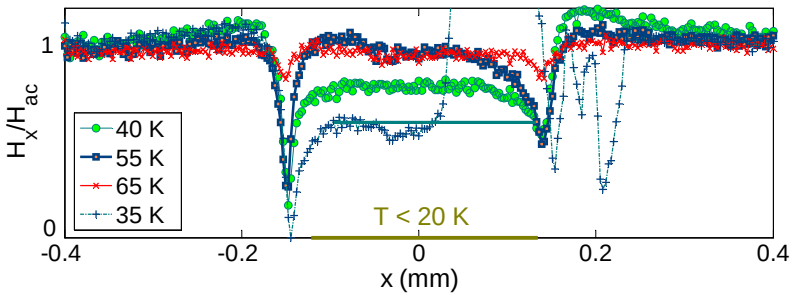

Figure 4.14: Magnitude of the transverse field H_x modulation normalized to H_{ac}: asterisk 65 K, square 55 K, circle 40 K, plus sign 35 K. The anomaly of the data at T = 35 K is due to the strong perturbation by magnetic domain walls in the indicator.

4.5 Effects of the screening current on NMR Knight shift data

As a first example, let us consider the investigated crystal at T = 45 K; the sheet current J_d (integrated over the sample thickness d = 88 μm) at the edges is then 4.5×10^3 Am^{-1}. The maximum current density $j = 5 \times 10^7$ Am^{-2}. At T < 20 K, the current density reaches 10^8 Am^{-2}, which results in $v_s \approx 5$ ms^{-1}, to be compared to $v_F \approx 1.2 \times 10^5$ ms^{-1} [55], $T_F \approx 4000$ K, i.e., a Doppler shift of 0.15%. Let us now estimate the Volovik effect [46]: $N(0,H)/N_0 = \langle \mathbf{p}_F \cdot \mathbf{v}_s \rangle / \Delta_0 \approx K\sqrt{H/H_{c2}}$. Using $K \approx 1$, $H_{c2} = 100$ T, and $H = 1$ T (NMR experimental condition), this yields $N(0,H)/N_0 = 10$ %. The effect due to the screening current due to H_{ac} can thus be ignored for our $YBa_2Cu_4O_8$ crystal. But for other high-T_c superconductors, e.g., $Bi_2Sr_2CaCu_2O_8$, in which screening currents of the order of 10^{10} Am^{-2} are attained, the Doppler shift due to screening current may strongly influence the NMR Knight shift data below 20 K.

For a *d-wave* superconductor like $YBa_2Cu_4O_8$, a linear dependence of the Knight shift on temperature should be observed for $0.1T_c < T < 0.4T_c$. While the Volovik contribution may lead to a non-vanishing Knight shift for $T \rightarrow 0$, the Doppler shift due to the screening current may lead to a *nonlinear* dependence of the Knight shift on temperature which would be determined by the temperature dependance of the critical current.

4.6 Summary and conclusions

The above experiments show that the penetration of a time-periodic magnetic field, perpendicular to a static magnetic field, into a superconductor is counteracted by vortex pinning at low temperatures. At high temperature regime, near to T_c, another problem arises since the $H_{c_2}(T)$ is small at this temperature regime and the static field applied in NMR measurements might be very close to the value of $H_{c_2}(T)$ and the decrease of the Knight shift below T_c may be delayed. This point of view is held by Y. Matsuda, Professor of the Department of Physics, Kyoto University, Japan [56]. The debate on the *p-wave* nature of the pairing symmetry in Sr_2RuO_4 continues until today [57]. More recent NMR data performed on Sr_2RuO_4 provided less clear evidence [57] for the *p-wave* nature of Sr_2RuO_4 than the data obtained by K. Ishida et al [41] in 1998.

The dependence of the in-plane field penetration on temperature obtained from the magneto-optical experiments is general for all type-II superconductors. When one performs NMR Knight shift measurements to determinate the pairing symmetry in high temperature superconductors, the following issues should be carefully considered: (1) At low temperatures, only the edges are probed by the NMR measurements and moreover, the contribution of Doppler shifted quasi-particles (Volovik effect) to the Knight shift should be considered properly; (2) At higher temperatures, the NMR measurements probe the entire sample but one should assure that the static field is well below $H_{c_2}(T)$.

The NMR Knight shift measurement is one way to probe the density of states. There is another type of measurement which permits one to distinguish the pairing symmetry in superconductors, the phase-sensitive measurements. For example, C. C. Tsuei et al. [58] have shown the *d-wave* pairing symmetry in $YBa_2Cu_3O_{7-\delta}$ in a convincing way with a tricrystal superconducting ring of $YBa_2Cu_3O_{7-\delta}$.

Chapter 5

Shear viscosity of the vortex liquid measurements in optimally doped $Bi_2Sr_2CaCu_2O_8$ in channel confined geometry

5.1 Introduction

The most important feature of the phase diagram of vortex matter in high-T_c superconducting single crystals is the first order phase transition - the vortex lattice melting transition [24], [25], [59] - [62], from a vortex lattice to a vortex liquid. The vortex lattice phase is the ordered phase, most often, a triangular lattice. This lattice structure has been observed in $Bi_2Sr_2CaCu_2O_8$ by Bitter decoration [63] and neutron diffraction [64] techniques. The vortex liquid phase is the disordered phase and no signal could be obtained from the vortex ensemble using structural probes like Bitter decoration or neutron diffraction techniques.

This first order vortex lattice melting transition has been demonstrated in $Bi_2Sr_2CaCu_2O_{8+\delta}$ by H. Pastoriza et al. [61] and by E. Zeldov et al. [24]. Both authors showed that the vortex lattice melting is accompanied by a discontinuous jump of the vortex density n_v, which could be measured by the local magnetic induction B since $B = n_v\phi_0$. It was also shown that the vortex liquid phase is denser than the vortex lattice phase. Similar magnetic measurements performed by U. Welp et al. [62] on $YBa_2Cu_3O_{7-\delta}$ single crystals have confirmed this vortex density jump in that material. Further more, the latent heat associated with the vortex lattice melting transition was measured in $YBa_2Cu_3O_{7-\delta}$ single crystals by A. Schilling et al. [25] and by M. Roulin et al. [65].

Aside from the above thermodynamic signatures, this phase transition also manifests itself in transport measurements. Indeed, the first indications of vortex lattice melting were obtained from dynamic measurements. A discontinuous drop of the resistance was

observed at the vortex liquid to lattice phase transition in $YBa_2Cu_3O_7$ single crystals by H. Safar et al. [59] and by W. K. Kwok et al. [60] and later in $Bi_2Sr_2CaCu_2O_8$ single crystals by D. T. Fuchs et al. [66]. This resistance jump is related with the disappearance of the critical current [67]. The resistivity is not a thermodynamic property as the equilibrium of the vortex ensemble is disturbed by the transport current. Resistivity measurements probe the motion of vortices and can thus show the signature of phase transitions of the vortex system, because the dynamic properties may change dramatically between different phases. The definition of the resistance is given by Ohm's formula: $R = V/I$. If the resistance is current-independent, we call it a *linear resistance*.

The vortex liquid shows a linear resistance behavior, meaning that the vortex motion is diffusive. In the regime above the melting line, vortex motion is thermally activated, and the resistivity was described by an Arrhenius law, $\rho = \rho_0 exp(-U_0/T)$ [68], [69]. The activation energy U_0 depends on magnetic field and field orientation. This linear resistance behavior implies the absence of superconducting phase coherence at long distance. Related is the sudden decrease of the coherence between superconducting layers (c-axis correlation) observed by S. Colson et al. [70] by using the Josephson plasma resonance technique at the melting transition in $Bi_2Sr_2CaCu_2O_{8+\delta}$ single crystals.

The onset of the nonlinearity of the dynamic response shows that a non-zero critical current density exists in the low temperature vortex solid phase due to the pinning by the crystalline defects, i.e., the so-called *bulk pinning*, or alternatively, by the vortex interaction with the sample boundaries, the so-called *surface pinning*. The onset of a non-zero critical current density defines the so-called *irreversibility line* on a *H-T* phase diagram. In clean superconducting single crystals, the vortex lattice melting line coincides very often with the irreversibility line. But they are of different natures: the irreversibility line is a dynamic property while the vortex lattice melting line is intrinsically thermodynamic. Indeed, D. Majer et al. showed a distinction between the irreversibility line and the melting line [71]. Whether the irreversibility line in disordered systems is related to melting in pure systems depends on the degree and type of disorder in a specific sample.

The origin of the sudden depinning of the vortex lattice at the melting transition is not clear. Since neither the bulk pinning nor the surface pinning disappears at the melting transition, the change of the vortex system's elastic properties at melting must be responsible. It was conjectured that the vortex solid has a non-zero shear modulus while the liquid state has vanishing shear modulus [72]. It is argued that the proliferation of the vortex lattice dislocations upon melting [73] or the vanishing of flux cutting barriers upon melting [74] may be the reason of the vanishing of the shear modulus at the melting transition.

In two-dimensional superconducting thin films, the proliferation of vortex lattice dislocations has been recognized as the melting mechanism [75]. The experimentally measured vortex liquid shear viscosity in two-dimensional $\alpha - Nb_3Ge$ films was found to be in good agreement with the theory of two-dimensional melting [76]. In three-dimensional superconductors, whether melting of the vortex lattice is also mediated by the spontaneous

generation of dislocation loops in the vortex lattice or by other mechanisms, for example, flux line cutting, remains unanswered yet.

In real high-T_c superconductors, the underlying melting always take place in the presence of disorder, such as oxygen vacancies or twin boundaries. The transport measurements are thus influenced by the presence of this disorder. There are two types of disorder which affect vortex motion: *point-like microscopic disorder*, for example, oxygen vacancies, and *correlated disorder*, for example, twin boundaries or columnar defects. In order to study their influence on vortex matter, experiments involving irradiation of superconductors by high energy electrons [77] or heavy ions [78], [79] have been carried out. These techniques permit the introduction of disorder in superconductors in a controlled way [22], [80] - [87].

5.1.1 Point-like microscopic disorder

Irradiation with high energy electrons introduces point-like microscopic disorder into the superconducting single crystals, in the guise of vacancy-interstitial pairs (Frenkel pairs) [77], [88]. It has been studied theoretically [89] and demonstrated experimentally [90], [80] that sufficiently weakly pinning point-like defects do not change the nature of the melting transition and the melting line in the *H-T* phase diagram may be only slightly lowered when the amount of point disorder increases.

J. A. Fendrich et al. [81] found that point-like disorder introduced by high energy electron irradiation (1 MeV) with a fluence of 1×10^{19} electrons/cm^2 in an untwinned $YBa_2Cu_3O_{7-\delta}$ single crystal lead to an apparent disappearance of the vortex melting transition, accompanied by a much more gradual decrease of the resistivity. However, M. Konczykowski et al. [82] showed that in $Bi_2Sr_2CaCu_2O_8$, the vortex melting transition seems to be robust to the introduction of point-like disorder by high energy electron irradiation (2.3 MeV) up to a fluence of 1.7×10^{20} electrons/cm^2. This was demonstrated by the vortex density jump through micro-Hall probe measurements [82]. Both of the irradiation experiments were performed at low temperatures, 40 K in [81] for $YBa_2Cu_3O_{7-\delta}$ single crystal and 20 K in [80], [82], [88] for $Bi_2Sr_2CaCu_2O_8$ single crystals; different melting mechanisms in *YBCO* and *BSCCO* may be the origin for these different conclusions.

5.1.2 Correlated disorder

Irradiation with high energy heavy ions introduces amorphous columnar defects into high-T_c superconducting single crystals. For example, in $Bi_2Sr_2CaCu_2O_8$, the latent columnar tracks have a diameter of about 7 *nm* when the crystal is bombarded with a 1 GeV Pb^{56+} beam [91] - [93], [79]. Columnar tracks provide a pinning energy much stronger than those provided by oxygen vacancies or other point defects; Hence, vortices are preferentially localized on the amorphous tracks in the vortex solid as well as in the vortex liquid [94], [95].

The matching field B_ϕ is defined as $B_\phi \equiv n_d \phi_0$, where n_d is the number of columnar defects per unit area, ϕ_0 is the magnetic flux quantum, $\phi_0 = h/2e$. A small density n_d of columnar defects, i.e., $n_d < n_V \equiv \frac{B}{\phi_0}$, is susceptible to produce a *porous* vortex matter, in which vortices not localized on a track are surrounded by a matrix of vortices pinned by the columnar defects [83] (see Figure 5.1 (b)). The vortices form a polycrystalline structure in this case. The grain size and the boundaries are determined by the spatial distribution of columnar defects, which could be modeled by Poisson statistics.

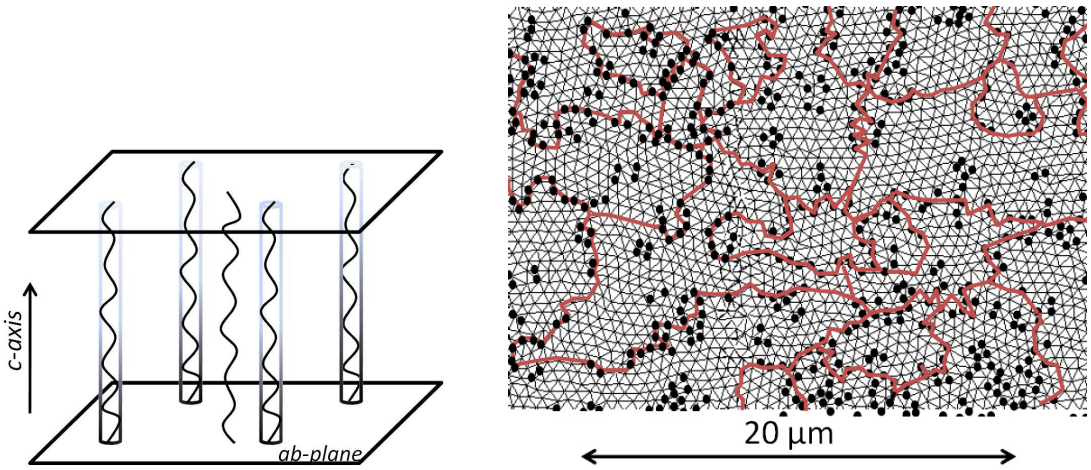

(a) (b)

Figure 5.1: (a) Illustration of pinned vortices localized on the columnar defects and the unpinned vortices outside of the columnar defects. The magnetic field is along the columnar defect, which is also parallel to the c-axis of the *BSCCO* crystal. (b) Magnetic decoration with columnar defects. The matching field is B_ϕ = 10 G and the applied field is 8 times of the matching field: B = 80 G. The vortex density is thus 8 times of the density of columnar defects. The vortices localized on the columnar defects are strongly pinned and form a rigid matrix. In contrast the vortices that reside in the pores are weakly pinned and they are surrounded by a rigid matrix. Figure from Ref. [83].

S. S. Banerjee et al. [84] have argued that because of the rigid matrix defined by the columnar defects, a two-step transition takes place upon freezing: (1) a normal liquid vortex state to a so-called nano-liquid vortex state due to the freezing at the pinned matrix; (2) freezing of the interstitial crystallites, i.e., the freezing of the so-called nano-liquid vortex state to the ordered vortex crystallites [84].

An increase of the columnar defect density leads to the complete amorphization of the vortex ensemble, which now forms a so-called *Bose-glass* vortex state [96], [97]. It is generally believed that the first order melting transition is suppressed with an increasing density of columnar defects [96], [97]. Nevertheless, experiments probing the vortex force-velocity curve [98] as well as Josephson Plasma Resonance measurements on heavily irradiated underdoped $Bi_2Sr_2CaCu_2O_{8+\delta}$ [70] suggest that the first order transition in this material is robust up to latent track densities of at least 1×10^{11} cm^{-2}.

Experiments performed at relatively high irradiation fluences showed that in contrast, the irreversibility lines were pushed up to considerably higher fields, and that the newly irreversible region of the *H-T* phase diagram shows the characteristics of a Bose-glass phase [85], [86], [87], [22].

Upon increasing the columnar defect density, the irreversibility field in $Bi_2Sr_2CaCu_2O_8$ saturates to a defect-independent value B_{irr}^{max}, that is phenomenologically well described by the expression:

$$B_{irr}^{max} = B_\Lambda \frac{\varepsilon_0 s}{k_B T} exp(\frac{\varepsilon_0 s}{k_B T}) \tag{5.1}$$

where $B_\Lambda = \phi_0[\lambda_{ab}^{-2} + \gamma^{-2}s^{-2}]^{-1}$, λ_{ab} is the in-plane penetration length, γ is the anisotropy factor, s is the distance between the adjacent CuO_2 bi-layers ($s \approx 1.5\ nm$), and $\varepsilon_0 = \phi_0/4\pi\mu_0\lambda_{ab}^2$. This upper limit represents a "*delocalization line*" above which two-dimensional pancake vortices can diffuse from their equilibrium site in the vortex solid and the "*line-like*" character of vortices is lost [22]. Equation (5.1) is inspired from a two-dimensional dislocation-unbinding model in a "*discrete superconductor*" defined by the allowed vortex positions (localized at the columnar defects) and is valid for $B < \frac{1}{6}B_\phi < B_{cr}$. The two-dimensional to three dimensional crossover field $B_{cr} = \phi_0/\gamma^2 s^2$ separates a two-dimensional flux fluctuations part (high field) and a three-dimensional flux fluctuations part (low field) [99].

For a small dose of heavy ions, one remarks that the delocalization line of the rigidly pinned matrix (of vortices localized on columns, and surrounding the puddles of vortex nano-liquid) introduced by S.S. Banerjee et al. [84] corresponds to a rapid drop of the resistivity. Its position coincides with the saturation position of the irreversibility line at high columnar defect density given by Equation (5.1). It is therefore legitimate to ask whether the mobility of vortex lattice dislocations is responsible for these results.

5.1.3 Major controversial issues in vortex dynamics in high-T_c superconductors

To summarize, several questions remain unanswered concerning the vortex dynamics in high-T_c superconductors, and notably in $Bi_2Sr_2CaCu_2O_8$.

1. The resistance jump at the vortex lattice melting transition in two-dimensional superconducting films has been well understood through the vortex lattice dislocation unbinding mechanism [75], [76]. The shear viscosity of the vortex ensemble is inversely proportional to the density of free vortex lattice dislocations. Near to the vortex lattice melting transition, the shear viscosity diverges due to the binding of free dislocations into pairs. Since the resistance is determined by the shear viscosity of the vortex ensemble, the mechanism of resistance jump associated with the vortex lattice melting transition in two-dimensional superconducting films can thus

be clearly explained. In three-dimensional superconductors, the mechanism related to the resistance jump at the melting transition remains unknown.

2. Besides the vortex lattice phase, various other vortex phases were proposed to describe the behavior of vortices in high-T_c superconductors. They are named the Bragg glass, the vortex glass and the Bose glass. A Bragg glass phase may be realized in a vortex system where only weakly pinning point-like defects are present [89], [90], [100], [101]. In this phase, the dependence of the bundle activation barrier U due to collective pinning, on current density j, is shown to be of power-law type: $U(j) \sim j^{-\alpha}$ [102]. The vortex glass, realized for strongly pinning point-like disorder [103], is an analogy to the spin glass. The E-j characteristic for the vortex glass is thought to be $E \sim exp((-\frac{j_0}{j})^{\alpha})$, derived from a droplet model. The Bose glass phase [96] in the presence of correlated disorder is the best understood glassy phase for the vortex system. In the region $B \ll B_\phi$, all the flux lines are localized on a columnar defect; In the region $B \geq B_\phi$, the situation is more complicated since there is a co-existence of pinned vortices situated on the columnar defects, and unpinned vortices outside of the columnar defects. A picture of polycrystallites was proposed in [83] and used in [84] to investigate the vortex transport properties in this situation.

   It is believed that vortex motion is determined by collective jumps of correlated regions of the lattice in the Bragg glass phase [104], [105], [101], [90]. In the vortex glass phase, the average vortex velocity is limited either by the activation rate of individual lines from the strongly pinning defects, or more likely, by the poorly understood motion of vortex lattice dislocations (plastic creep) [106], [107]. In the Bose glass phase, vortex motion for $B \ll B_\phi$ is understood to take place via the half-loop, or double kink nucleation process [96], [97], [85], [86] or via vortex variable range hopping [96], [97]. For the situation when $B \geq B_\phi$, the vortex lattice dislocations are considered to play an important role in the vortex motion.

   Since the vortex lattice dislocations substantially modify the shear modulus of the vortex ensemble [108], it seems important to measure this quantity.

3. Whether the delocalization line described in [84] is related with the irreversibility line in [22] has not yet been confirmed. Since the model [22] is inspired on two-dimensional physics, a measurement of the shear modulus or shear viscosity should provide valuable information to enrich our understanding of the topics listed above.

5.1.4 Relation between resistivity and shear viscosity in a channel confined geometry

The shear properties of the vortex system can be probed in a channel confined geometry proposed by M. C. Marchetti and D. R. Nelson [109] through resistivity measurements

near to the vortex liquid-solid transition. Experiments of this kind have been performed in two-dimensional superconducting films [110], [76].

In the vortex liquid state, vortices are believed to be free to move past one another and a hydrodynamic description should be used to study the vortex velocity distribution [109]. Consider the flow of an isotropic flux fluid in a channel contained between two flat strongly pinning boundaries in the yz-plane at $x = -L/2$ and $x = L/2$, shown in Figure 5.2.

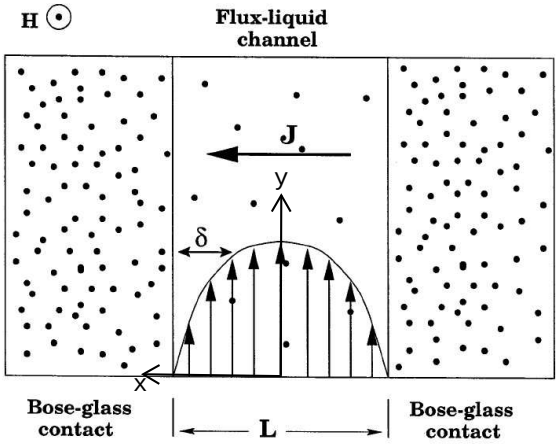

Figure 5.2: A weakly irradiated channel of size L where the flux liquid is sandwiched between two heavily irradiated Bose-glass contacts. A current J applied across the channel yields flux motion along the channel. (Figure from Ref. [32])

The magnetic field is in the z direction. The transport current is applied along $\hat{\mathbf{x}}$, $\mathbf{J} = J\hat{\mathbf{x}}$, and yields a constant driving Lorenz force:

$$\mathbf{f} = n_v \phi_0 \hat{\mathbf{z}} \times \mathbf{J} \tag{5.2}$$

in the y direction, where n_v is the areal vortex density. The equation to describe the velocity distribution of the vortex liquid is:

$$-\gamma \mathbf{v} + \eta \bigtriangledown_{\perp}^2 \mathbf{v} + \mathbf{f} = 0. \tag{5.3}$$

Equation (5.3) is a hydrodynamic description of flux flow which is valid on scales large compared to the intervortex spacing.

Here $\mathbf{v}$ is the vortex velocity, γ is the vortex "friction" coefficient of Bardeen and Stephen, augmented by the effects of weak microscopic disorder such as oxygen vacancies [111]. The parameter η is the vortex shear viscosity.

Once the vortex velocity distribution is obtained, the electric field profile can be found immediately from: $\mathbf{E}(\mathbf{r}) = \mathbf{B} \times \mathbf{v}(\mathbf{r})$. Equation (5.3) can then be rewritten as an equation

for the local electric field **E**:

$$-\delta^2\nabla_\perp^2\mathbf{E}+\mathbf{E}=\rho_f\mathbf{J}, \tag{5.4}$$

where the viscous length $\delta\equiv\sqrt{\eta/\gamma}$ characterizes the importance of viscous drag. When the first term $-\delta^2\nabla_\perp^2\mathbf{E}$ in Equation (5.4) is absent, i.e., the flux liquid viscosity is sufficiently small, Equation (5.4) reduces to Ohm's law with the flux-flow resistivity given by the bulk value, ρ_f.

In the following, we assume $\mathbf{v}=0$ at the strongly pinning walls. The solution of Equation (5.3) is then:

$$v_y(x)=v_\infty(1-\frac{cosh(x/\delta)}{cosh[L/(2\delta)]}). \tag{5.5}$$

Here the $v_\infty=\mathbf{f}/\gamma$ is the usual Bardeen-Stephen limiting flux-line velocity in the absence of any strong pinning centers. If one takes into account the velocity distribution given by Equation (5.5) to compute the resistivity, one finds:

$$\rho=\rho_f[1-\frac{2\delta}{L}tanh(\frac{L}{2\delta})], \tag{5.6}$$

where $\rho_f=(n_v\phi_0)^2/\gamma=B^2/\gamma$ is the limiting Bardeen-Stephen flux-flow resistivity for a sample without columnar defects.

Sufficiently close to the vortex liquid-solid phase transition, one has $\delta(T)>>L$, and therefore one has: $tanh\ (\frac{L}{2\delta})\sim\frac{L}{2\delta}$ - $\frac{1}{3}(\frac{L}{2\delta})^3$. We then have:

$$\rho(T)\approx\frac{1}{12}(n_v\phi_0)^2\frac{L^2}{\eta(T)}\sim B^2\frac{L^2}{\eta(T)}, \tag{5.7}$$

so that the resistivity $\rho(T)$ is inversely proportional to the vortex shear viscosity $\eta(T)$ of the liquid vortex system and proportional to the square of the channel width.

The above geometry has been used extensively for the study of the mechanism of vortex lattice melting in two-dimensional superconducting films [76], [112]. This melting is thought to occur via successive vortex lattice dislocation and disclination unbinding and is a continuous transition. This mechanism was first proposed by D. R. Nelson and B. I. Halperin [75] and A. P. Young [113] in 1979 and involves two transitions of the Kosterlitz-Thouless kind [114].

In the low temperature phase, vortex dislocation pairs are bound together (see Figure 5.3 (b)), the vortex lattice possesses a quasi-long-range positional order and a long-range orientational order; When the temperature is increased, the quasi-long-range positional order is lost, at melting, due to the spontaneous separation of paired dislocations. Nevertheless, long-range orientational order persists (see Figure 5.3 (c)). At melting, one thus enters, in theory, an intermediate phase, the so-called *hexatic* liquid, characterized by two order parameters: a short-range positional order and a quasi-long-range orientational (sixfold) order. When the temperature continues to increase, the quasi-long-range

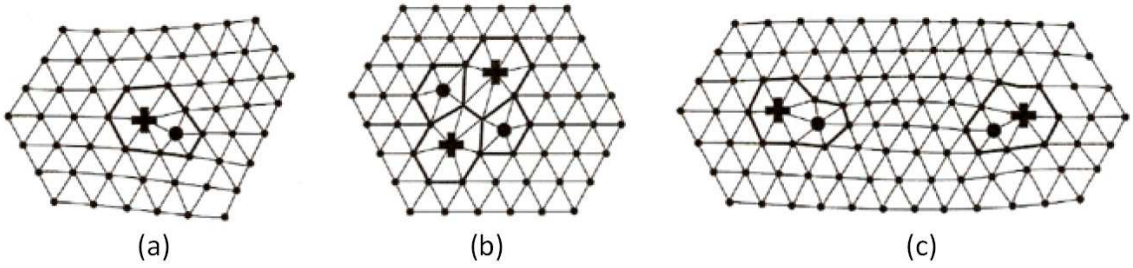

Figure 5.3: Two-dimensional melting through the separation of dislocation pairs: (a) A dislocation. (b) Paired dislocations of opposite effects. (c) Separation of paired dislocations.

orientational (sixfold) order is destroyed due to disclination unbinding. This transforms the *hexatic* liquid into an isotropic liquid (short-range positional and orientational order).

For a vortex system, the correlation function $C(r)$ is defined as $C(r) = \langle \rho_{\mathbf{G}}(\mathbf{r}) \cdot \rho^*_{\mathbf{G}}(\mathbf{0}) \rangle$, where $\rho_{\mathbf{G}}(\mathbf{r})$ is the local Fourier component of the vortex density evaluated at reciprocal lattice vector $\mathbf{G}$ [115]. The brackets signify the thermal average of the scalar product at two lattice points over all possible orderings.

Above the melting temperature T_m, the correlation function $C(r)$ begins to decay exponentially on a length scale given by the typical spacing between dislocations: $C(r) \sim e^{-r/\xi_+(T)}$, where the translation correlation length $\xi_+(T)$ scales with the inverse square-root of the density of free dislocations n_f. This is itself inversely proportional to the shear viscosity $\eta(T)$ [75]: $\eta(T,B) \sim 1/a_0^2 \tilde{\mu} n_f \sim \xi_+^2(T,B)$, with a_0 the lattice spacing and $\tilde{\mu}$ a typical dislocation mobility.

Approaching the solid to (*hexatic*) liquid melting transition, η mimics the strong divergence of ξ_+. The renormalization-group analysis gives the following result:

$$\xi_+ = \xi_{+0} exp[b'(\frac{T_m}{T - T_m})^{\nu}] \tag{5.8}$$

with $\nu = 0.36963...$ for triangular lattices, b' is non-universal constant of order unity. This divergence is faster than any power law defined by $\xi_+ \sim |T - T_m|^{-s}$ since the correlation length exponent $s = \infty$ in Equation (5.8).

The shear viscosity $\eta(T,B)$ thus follows an exponential divergence scaling approaching this transition, explicitly one has

$$\begin{aligned} \eta(T,B) &\sim \xi_{+0}^2 exp[2b'(\frac{T_m}{T - T_m})^{\nu}] \\ &\sim \xi_{+0}^2 exp[2b''(\frac{B_m}{B - B_m})^{\nu}] \end{aligned} \tag{5.9}$$

where $\nu = 0.36963...$ for triangular lattices, b', b'' are non-universal constants of order unity and $\xi_{+0} \approx a_0$ (the lattice spacing), being the smallest length scale of the system.

M. H. Theunissen et al. [76] performed the vortex liquid shear viscosity measurements in this channel confined geometry in two-dimensional $\alpha - Nb_3Ge$ films. The dependence of the measured vortex shear viscosity on temperature and on magnetic field showed a good agreement with the two-dimensional melting theory. The dependence of the melting temperature and the melting magnetic field on channel width measured in $\alpha - Nb_3Ge$ films also fitted well with the two-dimensional melting theory under the assumption that free dislocations in the liquid line up along the channel edges, i.e., the correlation length ξ_+ equals to the effective channel width w_{eff}.

5.1.5 Vortex shear viscosity in a Bose liquid

If the weakly pinning channels contain dilute columnar defects, the Bose-glass model may be applied to find a scaling form for resistivity [109]. In the following, T_{BG} denotes the Bose-glass transition temperature. In our study, the columnar defects are along the c-axis of the crystal. The magnetic field is applied along the columnar defects (see Figure 5.1 (a)).

The Bose glass correlation length in the ab-plane is: $\xi_\perp \sim |T - T_{BG}|^{-\nu_\perp}$ [109] while the correlation length along the field direction is: $\xi_{//} \sim \xi_\perp^\zeta \sim |T - T_{BG}|^{-\nu_\perp \zeta}$, with ζ the anisotropy exponent. In our case, for linear defects (columnar defects) illustrated in Figure 5.1 (a), one has: $\zeta = 2$. The correlation time controlling the relaxation of critical fluctuations is assumed to diverge as: $\tau \sim \xi_\perp^z$, with z the dynamic critical exponent [32]. The exponents have been determined via simulations to be $\nu_\perp \cong 1$ and $z \cong 4.6$ [116]. In bulk samples in three dimensions, the linear resistivity $\rho_\perp$ of the vortex liquid for currents applied in the ab plane is predicted to vanish as $T \to T_{BG}$ from above as: $\rho_\perp \sim |T - T_{BG}|^{\nu_\perp(z-2)}$ by scaling in the Bose glass model. If $\delta << L$, the bulk result is recovered:

$$\rho(T,L) \simeq \rho(T) \sim |T - T_{BG}|^{\nu_\perp(z-2)}. \tag{5.10}$$

In narrow channels, or near the Bose-glass transition, $\delta >> L$, and one has:

$$\rho(T) \sim L^2 |T - T_{BG}|^{\nu_\perp z}. \tag{5.11}$$

Since the resistivity is inversely proportional to the vortex shear viscosity, one finds: $\eta \sim |T - T_{BG}|^{-\nu_\perp z}$. Then the shear viscosity η is just proportional to the z-th power of the Bose glass correlation length $\xi_\perp$: $\eta \sim \xi_\perp^z$. The divergence of the shear viscosity is controlled by the dynamic exponent z.

The above results rest on the identification of the dynamic length scale δ with the static correlation length $\xi_\perp$ as stressed by M. C. Marchetti and D. R. Nelson [32]. We recall the result obtained in the theory of the continuous melting in two dimensions: $\eta \sim 1/\xi_d^2$, where η is the liquid shear viscosity and ξ_d the average distance between unbound dislocations, which diverges at the vortex lattice melting transition and results the divergence for the viscosity. In two dimensions, it is the dislocation-mediated melting mechanism

that establishes the precise relationship between static and dynamic correlation lengths. In three dimensions, for the vortex or Bose glass transitions, the relationship between static and dynamic correlation lengths is based on the assumption that the growing correlations associated with vortex localization in the disorder potential drives the divergence of dynamical properties, namely the viscosities, in the liquid phase.

5.1.6 Vortex liquid shear viscosity measurement in $Bi_2Sr_2CaCu_2O_8$

H. Pastoriza and P. H. Kes [72] have performed shear viscosity measurements on three-dimensional, heavy-ion irradiated $Bi_2Sr_2CaCu_2O_8$ single crystals containing 2.5 μm wide un-irradiated channels. Their results suggest that the vortex lattice shear modulus vanishes at the first order vortex lattice melting transition. However, the channels prepared in [**?**] were extended to the edges of the crystals, and the onset of vortex flow could be equally well explained by the demise of the surface barrier effects near to the first order vortex lattice melting transition [117].

D. T. Fuchs et al. have performed the transport measurements on $Bi_2Sr_2CaCu_2O_8$ single crystals of *square* and *strip* geometries (see Figure 5.4) [117]. The current injection contacts are far away from the edges for the square crystals. A *square* crystal of $1.3(w) \times 1.7(l) \times 0.013(d)$ mm^3 was cut to a *strip* crystal with a width of 0.29 *mm* (see the inset of Figure 5.4). Four Ag/Au pads for electrical contacts were thermally evaporated and had dimensions of 100×200 μm^2 with 75 μm separation. The same contacts were used for transport measurements in the *square* and *strip* geometries. The magnetic field was applied parallel to the crystalline c axis, and the resistance was measured using an *a.c.* bridge with four-point probe method.

The surface barrier dominates the vortex motion in the *strip* crystal and shows a highly nonlinear resistance at low currents in the liquid vortex state (see Figure 5.4), which tends to approach the bulk value, i.e., the resistance of the *square* crystal, as the current is increased. This nonlinear resistance in the liquid vortex state is due to the fact that the height of the surface barrier decreases with increasing transport current. At low currents, the surface barrier is very high and the resistance of the *strip* crystal is significantly reduced.

Since the surface barrier effect is more important in the *strip* crystal than the *square* crystal, a much stronger nonlinear behavior is observed in the *strip* crystal compared to the *square* crystal. The surface barrier plays an important role in vortex motion both in the vortex liquid phase and in the vortex solid phase. Figure 5.5 shows the normalized $R(T)$ curves in the vicinity of the first order transition (vortex solid-liquid transition) in the *strip* crystal and in the *square* crystal with 10 mA under a magnetic field of $H_{//c}$ = 300 Oe. In order to probe unambiguously the bulk properties of the vortex ensemble, the contacts for current injections in resistivity measurements and the channel structure should be remote from the sample edges.

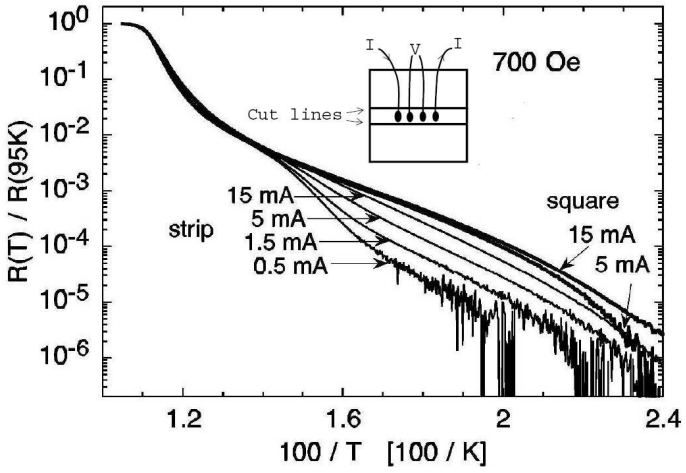

Figure 5.4: Arrhenius plot of the normalized resistance of $Bi_2Sr_2CaCu_2O_8$ crystal at $H_{//c}$ = 700 Oe. Thick curves: Resistance of the square sample with 5 and 15 mA current. Thin curves: Nonlinear resistance in the cut strip geometry for 0.5 to 15 mA currents. (Figure reproduced from [117])

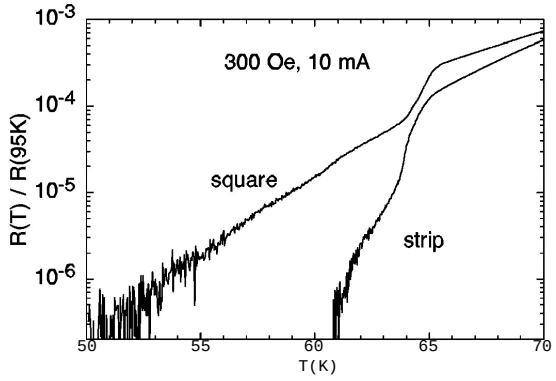

Figure 5.5: Normalized $R(T)$ of the *square* and *strip* crystal in the vicinity of the first order transition at $H_{//c}$ = 300 Oe and with 10 mA current. (Figure reproduced from [117])

5.2 Experimental details

The optimally doped $Bi_2Sr_2CaCu_2O_8$ single crystals ($T_c \approx 87$ K) that we use in this work were grown by Ming Li, of the research group of Professor P. H. Kes at the Kamerlingh Onnes Laboratory of Leiden University (the Netherlands). The samples were obtained from a batch grown using the traveling solvent floating zone technique under 200 mBar O_2 pressure, and were subsequently annealed in air at 800 °C for six hours [118], [119].

The channel confined geometry requires an array structure in which the weakly pinning channels are separated by strongly pinning walls. This can be achieved by selective

heavy ion irradiation at GANIL (Grand Accélérateur National d'Ions Lourds, situated in Caen, France) through a suitable nickel mask on the crystals.

The channels are weakly pinning on the condition that they do not contain any pre-existing macroscopic defects, for example, an inhomogeneous oxygen distribution or the intergrowth of other phases different from $Bi_2Sr_2CaCu_2O_8$ (Bi-2212). We therefore need to select $Bi_2Sr_2CaCu_2O_8$ crystals of the highest purity and free of any macroscopic defects prior to the irradiation.

5.2.1 Selection of $Bi_2Sr_2CaCu_2O_8$ crystals

During the selection step, we cleaved the crystals to obtain samples with a thickness less than 20 μm. This is because the range of 1 GeV Pb^{56+} ions in $Bi_2Sr_2CaCu_2O_8$ is about 30 μm [120]. In thicker crystals (more than 30 μm), the columnar tracks would not extend through the whole thickness since the ion energy drop below the threshold for track formation before leaving the sample. In crystals of intermediate thickness ($20 \sim 30$ μm), ions deviate from their trajectory. For further selection, we use the magneto-optical imaging technique.

Magneto-optical imaging provides an efficient way to detect macroscopic defects in superconductor crystals. The application of a magnetic field induces screening currents in the superconductor. If there is a defected region where the current flow is distorted, this is reflected in the magnetic field distribution, which may be observed in magneto-optical images.

The most commonly observed defect structures are:

1. Grain boundaries

Many seeds may be formed when a sample starts to crystallize, seeds grow until they meet at the boundaries. A grain is a single crystal. Properties along these boundaries are different from those inside the grains. For superconductors, the grain boundaries have a lower critical current density value than that found in a single crystal [121].

Single crystals can be obtained by cutting the crystal along its grain boundaries with a wire saw machine. The photo of the crystal shown in Figure 5.6 (a) was obtained through a polarized light microscope. We notice that very often the grain boundaries can be perceived directly prior to performing magneto-optical imaging measurements.

2. Arclike defects

The arclike defects revealed in Figure 5.7 (a) are due to the difficulty to regulate a constant rate of crystallization. The arclike defect structure is nearly perpendicular to the growth direction.

Differential Magneto-Optical (DMO) imaging shows that the *arcs* have a lower T_c than the *bulk*, typically $\Delta T_c \sim 1$ K. At a fixed temperature near T_c, flux penetration first occurs in the *arcs*, and then in the *bulk* [122]. The formation of the arclike defects is due

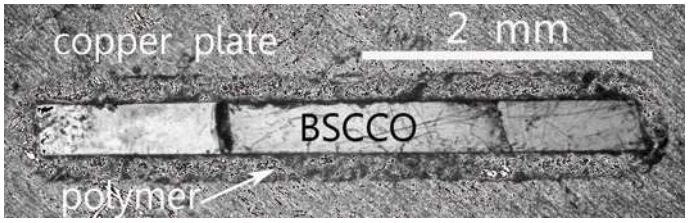

(a)

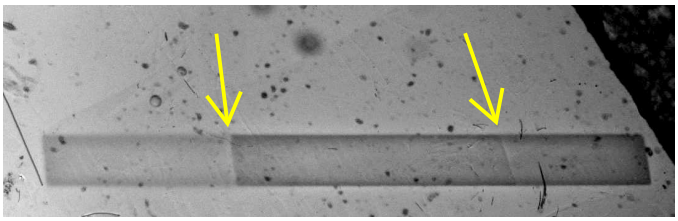

(b)

Figure 5.6: (a) The *BSCCO* crystal was glued to a thin copper plate with $n-C_{19}H_{40}$, a polymer the melting temperature of which is around 30 °C. (b) A magneto-optical image obtained at 23.52 K under a field of 140 Oe parallel to the *c-axis* of the *BSCCO* crystal. Flux penetration to the grain boundaries can be observed as indicated by the arrows.

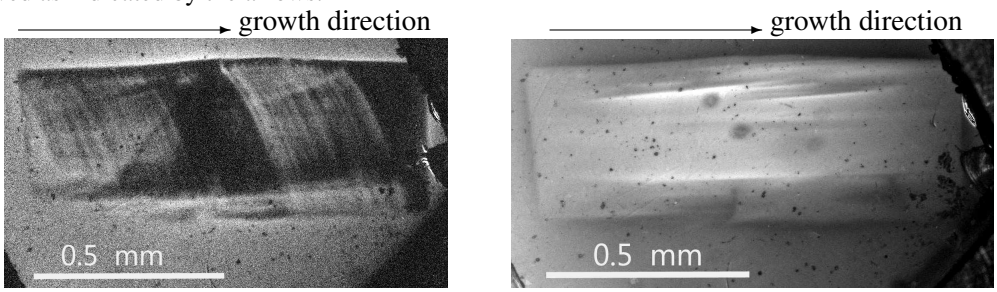

(a) (b)

Figure 5.7: Different kinds of defects revealed by the Magneto-Optical (MO) imaging technique in a *BSCCO* crystal (numerated as *BSCCO* 01-06-2007, with gold strip). (a) Arclike defects revealed by differential MO imaging at T = 83 K with a base field of zero, and a field modulation $\delta H_{//c}$ of 2 Oe along the *c*-axis of the *BSCCO* crystal. (b) Intergrowth defects revealed by direct MO imaging at T = 31 K with the application and removal of a field of 280 Oe parallel to the *c-axis*, in the same crystal as in (a).

to the thermal gradient during the crystal growth (see Figure 5.8).

3. Intergrowth defects

Due to the fact that $Bi_2Sr_2CaCu_2O_8$ melts incongruently, it is very difficult to maintain a stable molten zone during the crystal growth. In particular, a solid phase of different composition can form, appearing henceforth as a defect structure.

By performing magneto-optical imaging as well as transport measurements, M. Li et al. [123] have identified that the line defects (see Figure 5.7 (b)) occurring in $Bi_2Sr_2CaCu_2O_8$

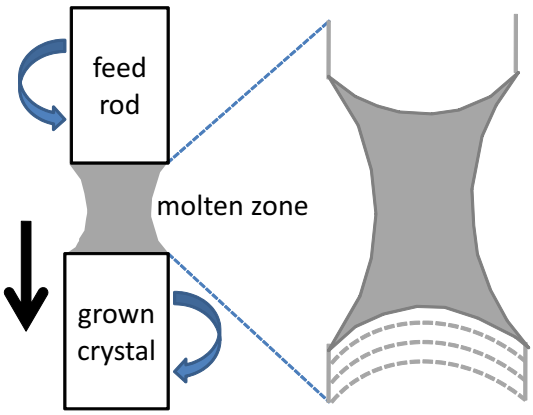

Figure 5.8: Sketch of the crystal growth process in the traveling floating zone method (left-hand panel). The feed and the seed shafts rotate in opposite directions. The right-hand panel shows a schematic expanded cross-sectional view of the molten zone. The growth front is curved by the thermal gradient. Arclike structures (broken lines) observed by magneto-optical imaging method are parallel to the growth front.

(Bi-2212) crystals grown in air are due to the intergrowth of the $Bi_2Sr_2Ca_2Cu_3O_{10+x}$ (Bi-2223) phase with a critical temperature near to 110 K. Magneto-optical imaging (see Figure 5.7 (b)) shows that the Bi-2223 phase forms as small needle shaped filaments oriented along the growth direction.

We remark that by the magneto-optical imaging technique, the Bi-2223 phase intergrowth defects (see Figure 5.7 (b)) are most noticeable at a temperature interval between 20 K and 35 K while the arclike defects (see Figure 5.7 (a)) are revealed at high temperatures close to T_c since the *arcs* have a lower T_c than the *bulk*.

4. Surface steps and embedded stacking defects

A dislocation cannot end within a crystal since it can only be contained within a crystal as a complete loop; the dislocation lines end at the sample surface. In single crystals, the majority of dislocations are formed at the surface. The small steps on the surface and the embedded stacking defects can be revealed by MO imaging technique. Figure 5.9 shows the surface step revealed by MO imaging. Clearly, crystals containing such defect structures are to be avoided for further study. The surface step defects can be avoided by cleaving the *BSCCO* single crystals between two *BiO* planes, since they are weakly bonded.

Selected homogeneous crystals are cut into square or rectangular pieces in order to obtain macroscopic defect-free single crystals. The selected single crystals are glued to nickel masks for the irradiation experiments. Figure 5.10 shows the MO images for a selected *BSCCO* crystal free of any macroscopic defect.

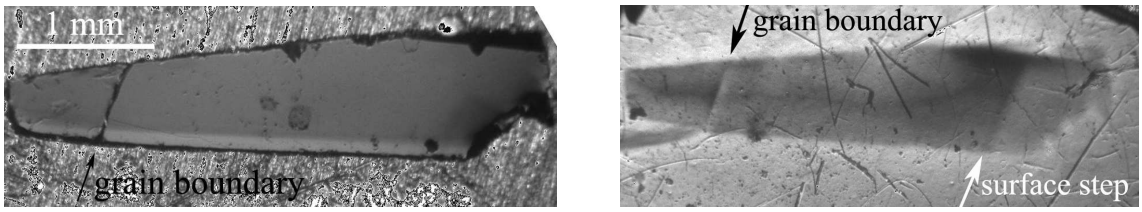

(a) (b)

Figure 5.9: (a) Photograph of the sample *BSCCO XII* through a polarized light microscope. (b) Direct MO image at T = 24.22 K, $H_{//c}$ = 363.1 Oe, after zero-field cooling. The left arrow marks the grain boundary defect, while the right arrow marks the surface step defect.

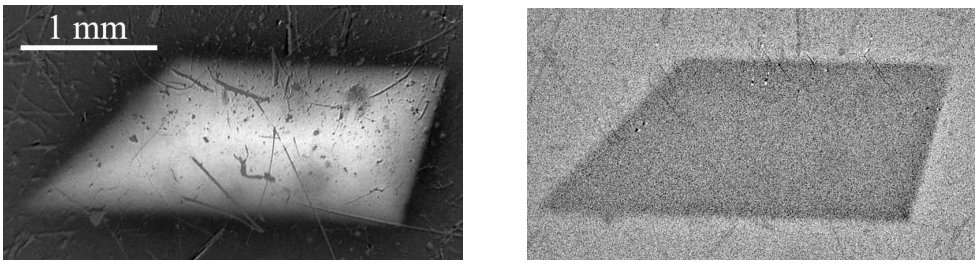

(a) (b)

Figure 5.10: MO images for a selected crystal (*BSCCO-III*) free of macroscopic defects. (a) Direct MO image of the remanent state at T = 23.8 K after the application and removal of a field of 273 Oe, parallel to the *c*-axis of the *BSCCO* crystal. (b) Field modulated DMO images of *BSCCO iii* at T = 83 K with field modulation of 0.5 Oe. The magnetic field is along the *c*-axis of the *BSCCO* crystal.

5.2.2 Fabrication of the nickel masks

The nickel masks were fabricated by electrodeposition at the Institute of Physics, Polish Academy of Sciences (Warsaw, Poland) by Dr. P. Gierlowski. In order to stop the high energy Pb^{56+} beam, 4 to 5 layers of Ni-masks with a thickness of $6 \sim 8$ μm were superposed.

Clear Ni-films with a well-defined apertures are thinner than 8 μm. Thicker films have blocked apertures with the electrodeposition method. Under an optical microscope, 4 to 5 layers of 8 μm thick Ni-films are aligned using a ring-shaped permanent magnet. The Ni-films were piled into masks for the heavy ion irradiation and glued together using an acrylocyanate glue.

5.2.3 Selective heavy ion irradiation to obtain the channel structure

Strongly pinning areas are introduced by selective irradiation through nickel masks (see Figure 5.11) using a 1 GeV Pb^{56+} beam. The Pb^{56+} ions create columnar defects along the *c*-axis in *BSCCO* crystals which provide the potential wells to pin the vortices. Two

fluences have been used to obtain the channel confined geometry: one is 1×10^{11} ions per cm^2 (a matching field of 2 T), another is 1×10^{10} ions per cm^2 (a matching field of 0.2 T).

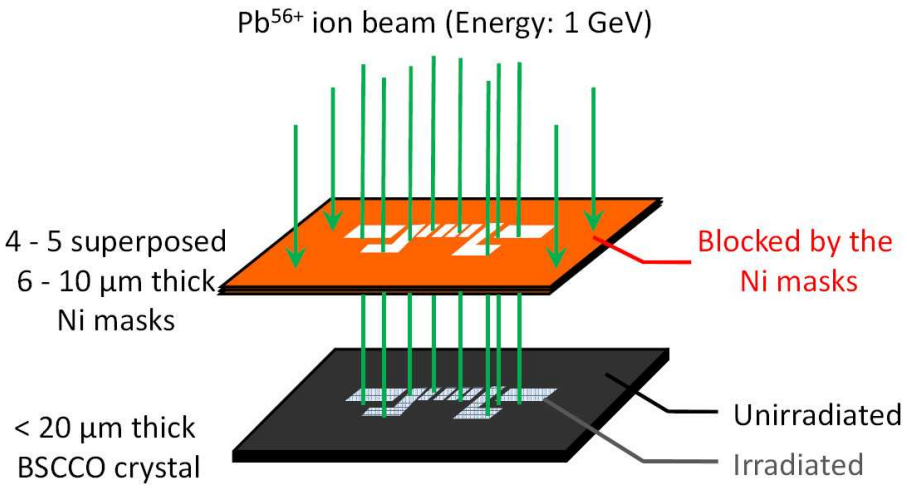

Figure 5.11: Selective irradiation through Ni masks.

The heavy ion irradiation causes a self-doping by oxygen displacements in $Bi_2Sr_2CaCu_2O_{8+\delta}$ crystals [119]. This effect modifies the critical temperature T_c. For an underdoped *BSCCO* crystal, after the heavy ion irradiation, its critical temperature T_c increases and for an optimally doped *BSCCO* crystal, after the heavy ion irradiation, its critical temperature T_c decreases. The variation of T_c is approximately 1 K for an equivalent irradiation dose of 2 Tesla.

For the optimally doped *BSCCO* crystal that we study, the critical temperature T_c for the strongly pinning walls is thus lower than that of the un-irradiated regions. To reduce this difference in T_c, the fluence of 1×10^{10} ions per cm^2 (a matching field of 0.2 T) is chosen.

Regions exposed to the ion beam are damaged and will contain many amorphous columnar latent tracks, which serve as strong pinning centers. By designing a mask such that only parallel rectangular regions of the crystals are exposed, we created strongly pinning walls artificially (see Figure 5.11).

Masks with different channel widths (5 μm, 10 μm, and 20 μm) were prepared for heavy ion irradiation experiment. But our irradiation results showed that only the masks with a channel width of 20 μm produced well-defined channel structures in the *BSCCO* crystals. The masks with channel widths of 5 μm and 10 μm produced ill-defined apertures in *BSCCO* crystals, i.e., the strongly pinning walls and the channels were not clearly separated. In the following, relevant MO images serving to check the selective irradiation experiment are presented.

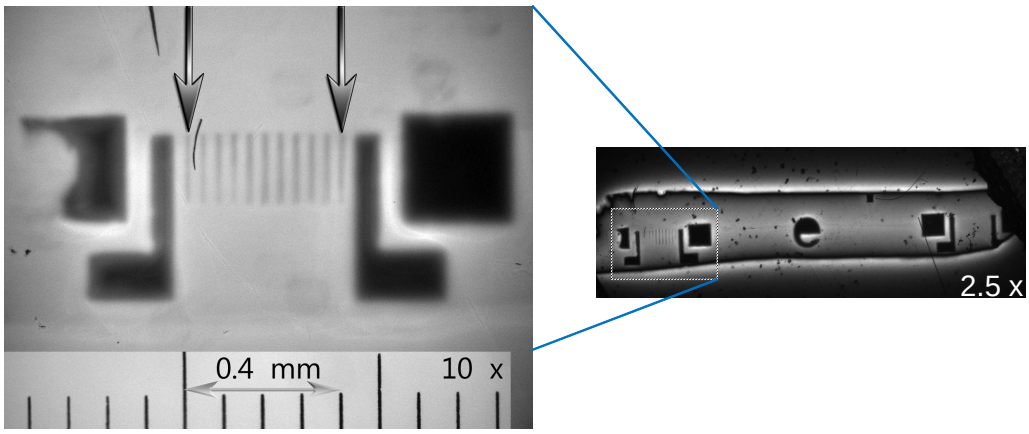

Figure 5.12: Channel structure examined by MO imaging for the sample *BSCCO 24-4*, B_ϕ = 0.2 T. Left-hand panel: direct MO Image (10 x) at T = 34 K, $H_{//c}$ = 418 Oe, after zero-field cooling. Right-hand panel: direct MO image (2.5 x) obtained at T = 5 K, with the application and removal of a field of $H_{//c}$ = 456 Oe.

5.2.4 Sample check by magneto-optical imaging after selective heavy ion irradiation

The channel structures were characterized using the Magneto-Optical (MO) imaging technique. The left-hand panel of Figure 5.12 shows a direct magneto-optical image taken at T = 34 K under a field of $H_{//c}$ = 418 Oe along the *c-axis* of the crystal *BSCCO "24-4"*. After zero-field cooling, the irradiated areas (dark regions) screen out the magnetic field, while the rest of the crystal (bright regions) is penetrated by the magnetic field.

The channel structure is clearly revealed by the MOI technique (see Figure 5.12). The irradiated, strongly pinning walls do not admit the vortices and show up as dark areas. The channel structure indicated by two arrows include 10 channels (showing up as bright) and 10 pinning walls (showing up as dark). The distance between the two arrows is 400 μm. The channel width is thus $L = \frac{400}{10} \cdot \frac{1}{2} = 20\ \mu m$.

The heavily irradiated square pads are for current injection and the two contact pads inside are for voltage measurements. Within the pads, below a certain temperature and a certain magnetic field, i.e., below the irreversibility line of the strongly irradiated pinning walls, there is no flux flow so that only the voltage drop over the channel structure is measured.

The heavily irradiated part has a lowered critical temperature. As we have mentioned in the last section, the variation of T_c is approximately 1 K for an equivalent irradiation dose of B_ϕ = 2 Tesla. The decrease of T_c for optimally-doped *BSCCO* samples due to heavy ion irradiation could be observed by magneto-optical imaging. Here we report on the sample denoted as *BSCCO "iv"* ($1800 \times 1750 \times 20\ \mu m^3$), the irradiation dose is B_ϕ = 2 Tesla and its critical temperature is $T_c \approx 87.5$ K for the unirradiated part.

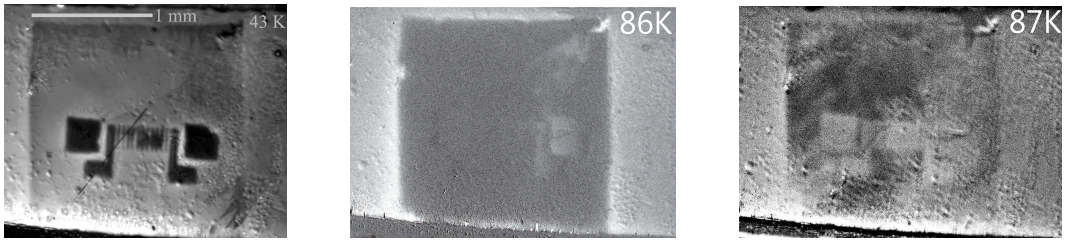

(a) (b) (c)

Figure 5.13: Variation of T_c in *BSCCO* due to the self-doping mechanism induced by heavy ion irradiation, observed by MO imaging. (a) Direct MO image at T = 43 K, under a field of $H_{//c}$ = 97 Oe. The heavily irradiated parts screen out the magnetic field and appear as dark regions. (b) Differential MO image at T = 86 K, $H_{//c}$ = 0 with a modulation field $\delta H_{//c}$ = 1 Oe. The heavily irradiated part has a lower T_c than the unirradiated part. The magnetic flux begins to penetrate first to the irradiated part, which shows up as bright regions (the irradiated pad on the right is bright). (c) Differential MO image at T = 87 K, $H_{//c}$ = 0 with a modulation field $\delta H_{//c}$ = 1 Oe. Since the heavily irradiated part has a lower T_c than the unirradiated part, the magnetic flux penetrates to the irradiated part which shows up as bright areas. At 87 K, the whole irradiated part shows up bright [122].

Figure 5.13 (a) is a direct MO image taken at T = 43 K under a field $H_{//c}$ = 97 Oe, parallel to the *c*-axis of the crystal *BSCCO iv*. The heavily irradiated part appears dark in the image since magnetic field is screened out. Figure 5.13 (b) and (c) are DMO images taken near to T_c, we see that, contrary to the situation in Figure 5.13 (a), magnetic flux penetrates to the irradiated regions first because of the lowered T_c in those regions.

Here are other examples (see Figure 5.14, Figure 5.15 and Figure 5.16) of well-defined channel structure created through selective Pb^{56+} ion irradiation experiment with the Ni masks. The channel structure can be also perceived directly through an optical microscope, see e.g. in sample *BSCCO "20"* (see Figure 5.15 (a)) and *BSCCO "25-4"* (see Figure 5.16 (a)).

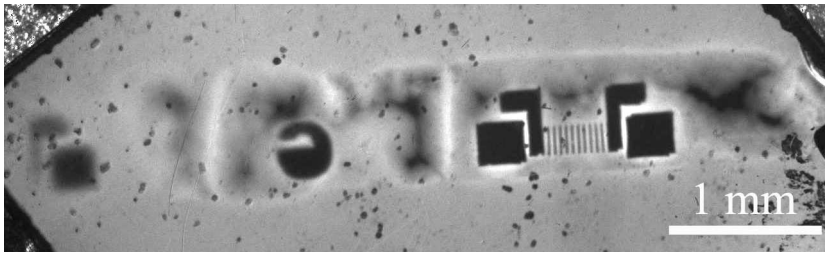

Figure 5.14: Channel structure examined by MO imaging for the crystal *BSCCO "24-3"*, B_ϕ = 2 T. Figure shows a direct MO image of this sample taken at T = 7 K, $H_{//c}$ = 457 Oe.

Examples of ill-defined channel structure or perturbed by other macroscopic defects are presented below. In Figure 5.17, the channels and the strongly pinning walls are not

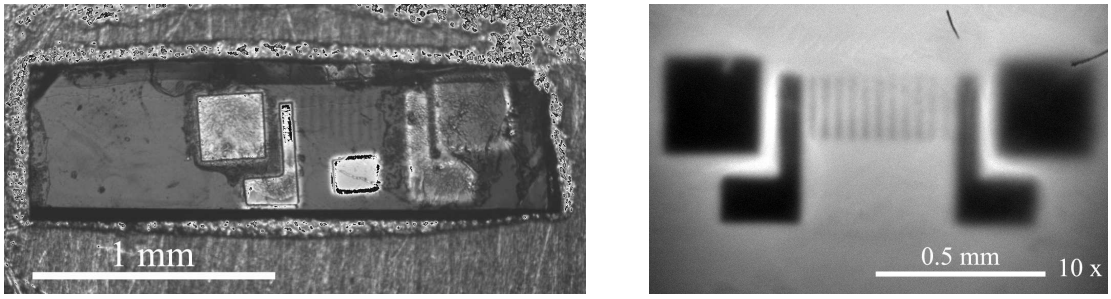

(a) (b)

Figure 5.15: Channel structure examined by MO imaging for the sample *BSCCO 20*, B_ϕ = 2 T. (a) Photograph of the sample *BSCCO 20* with the Au contacts added by evaporation through an identical Ni-mask as that used in the selective irradiation experiments. (b) Direct MO image of *BSCCO "20"* taken at T = 33.6 K, $H_{//c}$ = 342 Oe.

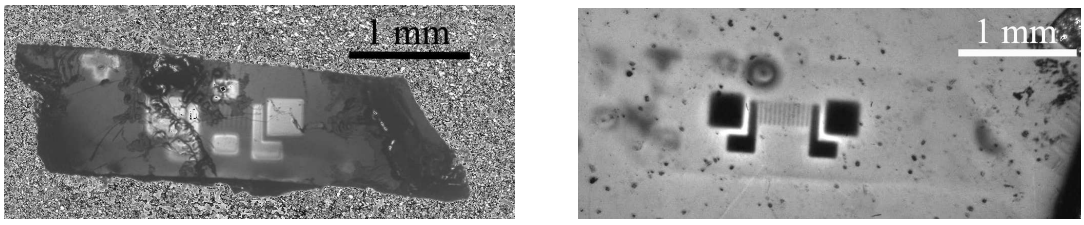

(a) (b)

Figure 5.16: Channel structure examined by MO imaging for the sample *BSCCO 25-4*, B_ϕ = 2 T. (a) Photograph of the sample *BSCCO 25-4*. (b) Direct MO image of *BSCCO "25-4"* taken at T = 34.3 K, $H_{//c}$ = 300 Oe.

totally separated. In Figure 5.18, the channel structure is disturbed by another macroscopic defect.

5.2.5 Small dose uniform re-irradiation

In order to compare our results to the predictions [109] for the Bose liquid vortex, we have re-irradiated several crystals uniformly (see Figure 5.19) with a fluence of 5×10^7 Pb^{56+} ions per cm^2 (1 GeV). This corresponds to a matching field of B_ϕ = 10 G. Such crystals were compared to homogenously irradiated crystals without channel structure.

For example, a single crystal denoted as *BSCCO "24-4"*, containing a channel structure with pinning walls of defect density corresponding to $B_\phi = 0.2$ T was homogeneously re-irradiated to a fluence corresponding to $B_\phi = 10$ G (1 mT). After irradiation, the crystals were glued on a 200 μm-thick sapphire substrate with Norland Optical Adhesive (NOA 61). Since the surfaces of the $Bi_2Sr_2CaCu_2O_8$ single crystals after irradiation are not very clean in general, a plasma etching for cleaning the surfaces is used: 2 minutes in a plasma

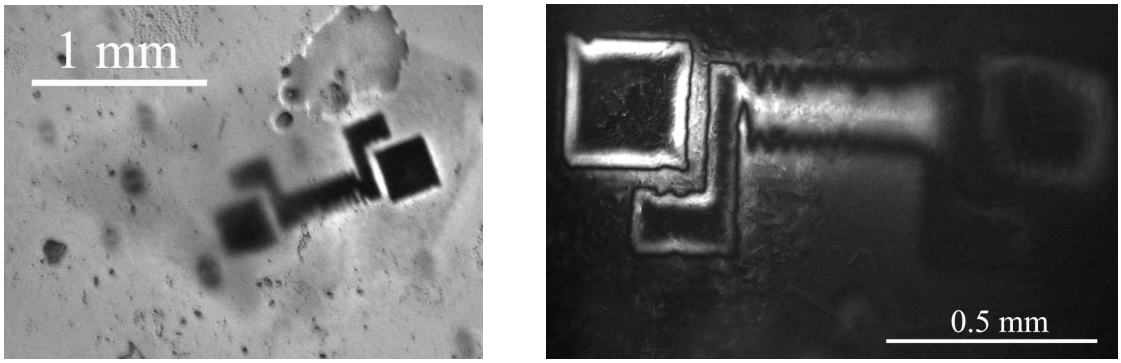

(a) (b)

Figure 5.17: Ill-defined channel structure illustration. The *hairline* one sees on the images is due to a defect (a) Direct MO image (2.5 ×) taken at T = 25.63 K, $H_{//c}$ = 354.7 Oe in sample *BSCCO 2.3*. (b) Direct MO image (10 ×) taken at T = 35.29 K with the application and removal of a field of $H_{//c}$ = 354.7 Oe in sample *BSCCO "2.3"*.

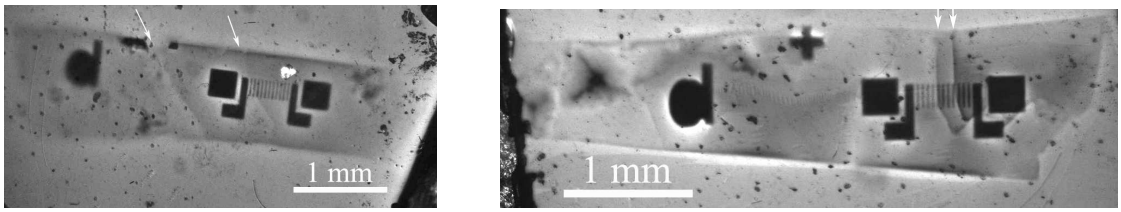

(a) (b)

Figure 5.18: Channel structure perturbed by surface steps, marked by the arrows. (a) Direct MO image taken at T = 32.66 K, $H_{//c}$ = 333 Oe in sample *BSCCO 23-2*. (b) Direct MO image taken at T = 25.93 K, $H_{//c}$ = 274 Oe in sample *BSCCO "26"*.

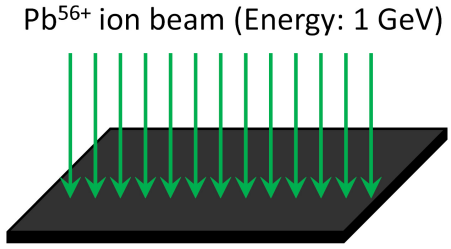

Figure 5.19: Uniform irradiation.

Ar/O_2 (ratio 1:4) with a pressure of 1×10^{-2} mbar and a power of 15 W. Photolithography technique was used to establish electrical contacts on the crystals for transport measurements. The procedure was detailed in Chapter 3.

5.3 Competition between surface pinning and bulk pinning

One expects to obtain a current flow through the channels with the help of the heavily irradiated current injection pads situated in the center of the samples. Both the bulk pinning and the surface pinning contribute to flux pinning in a type II superconducting sample; these pinning mechanisms compete with each other. In [117] and [124], it was reported that surface barriers significantly affect vortex motion in $Bi_2Sr_2CaCu_2O_8$ single crystals. On the contrary, the authors of Ref. [125] assert that the effect of surface barriers on vortex motion in $Bi_2Sr_2CaCu_2O_8$ single crystals can be neglected, *i.e.* vortex motion is essentially governed by bulk effects. The field-modulated DMO imaging technique provides a contact-free method to experimentally determine whether the bulk pinning or surface pinning dominates vortex motion in a specific sample in different temperature and magnetic field regimes.

As we have already seen in Chapter 2, the gradient of the intensity in the field modulated DMO images is related to the local critical current density value. If this gradient is no longer discernable over some superconducting regions, *i.e.* when one can no longer distinguish the superconducting region from the surrounding background, the local critical current density has all but vanished. This is the principle we use for the determination of the position of the irreversibility lines from field-modulated DMO images.

As an example, observing the field-modulated DMO images obtained on crystal *BSCCO "iv"* (see Figure 5.20), one sees that, below 82.5 K[1], for fixed temperature and increasing field, the edges of the sample vanish from view before the irradiated contact pads and the strongly pinning walls introduced by Pb^{56+} ion irradiation in field modulated DMO images. If one denotes H_{irr}^{edges} as the irreversibility field value for the edges and H_{irr}^{pads} as the irreversibility field value for the irradiated pads and the strong pinning walls created through irradiation, one has $H_{irr}^{edges} < H_{irr}^{pads}$. This result suggests that below 82.5 K, the edges are more resistive than the irradiated regions and the bulk pinning dominates vortex motion in the sample *BSCCO iv* in transport measurements.

For the crystals *BSCCO "24-4"* (see Figure 5.21) and *BSCCO "042008-17"* (see Figure 5.22), one also finds that under fixed temperatures, upon field increasing, the edges vanish before the irradiated pads and the strong pinning walls. Furthermore, the current is injected through the irradiated pads, which are remote from sample edges, for transport measurements. The resistance data obtained in this way on samples *BSCCO "iv"*, *BSCCO*

[1] For the high temperature part (near to T_c), the situation is different: (1) The heavily Pb^{56+} ion irradiated part has a shifted T_c. For optimally-doped *BSCCO* crystals, the T_c was lowered after Pb^{56+} ion irradiation. (2) The columnar defect pinning is very weak at this temperature regime and can be ignored. The presence of the columnar defects should have little influence to the thermodynamic melting transition. Since we are interested by the divergence behavior of the shear viscosity at liquid vortex phase, the regime at high temperature near to T_c is irrelevant to our study and we will discuss this point at the end of this Chapter.

(a) (b) (c)

Figure 5.20: Field modulated *DMO* images of *BSCCO iv* at T = 80.5 K with field modulation of 0.5 Oe. The magnetic field is along the *c*-axis of the *BSCCO* crystal. (a) base field = 0. (b) base field = 10 Oe. (c) base field = 25 Oe.

"24-4", and *BSCCO "042008-17"* at their liquid vortex states should be nearly unaffected by the surface barrier effects.

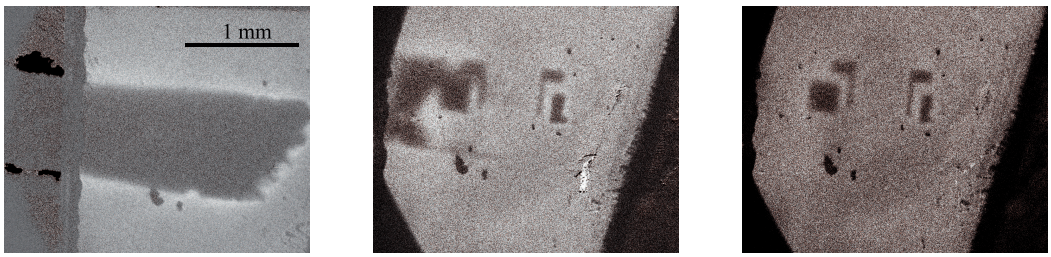

(a) (b) (c)

Figure 5.21: Field modulated *DMO* images of *BSCCO "24-4"* at T = 77 K with field modulation of 0.5 Oe. The magnetic field is along the *c*-axis of the *BSCCO* crystal. (a) base field = 30 Oe. (b) base field = 85 Oe. (c) base field = 110 Oe.

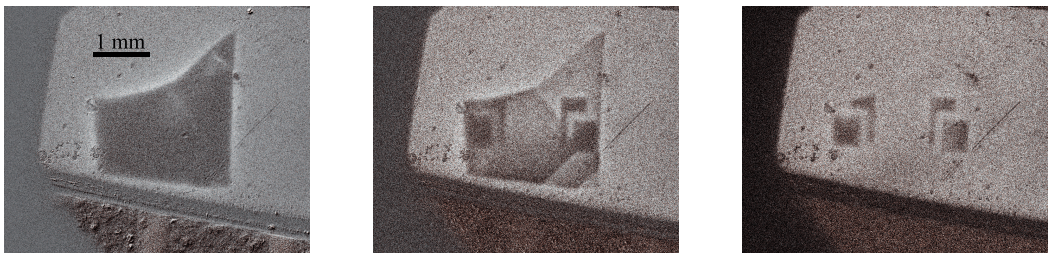

(a) (b) (c)

Figure 5.22: Field modulated *DMO* images of *BSCCO "042008-17"* at T = 79 K with field modulation of 0.5 Oe. The magnetic field is along the *c*-axis of the *BSCCO* crystal. (a) base field = 2 Oe. (b) base field = 16 Oe. (c) base field = 36 Oe.

Since the surface barriers contribute to a strongly nonlinear resistance even in the vortex liquid phase (see Figure 5.4), if one performs resistance measurements with different

currents on a superconducting sample, one can infer from the presence or absence of this nonlinear resistive behavior whether the surface barriers dominate the vortex transport properties. Turning to the crystal *BSCCO "iv"*, with dimensions $1800\times1750\times20$ μm^3, the dc current is injected through the two bottom exterior pads and the potential differences are measured between the two bottom interior pads (see Figure 5.24 (a)). To avoid Joule heating, the applied transport current did not exceed 10 mA.

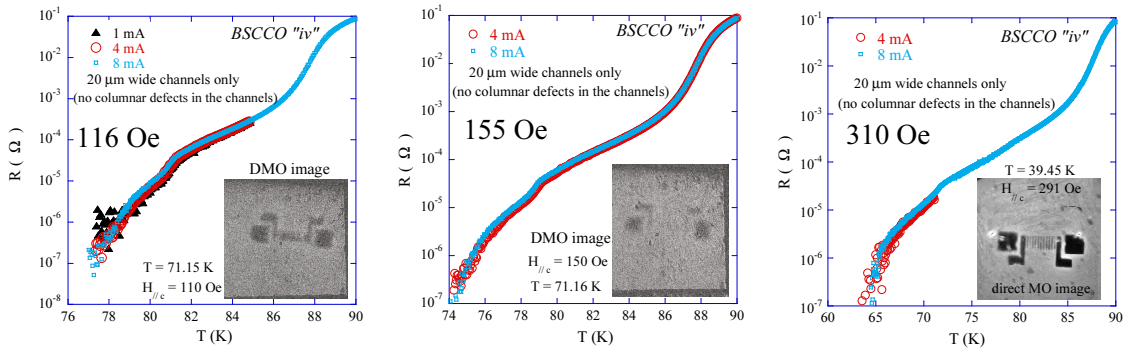

(a) (b) (c)

Figure 5.23: Resistance as a function of the temperature of *BSCCO "iv"* (channels only, no columnar defects in the channels) measured with different currents. (a) $H_{//c}$ = 116 Oe, with three different currents: 1 mA, 4 mA, and 8 mA. Inset: Field modulated DMO image at T = 71.15 K, $H_{//c}$ = 110 Oe, field modulation $\delta H_{//c}$ = 1 Oe. The magnetic field is screened by the strongly pinning walls and the contact pads, but not the sample edges. (b) $H_{//c}$ = 155 Oe, with two different currents: 4 mA and 8 mA. Inset: Field modulated DMO image at T = 71.16 K, $H_{//c}$ = 150 Oe, field modulation $\delta H_{//c}$ = 1 Oe. The magnetic field is screened by the strongly pinning contact pads but not the sample edges. (c) $H_{//c}$ = 310 Oe, with two different currents: 4 mA and 8 mA. Inset: Direct MO image at T = 39.45 K, $H_{//c}$ = 290.8 Oe. Sample edges are visible but the contrast at the edges, i.e., gradient of the vortex intensity, is much less important compared to that of the strongly pinning walls and contact pads.

A strongly nonlinear resistive behavior is not observed in the vortex liquid state in this crystal. Figure 5.23 shows the resistance as function of the temperature measured with different currents under different magnetic fields (along the crystal c-axis), varied from 116 Oe to 310 Oe. These data confirm that surface barrier effects are weak in this sample and that the current flows essentially in the bulk.

In addition, imaging of the self-field due to transport current using current-modulated magneto-optical imaging has been performed to study the current flow path and the efficiency of the irradiated contact pads. A current of 10 mA was applied, and ten magneto-optical images were acquired and summed; A current of the same value but of the opposite polarity (- 10 mA) was applied and ten other images were acquired and successively subtracted from the first sum. In order to increase the signal to noise ratio to obtain satisfactory self-field images, this procedure was repeated 20 times or even up to 100 times and the resulting images were averaged to produce the final self-field image due to transport current.

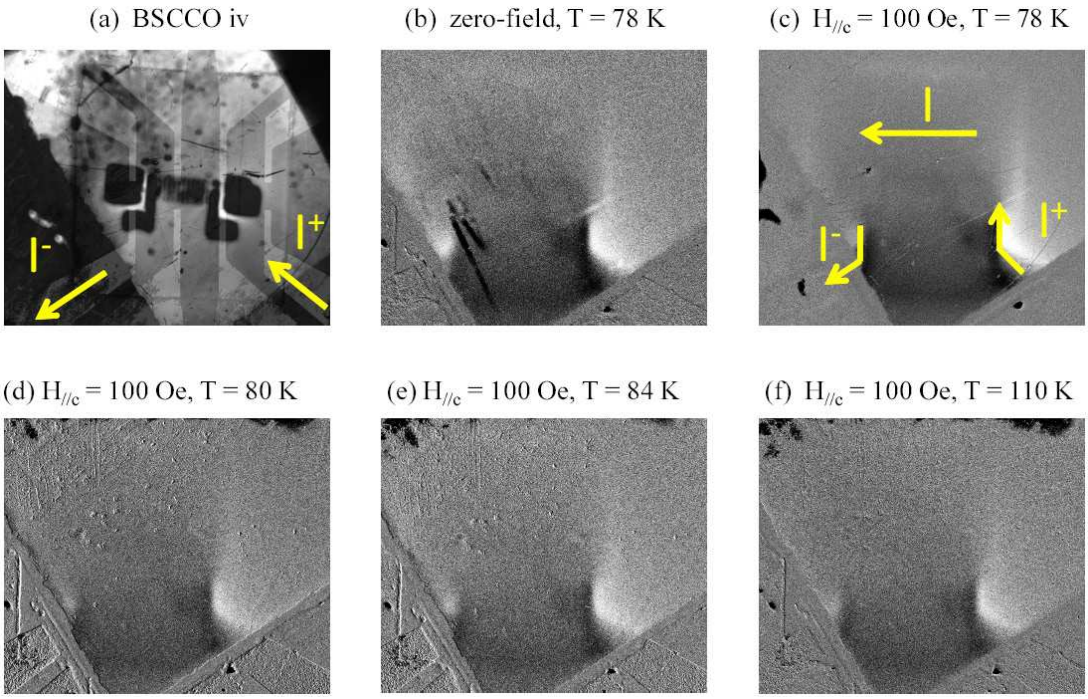

Figure 5.24: Current-modulated magneto-optical images obtained for *BSCCO "iv"* with current I = ± 25 mA.

Figure 5.24 shows the self-field images obtained for sample *BSCCO "iv"*. The current entry and exit path, defined by a sharp contrast on the current-modulated magneto-optical images, can be clearly recognized using the right-hand rule.

Even though the images obtained by differential magneto-optical imaging with current modulation (Figure 5.24) always show visible sample edges, we cannot immediately deduce that a part of transport current flows by the edges since the differential image acquired is always convoluted by the corresponding direct image (see Chapter 2). The self-field image obtained with current modulation under a magnetic field in the way described above is generated by the shielding current *and* the transport current. The shielding current always renders the sample edges visible. In the case where the current flows essentially though the bulk, the current-modulated Differential Magneto-Optical (*DMO*) images also produce visible sample edges.

Figure 5.25 shows a current-modulated DMO image acquired for the sample *BSCCO "24-4"*. Due to the shielding current, the sample edges are visible. The irradiated pattern and the current exit are clearly revealed in Figure 5.25. The characteristic contrasts[2] associated with the transport current show that the current flows through the irradiated pads.

[2] Figure 4.7 in Chapter 4 shows a comparison between shielding current and transport current in magneto-optical images.

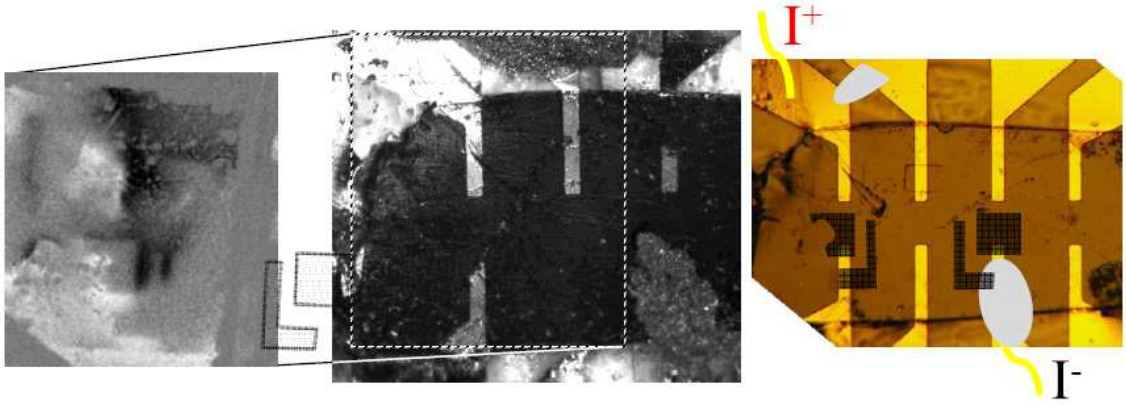

Figure 5.25: Current-modulated magneto-optical image obtained for *BSCCO "24-4"* at T = 68 K, with current I = ± 30 mA and under a field of 100 Oe parallel to the *c-axis* of the crystal.

This is direct evidence for the efficiency of the irradiated contact pads to "*attract*" the current. The transport current circulates through the irradiated regions since there is strong pinning there which provides a larger critical current density j_c and consequently a lower resistance compared to the unirradiated parts, including the sample edges. We remark that the current flows through the Au pattern (added by photolithography) until it reaches the irradiated pads (Figure 5.24 and 5.25).

5.3.1 Correspondences between the magneto-optical measurements and the resistance measurements

Resistance measurements performed on *BSCCO "iv"* in different magnetic fields parallel to its crystalline *c*-axis are shown in Figure 5.26. The kink points on the resistance curves are marked by the arrows T_{irr}^{CD} in Figure 5.26.

Except for the high temperature part[3] (near to T_c), the kink points on the resistance curves, correspond to the temperatures at which pinning in the heavily irradiated walls becomes effective which causes a sharp decrease of the resistance. Figure 5.27 shows the characteristic lines of *BSCCO "iv"* obtained from DMO imaging measurements and resistivity measurements. The line formed by the kink points identified from the resistance curves, marked by the arrows T_{irr}^{CD} in Figure 5.26, is superposed on the irreversibility line

[3] The kink point at high temperature may correspond to a vortex liquid-lattice melting transition but could also be attributed to the surface barrier effect.

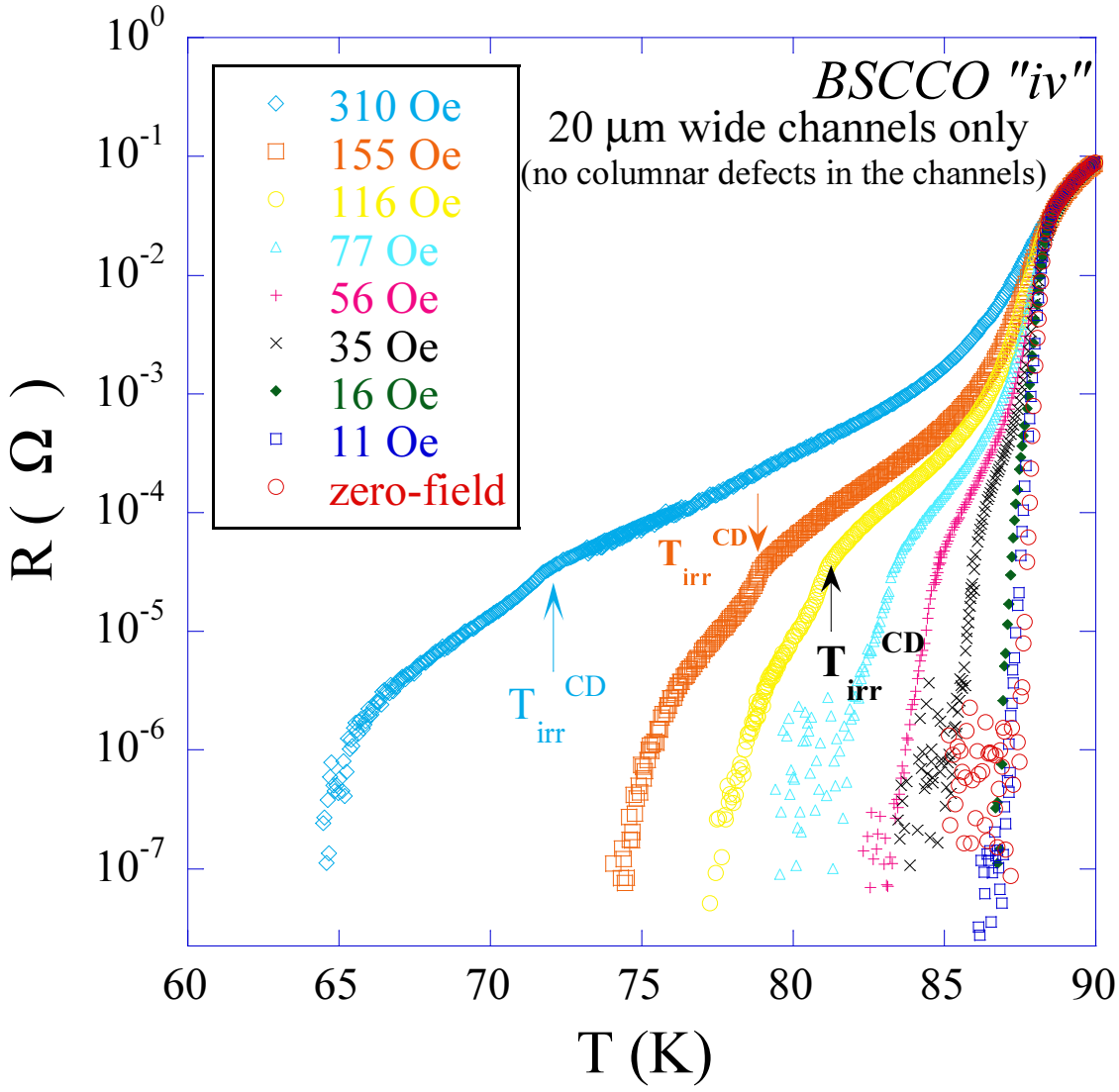

Figure 5.26: Resistance as a function of the temperature in different magnetic fields parallel to its crystalline *c*-axis. The transport current is 8 mA for all the measurements. Measured during the cooling.

derived from the field modulated DMO images[4]. These two lines correspond to the same physical origin: the onset of strong pinning by the heavily irradiated walls. Below this

[4] Because of the spatial resolution limit and the weakened signal due to the thickness of the gold layer (0.5 μm), it was difficult to clearly resolve the channels in the DMO images. Since the irradiation dose for the strongly pinning walls was the same as the irradiated contact pads, one can associate the onset of pinning in the irradiated contact pads as an indication for the effectiveness of pinning in the heavily irradiated walls. The irreversibility line for the strongly pinning walls is derived from the field-modulated DMO images in this manner.

line, the shear flow of the liquid vortex is realized in the channels.

If one plots the line $R = 10^{-7}$ Ω, determined from resistance measurements, and the irreversibility line for the edges, determined by the field modulated *DMO* images on this $H - T$ graph, one finds that these two lines are also superposed (see Figure 5.27). From this point of view, the resistivity data should be unaffected by the surface barriers in *BSCCO "iv"* for T < 82 K until approaching 10^{-7} Ω. This conclusion is consistent with the absence of nonlinear resistance at the liquid vortex state (see Figure 5.23). The resistivity data measured in the way that we described in this Chapter allows one to probe the bulk properties of the vortex system and furthermore, since the vortex motion is confined in the channels, one obtains directly the shear properties from the resistivity measurements.

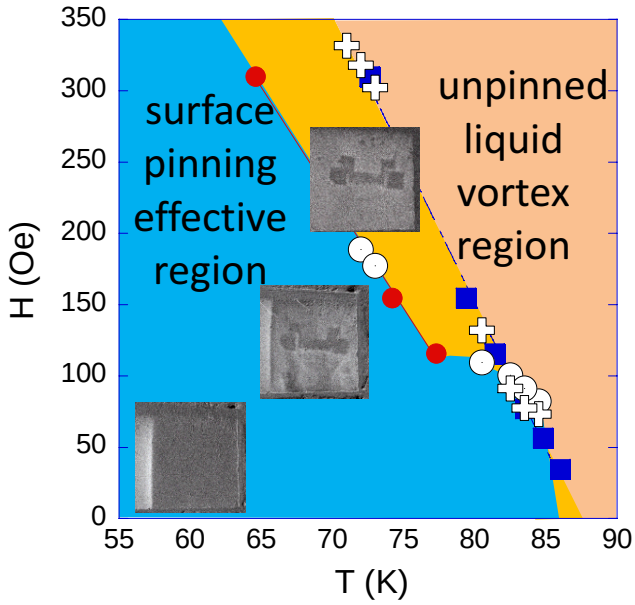

Figure 5.27: Characteristic lines of *BSCCO iv* derived from resistance measurements and field modulated *DMO* images. The fulfilled blue squares correspond to the *kink points* marked by the arrows T_{irr}^{CD} on the resistance curves in Figure 5.26. The unfilled black plus (+) signs refers to the irreversibility field and temperature of the strongly pinning walls determined from DMO images. The line formed by the fulfilled red circles correspond to the $R = 10^{-7}$ Ω line determined from resistance measurements. The unfilled black circles refers to the irreversibility field and temperature of the sample edges determined from DMO images.

5.3.2 Comparison of different types of confinement

Figure 5.28 shows the temperature dependance of the resistance for four crystals (*BSCCO "ref"*, *BSCCO "iv"*, *BSCCO "24-4"* and *BSCCO "10G"*) under the fields $H_{//c}$ = 116 Oe and $H_{//c}$ = 155 Oe. The first crystal is an unirradiated reference sample. The resistance has been renormalized to the normal resistance value of *BSCCO "iv"* for comparison.

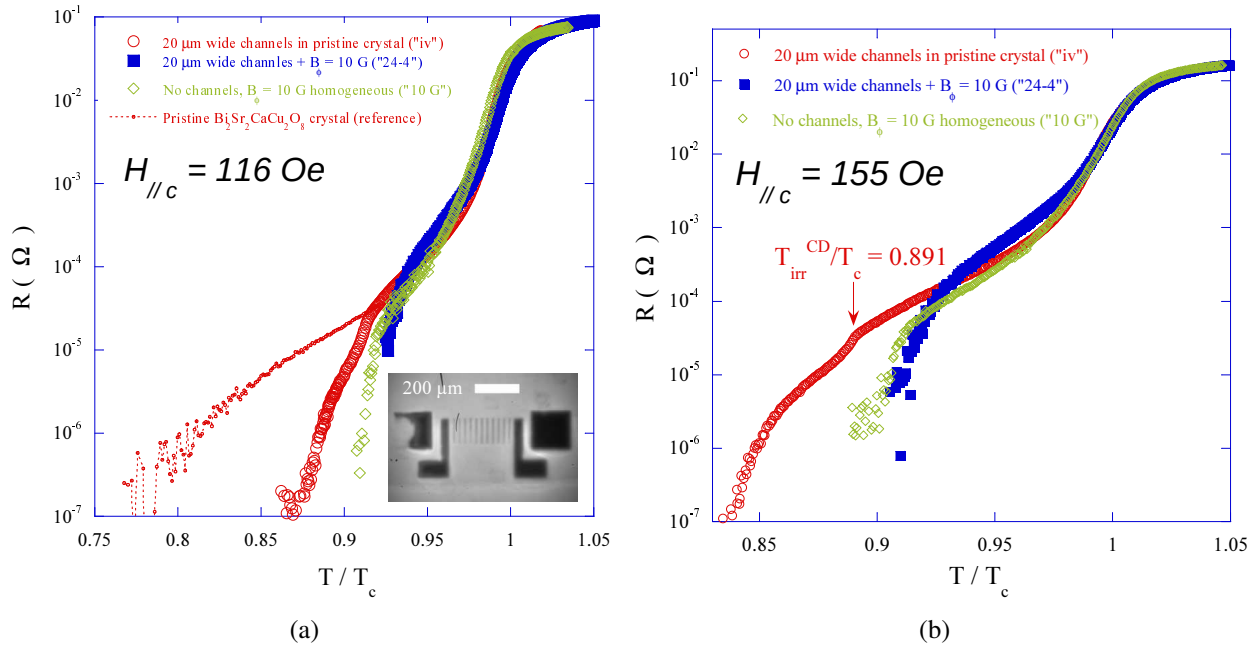

Figure 5.28: Renormalized resistance as a function of the temperature for three $Bi_2Sr_2CaCu_2O_8$ crystals. (a) Resistance data under the field $H_{//c}$ = 116 Oe. The thin line presents the resistance data of a pristine sample under the same magnetic field (multiplied by a factor of 0.024 for comparison). It shows the continuation of the resistance for a sample without confinement effect. Inset: direct magneto-optical image of the central part of the crystal *BSCCO "24-4"*, taken as T = 35 K and an applied field $H_{//c}$ = 456 Oe. The bright regions correspond to those parts of the crystal that are penetrated by the magnetic field and the dark regions are the irradiated areas that screen the magnetic field. (b) Resistance data under the field $H_{//c}$ = 155 Oe.

Two of the crystals (*BSCCO "iv"* and *BSCCO "24-4"*) contain a channel confined structure created by selective Pb^{56+} ion irradiation through the Ni-masks with 1×10^{11} and 1×10^{10} columnar defects per cm^2 respectively (dose-matching field B_ϕ = 2 T for *BSCCO "iv"* and B_ϕ = 0.2 T for *BSCCO "24-4"*). This difference in irradiation dose is irrelevant for the physics that we discuss here since the field applied in our study is much lower than 0.2 T. The crystal *BSCCO "iv"* was only irradiated once through the Ni-masks so that the channels in the crystal *BSCCO "iv"* are free of defects compared to the crystal *BSCCO "24-4"* which was subsequently homogeneously irradiated with a fluence of 5×10^7 cm^{-2} 1 Gev Pb^{+56} ions (dose-matching field B_ϕ = 10 G), producing weakly pinning channels that contain a low density of columnar defects. The last crystal *BSCCO "10 G"* was only homogeneously irradiated with a fluence of 5×10^7 cm^{-2} 1 Gev Pb^{+56} ions (dose-matching field B_ϕ = 10 G) serving as the reference for comparison.

The signature of the strong pinning by the walls is clearly observable at T_{irr}^{CD}/T_c = 0.891 and is indicated by the arrow in Figure 5.28 (b). The presence of the strongly pinning walls clearly reduces the resistivity with respect to the un-irradiated crystal (see

Figure 5.28 (a)). The resistivity at temperatures below the "*knees*" in Figure 5.28 is determined by the flow of the vortex liquid through the 20 μm-wide channels, and is therefore inversely proportional to the vortex liquid shear viscosity. An even stronger decrease of the resistance due to the addition of a small columnar defect density was observed. The resistance of the crystal *BSCCO "24-4"* (20 μm wide channels plus 5×10^7 cm^{-2} columnar defects, matching field B_ϕ = 10 G) follows nearly the same temperature dependance as that of the crystal *BSCCO "10G"*.

Thus, the small dose of irradiation (matching field B_ϕ = 10 G) significantly reduces the resistivity. Here we provide an explanation: The vortices localized on the columnar defects due to the Pb^{56+} ion irradiation with a matching field of B_ϕ = 10 G form a rigid matrix (see Figure 5.1 (b)). This rigid matrix may play the same role as the channel confined geometry. Along with this assumption, the rigid matrix defines an equivalent confined geometry whose characteristic channel width is the average grain size. For a matching field of B_ϕ = 10 G, the grain size is about $1 \sim 5$ μm. Since it is the smaller length between the channel width L (20 μm) and the average grain size D_{av} that should be compared to the correlation length at the vortex liquid-solid transition, the channel structure may have little effect on the vortex dynamics in this situation.

5.4 Confrontation between theory and resistivity data

We now compare the temperature dependence of the resistivity due to vortex shear, i.e., below the "*knees*", to the Nelson-Halperin model (continuous melting by dislocation unbinding) and the Bose-glass model, which yield different scaling laws for the divergence behavior of the shear viscosity, and consequently yield different scaling laws describing the vanishing of the resistivity approaching the *solidification* transition.

In the Nelson-Halperin model, the scaling law of resistivity (under a constant magnetic field) is expressed as follows:

$$\rho(T) \approx C_1 exp[-2C_2(\frac{T_m}{T-T_m})^{0.37}] \tag{5.12}$$

where C_1 is approximately the corresponding normal state resistivity, C_2 is a non-universal constant of order unity, and T_m is the continuous melting (freezing) temperature.

In the Bose-glass model, the scaling behavior for the resistivity is:

$$\rho \approx C|T - T_{BG}|^s \tag{5.13}$$

where T_{BG} is the Bose-glass transition temperature, $s = \nu_\perp(z-2)$ for the bulk sample and $s = \nu_\perp z$ for confined geometry, C is a constant.

Scaling laws are valid sufficiently near to the phase transition. The range of validity of any fit is confined to the lowest resistance region below the *"knees"*, at temperatures

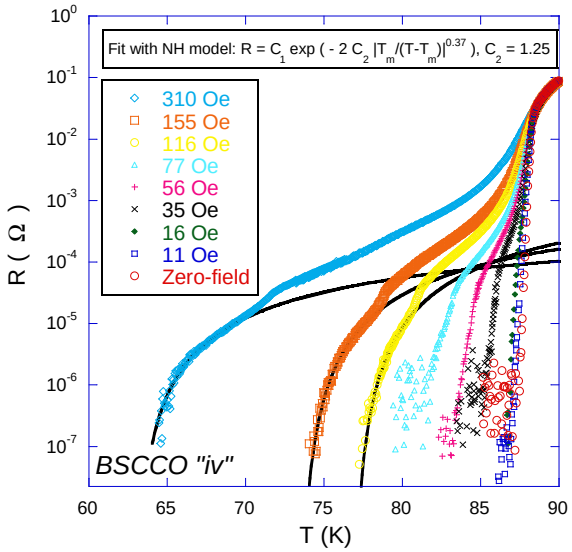

$H_{//c}$ (Oe)	T_m (K)	C_1
310	62.66	3.10×10^{-3}
155	73.25	1.22×10^{-2}
116	76.63	2.42×10^{-2}

Figure 5.29: Halperin-Nelson fit for the sample *BSCCO "iv"* (channels only) according to Equation (5.12). The right-hand panel shows the fit parameters. C_2 is set to a common value: $C_2 = 1.25$ for all the fits.

at which vortex flow is shear flow. We compare with the Nelson-Halperin model (two-dimensional melting by dislocation unbinding) first and then with the Bose-glass model (three-dimensional).

5.4.1 Comparison with the Nelson-Halperin model

Remarkably, almost all the resistivity data for different types of confinement (*BSCCO "iv"*, *BSCCO "24-4"*, and *BSCCO "10G"*) can be fitted well with Equation (5.12) which results from the two-dimensional melting theory. More than two decades can be fitted by Equation (5.12). We find that the exponent 0.37 in Equation (5.12), which is characteristic of continuous melting for triangular lattices, is not strictly required to fit the data. In fact, any exponent value in the interval $0.20 \sim 0.65$ can equally fit our resistivity data and yield reasonable results, namely, the melting temperature T_m.

In $Bi_2Sr_2CaCu_2O_8$, for a certain temperature regime, the interlayer coupling is extremely weak. The layers may act approximately independently. It was theoretically proposed that the decoupling takes place simultaneously with the melting transition [126]. In this scenario, vortex lines lose their line integrity and dissociate into uncorrelated vortex pancakes in the *CuO* planes [127].

At very low fields, a nonlinear resistive behavior is observed in our *BSCCO* samples. Figure 5.32 shows this behavior for the sample *BSCCO "iv"* under various magnetic fields below 56 Oe. The arrows T_{NL} in Figure 5.32 separate a linear-resistance regime and a

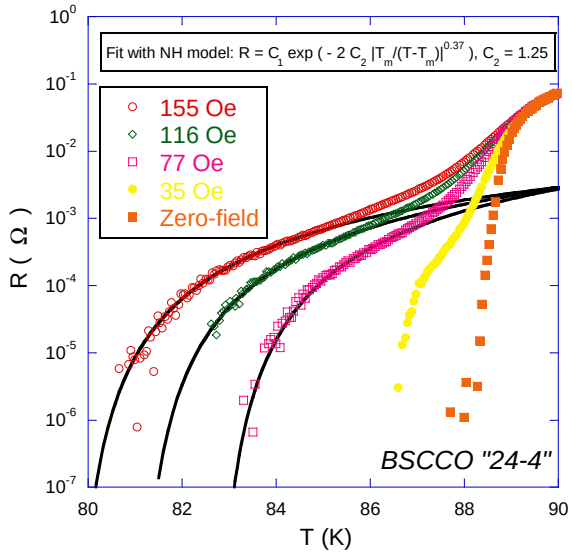

$H_{//c}$ (Oe)	T_m (K)	C_1
155	79.60	0.585
116	80.92	0.762
77	82.59	1.216

Figure 5.30: Halperin-Nelson fit for the sample *BSCCO "24-4"* (channels containing columnar defects of B_ϕ =10 G) according to Equation (5.12). The right-hand panel shows the fit parameters. C_2 is set to a common value: C_2 = 1.25 for all the fits.

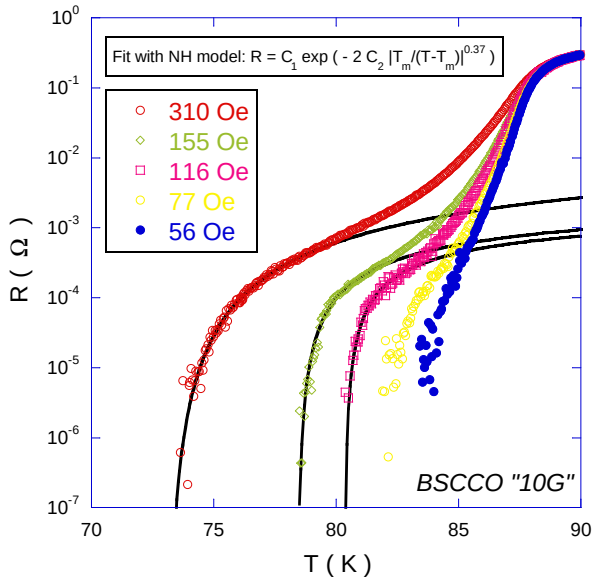

$H_{//c}$ (Oe)	T_m (K)	C_1	C_2
310	72.96	1.21×10^{-1}	1.11
155	78.38	7.66×10^{-3}	0.52
116	80.30	4.59×10^{-3}	0.41

Figure 5.31: Halperin-Nelson fit for the sample *BSCCO "10G"* (homogenously irradiated, B_ϕ = 10 G) according to Equation (5.12). The right-hand panel shows the fit parameters. C_2 takes different values, but remains on the order of unity.

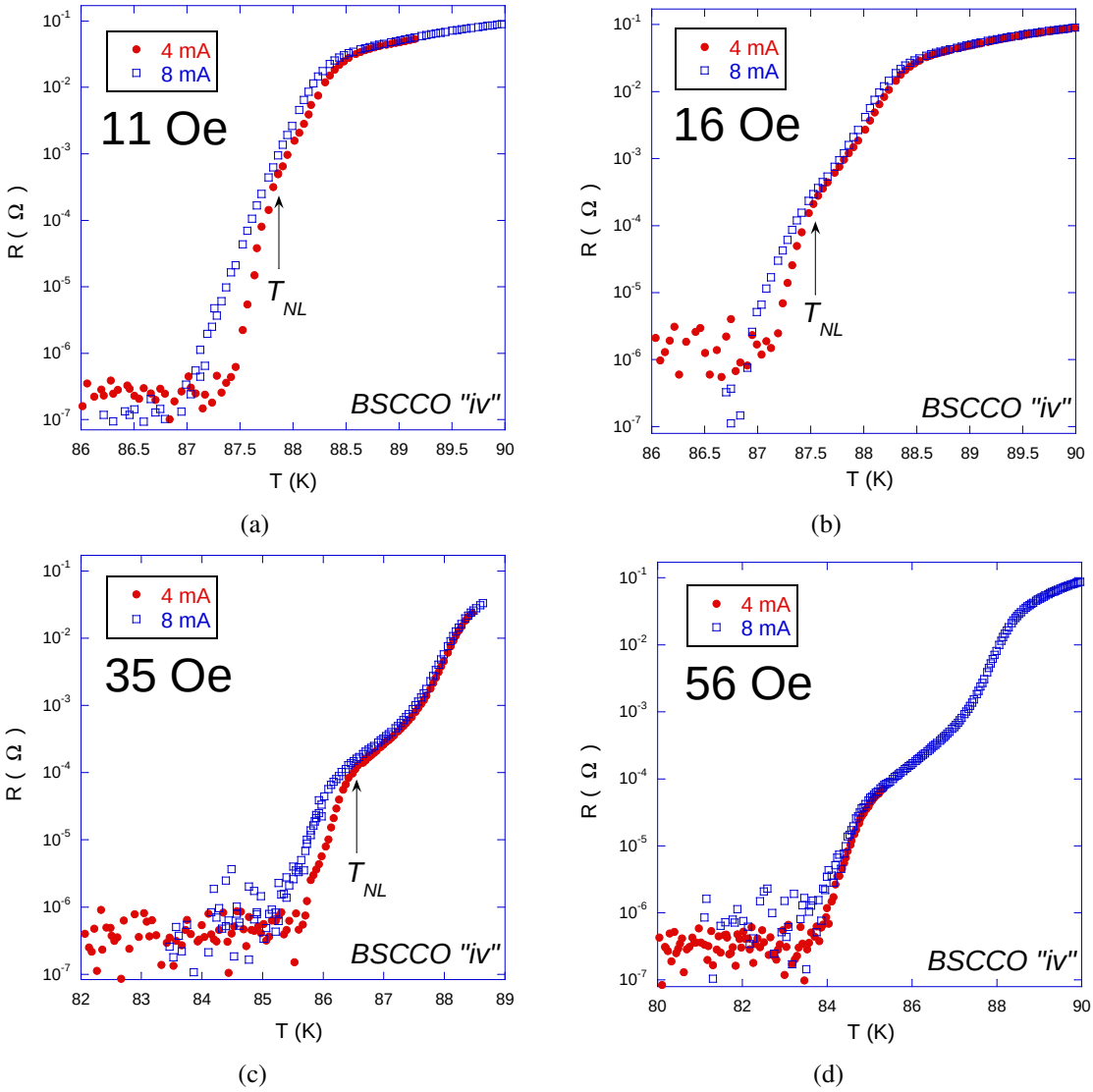

Figure 5.32: Onset of nonlinear resistivity at small fields in *BSCCO "iv"* crystal (channels only). (a) $H_{//c}$ = 11 Oe. (b) $H_{//c}$ = 16 Oe. (c) $H_{//c}$ = 35 Oe. (d) $H_{//c}$ = 56 Oe.

nonlinear-resistance regime. It is often considered that the resistance changes its behavior at the first-order transition (FOT), i.e., vortex liquid-lattice transition. In the liquid state, the resistance is linear; and in the solid state, the resistance is nonlinear. We found that the values of T_{NL} are much higher than the commonly reported FOT temperature for an optimally doped single crystal $Bi_2Sr_2CaCu_2O_8$ [24], [128]. Moreover, if the FOT is the origin of this nonlinear behavior reported in Figure 5.32, it is unlikely that this behavior is suddenly strongly weakened at 56 Oe (see Figure 5.32 (d)). We now investigate whether this corresponds to a continuous two-dimensional melting transition by performing *I-V*

characterizations.

According to the two-dimensional melting theory mediated by the separation of the vortex dislocation pairs, the unbinding of the vortex dislocation pairs under a driving current leads to a power-law *V-I* characteristic: $V \sim I^a$, where the exponent a has the simple form $a(T) = 1 + 2T_{KT}/T$ (a has a $\sqrt{T_{KT} - T}$ behavior close to T_{KT}) [129], [130]. For $T > T_{KT}$, the unbound pairs can be thermally excited without a driving current, the *V-I* behavior is linear. Thus a universal jump in the exponent $a = 1$ to $a = 3$ is expected when one passes through T_{KT}.

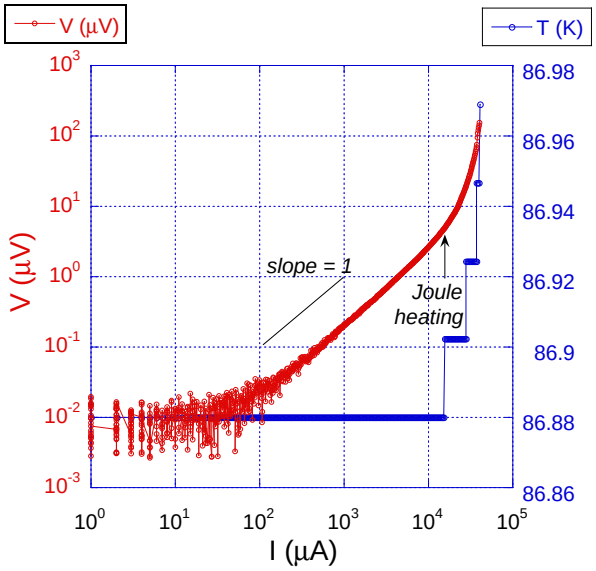

Figure 5.33: To avoid Joule heating, the applied transport current should not exceed 10 mA. Experiment performed on the sample *BSCCO "iv"* at T = 86.88 K, $H_{//c}$ = 35 Oe. The discontinuous jump of the measured temperature is an artifact and is due to the resolution of the temperature sensor and Lakeshore 331.

In order to avoid Joule heating, the maximum current that we were allowed to apply to our samples was 10 mA (see Figure 5.33). In the low current region, due to the thermal noise and the nanovoltmeter resolution, the nonlinear *I-V* characterization performed on our samples was rather rudimental. Our preliminary results of *I-V* characterization (see Figure 5.34) show a jump for the exponent a to 3 in a narrow window around 86 K. Similar results are found in [124] and is explained as a sharp reduction in interplanar coupling between vortex pancakes when the temperature passes through the melting temperature [124]. While it was reported that the vortex correlation along the *c-axis* were amplified after the introduction of columnar defects [131], [132].

Our resistivity data at fields above 77 Oe always lie in the linear-resistance regime, i.e., the vortex system is always in its liquid phase until the sensitivity limit of current

set-up[5]. So, one cannot conclude that a continuous two-dimensional melting (freezing) transition really takes place simply because a good fit of the decreasing resistivity and the scaling law given by Equation (5.12) is found.

Even if the two-dimensional melting scenario cannot be denied in *BSCCO "iv"* by the above *I-V* characterization, as a matter of fact, the surface barrier effect provides a more pertinent explanation for the above observed nonlinear behavior since the two-dimensional melting cannot explain the suddenly strongly weakened nonlinear behavior for fields above 56 Oe either.

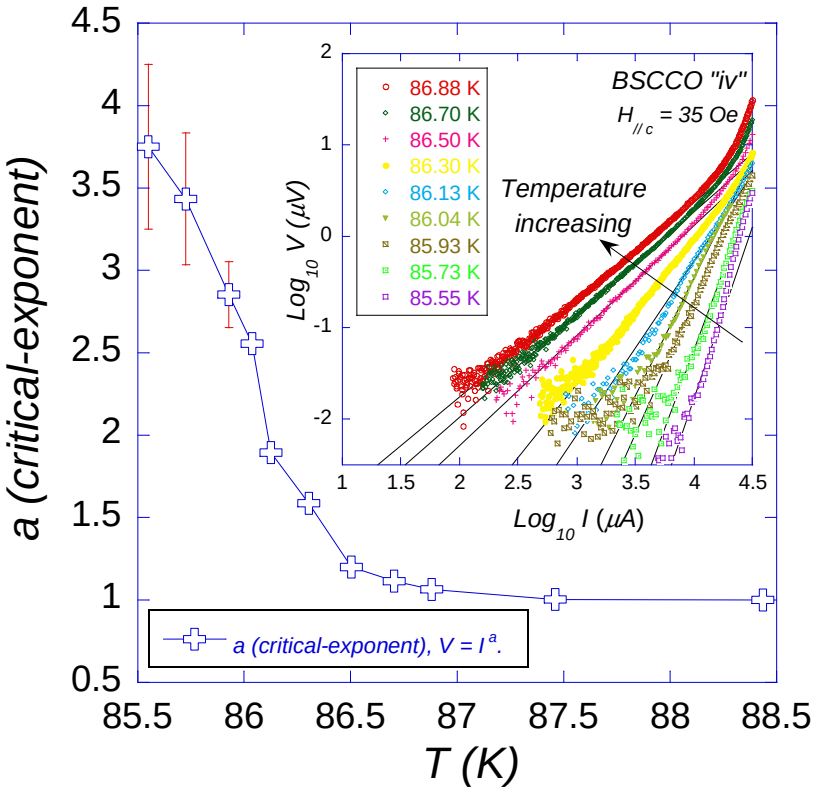

Figure 5.34: Measured critical-exponent as a function of the temperature under a field of $H_{//c}$ = 35 Oe, for the crystal *BSCCO "iv"* (channels only). Inset: I-V characteristics of *BSCCO "iv"* under the same field ($H_{//c}$ = 35 Oe). From the left to the right the data were obtained at the following temperatures: 86.88 K, 86.70 K, 86.50 K, 86.30 K, 86.13 K, 86.04 K, 85.93 K, 85.73 K, 85.55 K. The solid lines are the fits to the data according to the nonlinear relation $V \sim I^a$.

The surface barrier can also introduce a strong nonlinear resistance in the vortex liquid state as we have already seen in the section 5.1.6, the arrows T_{NL} thus separate in fact a uniform flow (high temperature part) and a surface barrier current flow (low temperature

[5] The resistance could be resolved to 10^{-7} Ω with an applied current of 8 mA, which corresponds to a voltage signal of 1 nV.

part) [18], [117]. The heavily irradiated pads and walls have a lowered T_c. At higher temperatures near T_c (see Figure 5.13 (b) (c)), the heavily irradiated part is in the normal state. The magnetic field penetrates these regions and a normal-superconducting interface forms. Since the pads for current injection are located at this interface, the surface barrier effect is significant for the vortex motion in the high temperature regime near T_c. When the temperature is lowered (more explicitly, below 85 K), this normal-superconducting interface disappears and bulk pinning advances towards surface pinning. The vortex motion is then dominated by the bulk pinning and the nonlinear resistance behavior thus disappears. It is reported that the surface barrier can be suppressed when a sufficiently large field (of the order 50 Oe) is applied to a *BSCCO* single crystal where correlated defects are presented [133]. From Figure 5.32, the surface barrier is suppressed for a field around 56 Oe for the *BSCCO "iv"*.

5.4.2 Comparison with Bose-glass model

To investigate the power law in Equation (5.13) experimentally, one usually calculates the inverted logarithmic derivative $(\delta \log R/\delta T)^{-1}$, which should be proportional to $T - T_{BG}$ with a slope of $1/s$. This method is widely used to investigate the power law behavior at Tesla fields. By extrapolating $(\delta \log R/\delta T)^{-1}$ to zero resistivity, one finds T_{BG}. When applying this method to the resistivity data under relatively low magnetic fields, of the present study, one can compare the temperature dependence of the resistivity with scaling laws only when the vortex shear flow is realized; Unfortunately, the data of $(\delta \log R/\delta T)^{-1}$ is very noisy in this region and it is rather difficult to obtain the right value for the slope $1/s$. This is illustrated in Figure 5.35.

Due to the above reason, the following fits are obtained directly from resistivity data compared to Equation (5.13). Whenever possible, the exponent s is fixed so that a model with three parameters (T_{BG}, s, $\mathcal{C}$) reduces to a two-parameter fit. The fits shown in Figures 5.36, 5.37, and 5.38 yield reasonable "Bose-glass transition" temperatures and for a given sample, the constant $\mathcal{C}$ does not vary so much at different magnetic fields. We obtain a field-independent exponent s = 1.9 for sample *BSCCO "iv"* and for sample *BSCCO "24-4"*. While for *BSCCO "10G"*, the exponent s is field-dependent.

Following the argument in Ref. [83], for a homogeneously irradiated crystal, as a first order approximation, the fraction of vortices involved in topological defects, ρ_{def}, is $\rho_{def} \approx \mathcal{K}(B_\phi/B)^{1/2}$, where $\mathcal{K}$ is a proportionality constant. The fraction of vortices forming the crystallites surrounded by the contours (rigid matrix), is thus $1 - \rho_{def} \approx 1 - \mathcal{K}(B_\phi/B)^{1/2}$. With increasing field, the fraction of vortices confined in the rigid matrix increases. In the case of channel confined structure, such as those in *BSCCO "iv"* and *BSCCO "24-4"*, the fraction of confined vortices in the channels remains constant upon changes of the field since the strong pinning walls do not admit vortices in the range of the field of this study (much lower than the matching field of 0.2 Tesla). This may provide

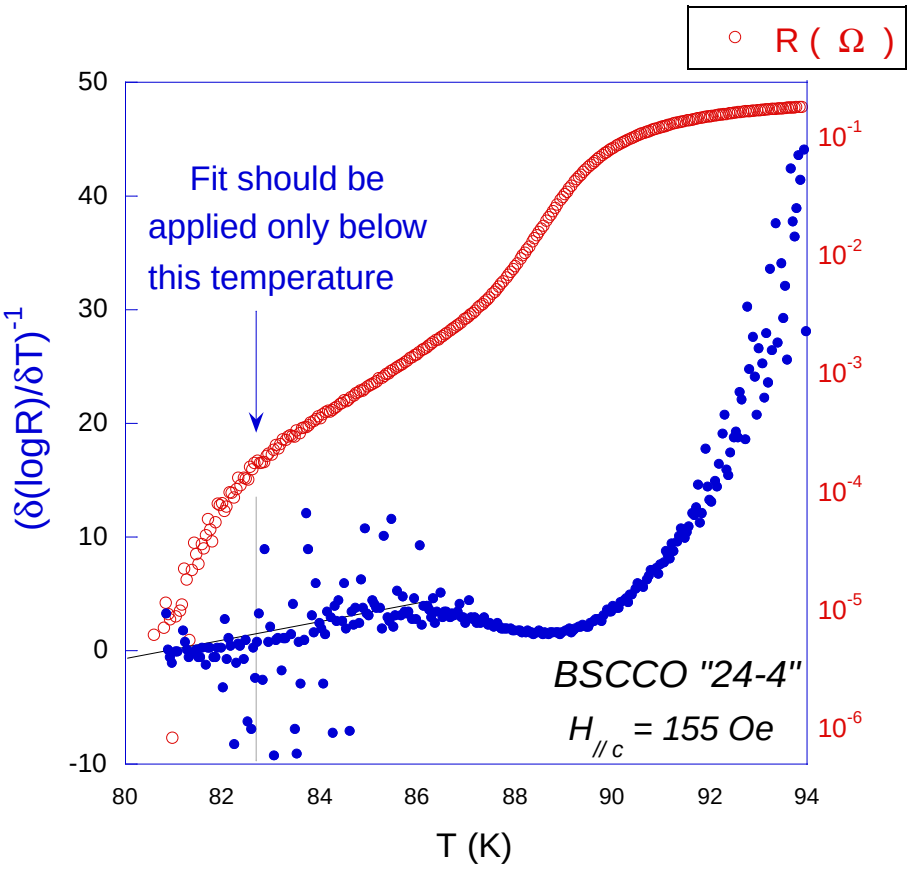

Figure 5.35: Illustration of the inverted logarithmic derivative $(\delta \log R/\delta T)^{-1}$ as a function of the temperature. The resistance curve is also plotted on the same graph for comparison.

an explanation for the field-dependence of the exponent s found in sample *BSCCO "10G"* contrary to the unique s found in sample *BSCCO "iv"* and in sample *BSCCO "24-4"*. If one takes the average value 1.2 for the exponent s as the bulk result (unconfined medium), compared to $s = 1.9$ found for the channel confined medium, one finds $\nu_\perp \approx 0.35$, $z \approx 5.40$. The prediction made by Marchetti and Nelson [109], [32] is thus roughly verified.

Since in *BSCCO "iv"*, the channels are free of any columnar defects, the Bose-glass model is a priori not justified to describe the scaling law in this sample. Combining all the analysis above, we suggest that a good fit between the experimental resistivity data and different kinds of the scaling laws, notably the Bose-glass scaling law, may be resulted from a confinement effect. The unique exponent $s \approx 1.9 \pm 0.2$ found on sample *BSCCO "iv"* and on sample *BSCCO "24-4"* may be only a characteristic of the confinement effect due to the 20-μm channel. In the *polycrystallite* crystal *BSCCO "10G"*, the vortex is confined in the contours (rigid matrix) and the degree of the confinement is field-dependent

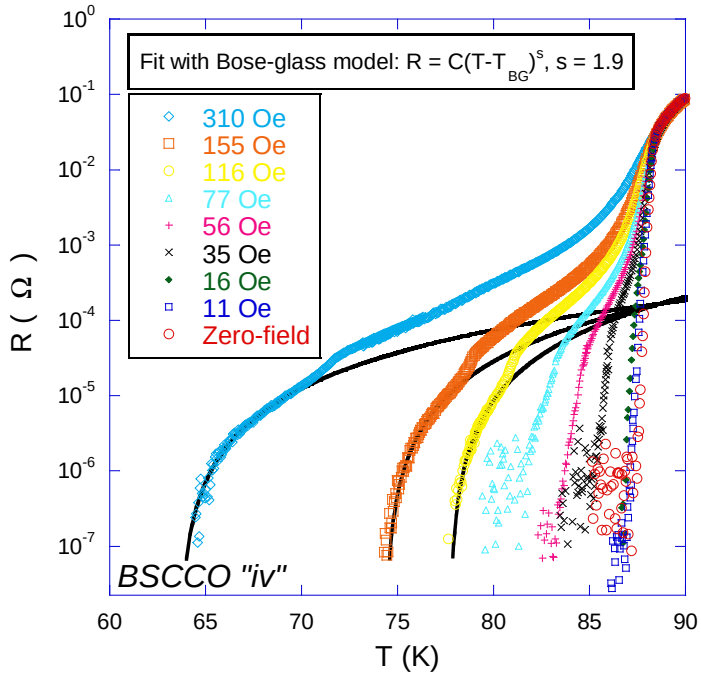

$H_{//c}$ (Oe)	T_{BG} (K)	C
310	63.59	3.66×10^{-7}
155	74.35	1.06×10^{-6}
116	77.70	1.76×10^{-6}

Figure 5.36: "Bose-glass fit" (There are no columnar defects in the channels in this sample) for the resistivity data of *BSCCO "iv"* (channels only) according to Equation (5.13). The right-hand panel shows the fit parameters. s is set to a common value: s = 1.9 for different fields.

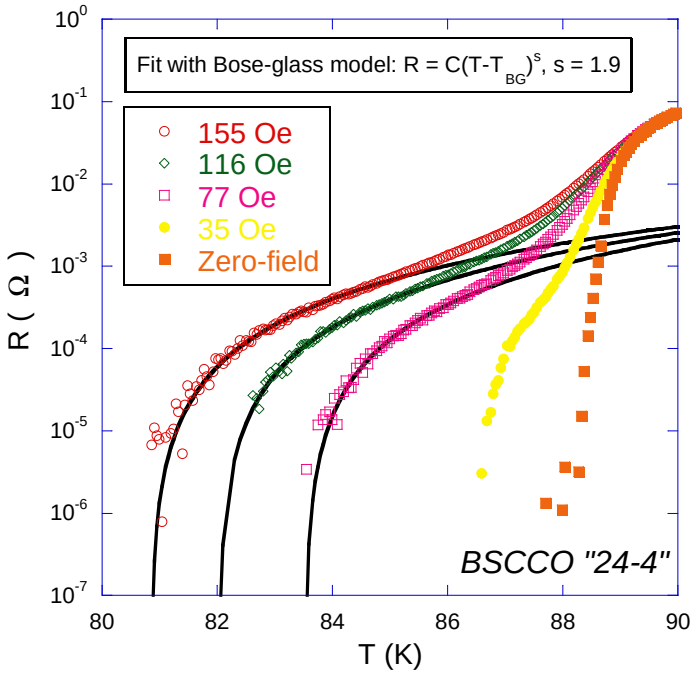

$H_{//c}$ (Oe)	T_{BG} (K)	C
155	80.84	4.50×10^{-5}
116	82.02	4.93×10^{-5}
77	83.52	6.07×10^{-5}

Figure 5.37: Bose-glass fit for the resistivity data of *BSCCO "24-4"* (channels containing columnar defects of $B_\phi = 10$ G) according to Equation (5.13). The right-hand panel shows the fit parameters. s is set to a common value: $s = 1.9$ for different fields.

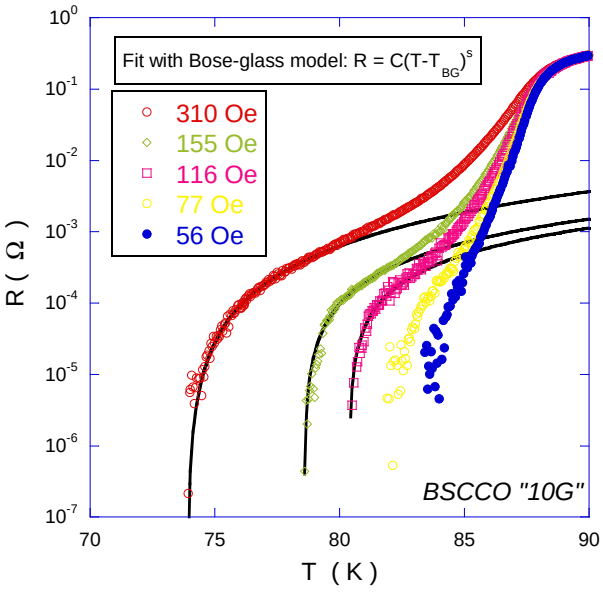

$H_{//c}$ (Oe)	T_{BG} (K)	C	s
310	73.91	2.38×10^{-5}	1.81
155	78.57	6.05×10^{-5}	1.32
116	80.39	8.00×10^{-5}	1.17

Figure 5.38: Bose-glass fit for the resistivity data of *BSCCO "10G"* (homogenously irradiated, $B_\phi = 10$ G) according to Equation (5.13). The right-hand panel shows the fit parameters. We remark that s takes different values for different fields.

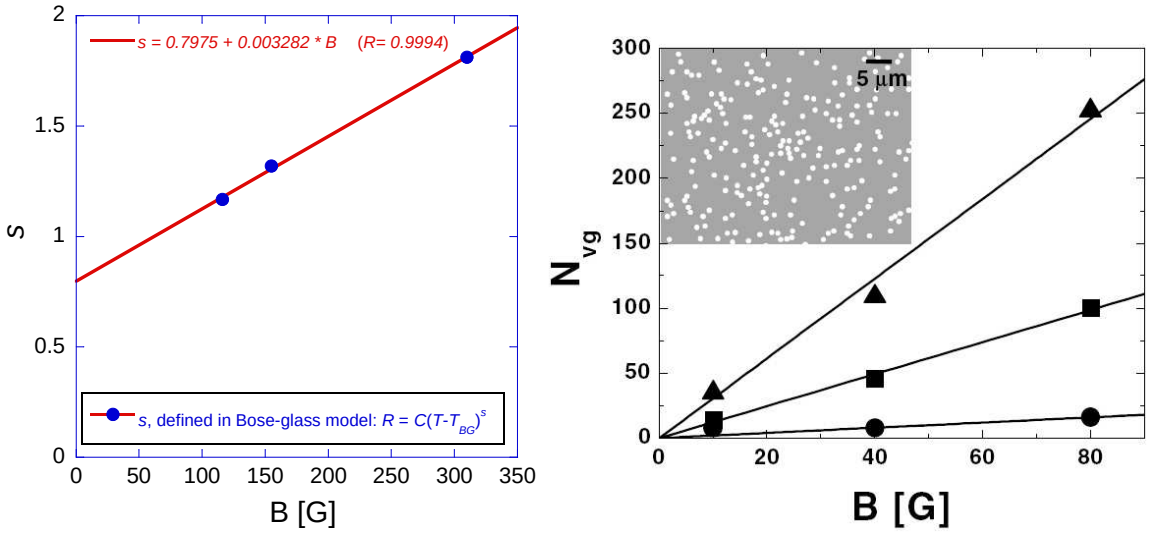

(a) (b)

Figure 5.39: (a) Field-dependence of the exponent s in the Bose-glass model for the sample *BSCCO "10G"* which is homogenously irradiated with a dose of B_ϕ = 10 G. The solid line is a linear fit to this field-dependence relation. (b) Number of vortices within the largest (triangles), the average (squares), and the smallest (circles) grains as a function of B for B_ϕ = 10 G. Inset: distribution of columnar defects in mica. Figure from Ref. [83].

which yields a field-dependent exponent value s (see Figure 5.39).

In the lower range field in this study, the first order transition line exists and lies below the "Bose-glass transition" lines obtained from the fits for the three samples (*BSCCO "iv"*, *BSCCO "24-4"* and *BSCCO "10G"*) (see Figure 5.40). Doubts still remain concerning whether the region below the so-called Bose-glass lines is a Bose-glass phase or simply a confined liquid phase with a very small linear resistance (beyond the resolution of the actual experimental set-up in this study).

The DMO images taken at the relevant temperature and field regime show that the irradiated pads and walls present a much higher critical current density than that of the sample edges, the surface barrier effect should not play an important role on the vortex motion in the temperature and field range under consideration. The absence of nonlinear resistance in the vortex liquid state in this temperature and field regime strongly supports the above argument. The properties probed by our transport measurements on the samples with the irradiated pattern correspond to the bulk properties of the vortex system. It is thus highly desirable to investigate the scaling behavior on the samples with narrower channel structures. Explicitly, if one obtains different values for the exponent s in samples with channel confined structure of different channel widths (for example 10 μm, 5 μm), then the accordance between the experimental resistivity data and the scaling laws does not correspond to any phase transitions but only describe a confinement effect which mimics

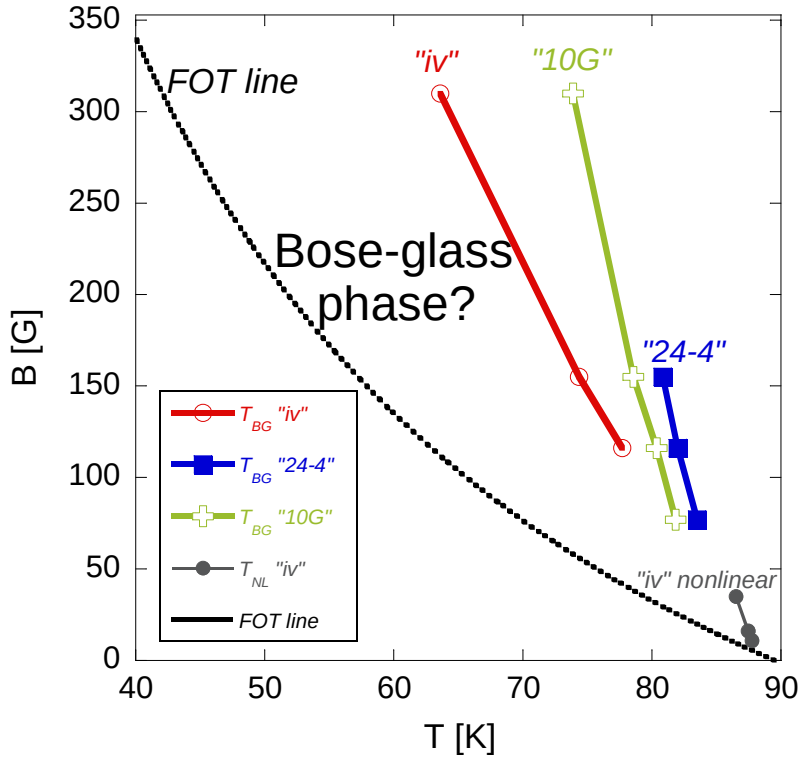

Figure 5.40: Phase diagram of $Bi_2Sr_2CaCu_2O_8$. The Bose-glass lines are obtained from the fit results of T_{BG} according to Equation (5.13). The FOT line is traced by the Equation $B_m(T) = B_0(T_c - T)/T$ with B_0 = 275 G, $T_c \approx$ 89.5 K which is in good agreement with the experimental data for optimally doped $Bi_2Sr_2CaCu_2O_8$ single crystals [24], [128].

that in a vortex liquid to disordered vortex solid transition. Unluckily the irradiation experiments aiming to obtain channels of width less than 20 μm failed in our work. If one obtains the same value for $s \approx 1.9 \pm 0.2$, then the *I-V* characterizations (using pulsed current in order to avoid the Joule heating) are pursued for the investigation of the vortex system at its Bose-glass state.

Chapter 6

Conclusions

In this thesis, two experimental techniques are combined in order to study vortex dynamics in high temperature superconductors: magneto-optical imaging and transport measurements. These methods are applied to the characterization of high temperature superconducting single crystals, notably $Bi_2Sr_2CaCu_2O_8$. Magneto-optical imaging is used to investigate the distribution of flux density and screening currents in superconductors to which orthogonal magnetic fields are applied, in the configuration of a Nuclear Magnetic Resonance experiment. Finally, the shear properties of the vortex liquid in $Bi_2Sr_2CaCu_2O_8$ single crystals are studied on approaching the vortex liquid-to-solid transition. In both cases, magneto-optical imaging is an invaluable tool to identify the path of current flow, and thereby the physical mechanism at the origin of the electrodynamic response of the superconductor, and at the origin of dissipation.

In the latter experiments, the shear viscosity of the vortex system can be measured directly by introducing an artificial structure in $Bi_2Sr_2CaCu_2O_8$ single crystals that are otherwise free of any macroscopic defects. Strongly pinning walls, introduced by heavy ion irradiation through a 30 μm thick Ni mask, define weakly pinning channels through which the vortex ensemble is forced to flow. An additional, essential ingredient of the experiment is the inclusion of heavy-ion irradiated contact pads directly adjacent to the channel structure, and far removed from the crystal boundaries. By injecting the transport current through these irradiated pads, one forces the transport current to flow through the bulk; shear flow of the vortex ensemble then takes place through the channels. The shear viscosity of the vortices in the bulk can then be probed by a standard resistivity measurement. The signatures of shear flow are clearly noticeable in the resistance curves. The nature of the various features of the resistivity curves can be unambiguously identified by comparing them to magneto-optical images of the magnetic field distribution created by a transport current.

By comparing our results with the former work performed by H. Pastoriza and P. H. Kes [72] and the work of D. T. Fuchs et al. [117] in $Bi_2Sr_2CaCu_2O_8$ single crystals, we conclude that the vortex properties obtained in [72] correspond to the response of the

surface of the $Bi_2Sr_2CaCu_2O_8$ crystal. Our work probes the bulk vortex properties; as a consequence, we observed no sharp jump of the resistance within the resolution limit (10^{-7} Ω) of our set-up.

We have compared our resistance data with two different models: two-dimensional (2D) Nelson-Halperin melting model and the three-dimensional (3D) Bose-glass model. Both the 2D and 3D models well describe the experimental resistance data as one approaches zero-resistance. There are several ways to understand this. First, in layered $Bi_2Sr_2CaCu_2O_8$ single crystals, the interaction between the CuO_2 planes is very weak in the liquid vortex state. The vortex system might thus be considered as an ensemble 2D vortices at the crystal surface; correspondingly, vortex lattice defects in layered $Bi_2Sr_2CaCu_2O_8$ single crystals resemble 2D defects. However, the fact that the irradiated structure is defined through the entire sample thickness means that the current is also distributed over the whole thickness: a plausible alternative is therefore that the vortex lattice flows as an ensemble of rectilinear lines, and that vortex lattice defects (edge dislocations) extend from crystal top to crystal bottom.

As we investigate the 3D glass model, one remarks that the obtained parameters within the framework of the Bose-glass model correspond to the predictions of Marchetti and Nelson [109]: a higher value of the critical exponent for confined vortex matter. It is also noteworthy that glass-like features of the resistivity are observed, even though one is in the vicinity of a first order transition of the vortex lattice. The fact that the resistance data, even in the low fields investigated, can be well fitted by the power scaling law derived from glass model may be attributed to the fact that plastic vortex motion in confined medium mimics the vortex liquid to vortex glass transition. This point of view finds an analogy in the recently reported shear-induced solid-to-fluid transition in soft glassy materials such as foams, emulsions, gels, or colloidal suspensions.

There are various opportunities for the continuation of this work. Magneto-optical imaging is a powerful experimental tool to study vortex dynamics in superconductors. However, the relation between the light intensity in a magneto-optical image and the magnetic flux intensity (B-field) is quadratic. We find that in the normally used differential imaging procedure [36], the signal is the true differential signal, convoluted with the direct signal. If one incorporates a light polarization modulation procedure into the image acquisition step, one can obtain a linear-in-B-field mapping, rather than $(kB+\alpha)^2$. By performing a differential operation on the images of B-field, one would obtain true differential signal, e.g., $\frac{dB}{dH}$, $\frac{dB}{dT}$. It would be very interesting to study the flux density pattern at vortex lattice melting further in the presence of disorder with this new differential magneto-optical imaging technique and reconsider the correlation between the melting propagation and the resistivity change revealed by simultaneous magneto-optical imaging and transport measurements. The first study of this correlation is reported in the thesis work of A. Soibel [38], while this study only considered the situation where bulk pinning

is absent.

We point out that the interpretation of differential magneto-optical imaging with an in-plane field modulation presented in the fourth chapter of this thesis relies on the hypothesis that the vortex responses under an in-plane field and a perpendicular field are independent. This hypothesis needs more careful examination and the interpretation for differential imaging with an in-plane field modulation could be more complicated.

Concerning the studies of confined vortex matter, if one succeeds in making new masks with narrower channel widths, then comparisons of resistivity data with different channel widths could be achieved and the size effects could be studied.

Appendix A: Units, Notations, and Conventions

A-1 Units

The two systems of electromagnetic units in most common use today are the SI and cgs-Gaussian systems. The SI system is convenient in engineering applications and the cgs-Gaussian system is more suitable for microscopic problems. This thesis is written with the SI system throughout except for a few formulas that are explicitly quoted in cgs-Gaussian system for convenience.

A-2 Definitions to study magnetic materials

The magnetic fields of magnets or generated by currents are characterized by the magnetic induction or flux density **B**, with Tesla as its unit in SI system and Gauss as its unit in cgs-Gaussian system (1 Tesla = 10^4 Gauss). When one applies a magnetic field on magnetic materials which themselves contribute internal magnetic field, to distinguish the part of the field that comes from the external applied field and the part from the material itself, one defines another magnetic field quantity, which is independent of the material's magnetic response, called the *magnetic field strength* and designated by **H**, through the following relation:

$$\mathbf{H} \equiv \mathbf{B}_0/\mu_0 \equiv \mathbf{B}/\mu_0 - \mathbf{M} \tag{A-1}$$

or

$$\mathbf{B} = \mu_0(\mathbf{H} + \mathbf{M}) \tag{A-2}$$

where **M** is called the *magnetization density* (magnetic moment per unit volume) of the material, μ_0 is a universal constant called the *magnetic permeability of free space* and $\mu_0 \equiv 4\pi \times 10^{-7}$ H/m in SI system[1]. **H** and **M** have the the same units, A/m, in SI system.

In the special case where the magnetization density is proportional to the external applied magnetic field, one can rewrite Equation (A-2) as $\mathbf{B} = \mu\mathbf{H}$, where μ is defined as

[1] In vacuum, $\mathbf{B} = \mu_0\mathbf{H}$. Its counterpart in cgs-Gaussian system is $\mathbf{B} = \mathbf{H}$. Equation (A-2) in cgs-Gaussian system is: $\mathbf{B} = \mathbf{H} + 4\pi\mathbf{M}$.

the *magnetic permeability* of the material. The ratio of the magnetic permeability of the material μ to magnetic permeability of free space μ_0, defined by $\mu_r \equiv \mu/\mu_0$, is called the *relative permeability* of the material.

For paramagnetic substances, μ_r is greater than unity; For diamagnetic substances, μ_r is smaller than unity; For ferromagnetic substances, there is no unique relation between $\mathbf{B}$ and $\mathbf{H}$. Another quantity, called the *magnetic susceptibility*, defined as $\chi \equiv \mu_r - 1$, specifies how much the relative permeability differs from unity.

A-3 Convention employed to describe magnetic response of superconductors

Equation (A-2) is a constitutive law for material. To model the behavior of superconductors, one can use two equivalent approaches as discussed in Ref. [8] and listed in Table (A-1): in the so-called "Method I", $\mathbf{M} = 0$ in the constitutive Equation (A-2) and the supercurrent $\mathbf{j}_s$ contains two terms: the external applied current $\mathbf{j}_{s,app}$ and the induced supercurrent $\mathbf{j}_{s,ind}$ due to the application of external magnetic field; while in the so-called "Method II", $\mathbf{M} \neq 0$ and the supercurrent $\mathbf{j}_s$ only refers to the external applied current $\mathbf{j}_{s,app}$. The constitutive relations are only to model the behavior of the material and are not fundamental. The two modeling methods are related through the following relation: curl $\mathbf{M} = \mathbf{j}_{s,ind}$ so that all the experimentally observed phenomena can be consistently described by both methods.

Quantity	Method I ($\mathbf{M} = 0$)	Method II ($\mathbf{M} \neq 0$)
Supercurrent	$\mathbf{j}_s^I = \mathbf{j}_{s,app} + \mathbf{j}_{s,ind}$	$\mathbf{j}_s^{II} = \mathbf{j}_{s,app}$
Magnetic field	$\mathbf{H}^I = \mathbf{B}/\mu_0$	$\mathbf{H}^{II} = \mathbf{B}/\mu_0 - \mathbf{M}$

Table A-1: Comparison between two modeling approaches.

We choose the approach "Method I" in this thesis to describe magnetic response of superconductors. The difference between the measured magnetic flux density $\mathbf{B}$ and the applied external magnetic field $\mu_0\mathbf{H}_a$ is defined as the *self-field*, designated by $\mu_0\mathbf{H}_s$, i.e., $\mu_0\mathbf{H}_s \equiv \mathbf{B} - \mu_0\mathbf{H}_a$. If one defines $\mathbf{B}_a \equiv \mu_0\mathbf{H}_a$ and $\mathbf{B}_s \equiv \mu_0\mathbf{H}_s$, then one has: $\mathbf{B} = \mathbf{B}_a + \mathbf{B}_s$. The term *self-field* $\mathbf{H}_s$ employed in this thesis corresponds to the term "*magnetization*" when one uses the second approach ("Method II") to describe magnetic behavior of superconductors.

Notations and conventions for magnetic and electric fields on microscopic length scale

One uses $\mathbf{h}(\mathbf{r})$ to denote the local value of the magnetic induction or flux density, which typically varies on the scale of the penetration depth λ. One reserves the use of $\mathbf{B}$ to denote the value of $\mathbf{h}(\mathbf{r})$ averaged over such microscopic lengths but still capable of varying smoothly over the macroscopic dimensions of the sample[2]. For notation symmetry, one defines a microscopically varying electric field $\mathbf{e}(\mathbf{r})$, whose spatial average is $\mathbf{E}$. The macroscopic averages $\mathbf{B}$ and $\mathbf{E}$ satisfy the Maxwell's equations, which are listed below (expressed with SI units):

$$\begin{aligned} curl\,\mathbf{E} &= -\frac{\partial \mathbf{B}}{\partial t}, \\ curl\,\mathbf{B} &= \mu_0 \mathbf{j} + \mu_0 \varepsilon_0 \frac{\partial \mathbf{E}}{\partial t}, \\ div\,\mathbf{E} &= \frac{\rho}{\varepsilon_0}, \\ div\,\mathbf{B} &= 0. \end{aligned}$$

where $\mathbf{j}$ is the total current density[3]; ρ is the total charge density (including polarization charges); μ_0 is a universal constant called the *magnetic permeability of free space* and $\mu_0 \equiv 4\pi \times 10^{-7}$ H/m in SI system; ε_0 is a universal constant called the *permittivity of free space* and $\varepsilon_0 = 1/c^2\mu_0 \approx 8.8542 \times 10^{-12}$ F/m, with c the speed of light in vacuum.

[2] I follow the conventions employed by P. G. De Gennes and M. Tinkham. [3] $\mathbf{j} = \mathbf{j}_c + \mathbf{j}_m + \mathbf{j}_p$, where $\mathbf{j}_c$ is the conduction current density, $\mathbf{j}_m$ is the magnetization current density defined as $\mathbf{j}_m = curl\mathbf{M}$, $\mathbf{j}_p$ is the polarization current density defined as $\mathbf{j}_p = \partial\mathbf{P}/\partial t$, with $\mathbf{P}$ the electric dipole moment per unit volume.

Appendix B: Nuclear Magnetic Resonance and Knight shift

B-1 Nuclear Magnetic Resonance

Nuclear Magnetic Resonance (NMR) provides a powerful tool for the identification and the structure determination of complex molecules. It is possible to use the radiofrequency signals from the nuclei to build up a detailed picture of the three-dimensional structure of an object. A major medical application of NMR is Magnetic Resonance Imaging (MRI), which allows 3D resolution of abnormal growths, configurations, and reactions in the whole body.

The key elements to understand NMR are presented in the following. This simple quantum mechanical description is inspired from C. P. Slichter's book « Principles of magnetic resonance » [134]. A nucleus possesses a total moment μ and a total angular momentum $\hbar\mathbf{I}$. The two vectors are parallel and are related by $\mu = \gamma\hbar\mathbf{I}$, where γ is a scalar called the *gyromagnetic ratio*. The application of a magnetic field $\mathbf{H}$ produces an interaction energy of the nucleus of amount $-\mu\cdot\mathbf{H}$. One has, therefore, a very simple Hamiltonian: $\mathcal{H} = -\mu\cdot\mathbf{H}$. One denotes I_z as the component of $\mathbf{I}$ along the z-direction. Taking the field to be H_0 along the z-direction, one finds $\mathcal{H} = -\gamma\hbar H_0 I_z$. The eigenvalues of this Hamiltonian are multiples $(-\gamma\hbar H_0)$ of the eigenvalues of I_z. Therefore the allowed energies are: $E = -\gamma\hbar H_0 m$, $m = I, I-1, ..., -I$.

In order to detect the presence of such a set of energy levels by spectral absorption measurements, one needs to have an interaction that can cause transition between levels. If one uses an alternating magnetic field of an amplitude H_x^{ac} applied perpendicular to the static field to produce magnetic resonances, one gets a perturbing term in the Hamiltonian of $\mathcal{H}_{pert} = -\gamma\hbar H_x^{ac} I_x \cos\omega t$. To satisfy the conservation of energy, the angular frequency ω satisfies that $\hbar\omega = \Delta E$, where ΔE is the energy difference between the initial and final nuclear Zeeman energies. The operator I_x has matrix elements between states m and m', $(m'|I_x|m)$, which vanish unless $m' = m \pm 1$. Consequently only the transitions between adjacent energy levels are allowed, giving $\hbar\omega = \Delta E = \gamma\hbar H_0$ or $\omega = \gamma H_0$. For example: for the proton ($\gamma = 2.675 \times 10^8\ s^{-1}T^{-1}$) in a magnetic field of 1 Tesla, the resonance frequency is $\nu = 42.58\ MHz$ (a radiofrequency).

B-2 NMR probe of superconductors

B-2.1 NMR Knight shift

One finds that, in a given field H, the frequency ν_m at which nuclear resonance is observed in a metal is higher than the frequency ν_i at which it occurs, for the same nucleus, in an insulator. The ratio $K = (\nu_m - \nu_i)/\nu_i$ is called the Knight shift after its discoverer, and the effect is due to the presence of conduction electrons in the metal [135].

The so-called hyperfine interaction is the magnetic interaction between the magnetic moment $\mathbf{I}$ of the nucleus and the magnetic moment $\mu_\mathbf{e}$ of the electrons [136]. As observed from the nucleus, the interaction is caused by the magnetic field originating from the magnetic moment $\mu_B\mathbf{J}$ of the electrons (here $\mu_B = e\hbar/2m = 9.27 \times 10^{-24}$ J/T is the Bohr magneton). In the presence of electronic density $n \sim |\Psi(0)|^2$, where $\Psi(0)$ denotes the value of the electronic wavefunction at the nucleus, one has

$$U = -\mu \cdot \mu_e |\Psi(0)|^2 \approx 2\gamma\hbar\mu_B |\Psi(0)|^2 \mathbf{I} \cdot \mathbf{J}. \tag{B-1}$$

Here $\mathbf{J} = \mathbf{L} + \mathbf{S}$, $\mathbf{L}$ is the orbital angular momentum and $\mathbf{S}$ is the spin of the electron in units of $\hbar$.

If the electrons are in a state with nonzero orbital angular momentum L, there is an orbital electronic current about the nucleus. But, even if the electrons are in a state of zero angular momentum, there is still a spin current about the nucleus, which gives rise to the so-called contact hyperfine interaction:

$$U_c = -\mu \cdot \mu_e |\Psi(0)|^2 \approx 2\gamma\hbar\mu_B |\Psi(0)|^2 \mathbf{I} \cdot \mathbf{S}. \tag{B-2}$$

The hyperfine constant a is defined by $U = a\mathbf{I} \cdot \mathbf{S}$, compared to Equation (B-2), one thus gets:

$$a \approx 2\gamma\hbar\mu_B |\psi(0)|^2. \tag{B-3}$$

Taking into account this *contact hyperfine interaction*, the interaction energy of the nucleus is

$$\mathcal{H} = -\gamma\hbar H_0 I_z + a < S_z > I_z, \tag{B-4}$$

where the first term is the interaction with the applied magnetic field H_0 and the second is the average hyperfine interaction of the nucleus with the conduction electrons.

The average conduction electron spin $< S_z >$ is related to the Pauli spin susceptibility χ^{spin} of the conduction electrons through M_z (magnetization component along z-direction per unit volume): $M_z = \chi^{spin} H_0$, where $\chi^{spin} = \mu_B^2 N(E_F)/E_F$, here E_F is the Fermi energy and $N(E_F)$ is the density of states at the Fermi surface. This relation is obtained by the application of the Fermi-Dirac distribution to electrons [137]. Let N denote the number

of electrons per unit volume, M_z can also be expressed by $M_z = 2N\mu_B < S_z >$. One thus gets:

$$< S_z >= \frac{\chi^{spin} H_0}{2N\mu_B}. \tag{B-5}$$

If one defines ΔH as $\Delta H \equiv -\frac{a\chi^{spin}}{2N\mu_B\gamma\hbar} \cdot H_0$, the interaction energy can be expressed as:

$$\mathcal{H} = -\gamma\hbar H_0(1 + \frac{\Delta H}{H_0})I_z \tag{B-6}$$

The Knight shift is:

$$K = \frac{\nu_m - \nu_i}{\nu_i} = -\frac{\Delta H}{H_0} = \frac{a\chi^{spin}}{2N\mu_B\gamma\hbar} \tag{B-7}$$

Putting the expression of a in Equation (B-3) into the above Equation (B-7), one gets:

$$K \approx \frac{\chi^{spin} < |\psi(0)|^2 >_{av}}{N} \tag{B-8}$$

The Knight shift is therefore a measure of the Pauli spin susceptibility and so also a measure of the density of states at the Fermi surface.

B-2.2 Knight shift measurements in superconductors

In superconductors, for the spin-singlet pairing, the ratio of the spin susceptibility of the Cooper pair χ_s to that of the normal state χ_n is given by [41]:

$$\frac{\chi_s}{\chi_n} = -\frac{2}{N_0}\int_0^\infty N_s(E)\frac{\partial f(E)}{\partial E}dE \tag{B-9}$$

where N_0 and $N_s(E)$ are the quasi-particle *Density of States* (*DOS*) in the normal and in the superconducting state, respectively, and $f(E)$ is the Fermi distribution function.

This is just the sort of tool one needs to explore the nature of the superconducting state, since the coherent Cooper pair states are formed at energies near the Fermi energy. Also, since the energy involved in the superconducting transition is small, it is unlikely that the value $\psi(0)$ of the wavefunction of a conduction electron at the position of a nucleus is appreciably affected when the specimen goes superconducting. It would thus be interesting to investigate the Knight shift in a superconductor from above T_c to as close to 0 K as is reachable. In a singlet superconductor, the electrons in the Cooper pairs are bound in spin singlets; they are not polarized at all in the small fields applied in NMR experiments. As a result, the Knight shift or the Pauli spin susceptibility vanishes at zero temperature [138].

For the *s-wave* paring, the DOS is given by $N_s(E)/N_0 = |E|/\sqrt{E^2-\Delta^2}$ (for $|E| > \Delta$) and $N_s = 0$ (for $|E| < \Delta$), in which Δ is a function of T/T_c. Equation (B-9) reduces to the Yosida function $Y(T/T_c)$ [139]. At low T, χ_s decreases exponentially as $exp(-\Delta/k_BT)$ (see Figure B-1 (b), dashed line). In a spin-singlet *d-wave* state, the decay of χ_s is not exponential. The gap symmetry in $YBa_2Cu_4O_8$ compound is $d_{x^2-y^2}$ symmetry and can be modeled as: $\Delta(\mathbf{k}) = \Delta(\phi) = \Delta_0 cos(2\phi)$, where Δ_0 is the maximum gap, ϕ is the angle on the cylindrical Fermi surface of the CuO_2 plane. In the absence of a magnetic field,

$$N_s(E)/N_0 = \frac{1}{2\pi}\int_0^{2\pi} Re[\frac{E}{\sqrt{E^2-\Delta^2(\phi)}}]d\phi = \frac{2}{\pi}\frac{E}{\Delta_0}K(\frac{E}{\Delta_0}), \qquad \text{(B-10)}$$

Here $Re(x)$ means the real part of x and $K(x)$ is the complete elliptic integral. For small $\frac{E}{\Delta_0}$, or when $T < 0.4T_c$, numerical evaluation shows that $N_s(E)$ increases linearly with E [140]. χ_s is proportional to T at low T (see Figure B-1 (b), solid line). As long as the pairing is spin-singlet, χ_s diminishes to zero as $T \to 0$ K. But for triplet superconductors with the parallel spins lying in the plane, the application of a magnetic field in the plane changes the relative numbers of pairs with spin parallel and antiparallel to the field, and the Knight shift is unchanged from its value in the normal state [41] (see Figure B-3).

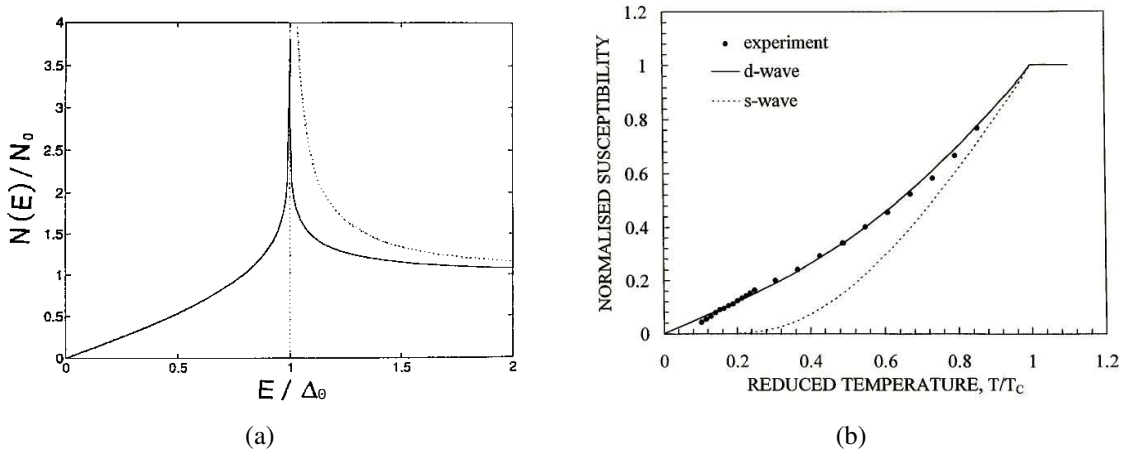

(a) (b)

Figure B-1: (a) Density of states for *s-wave* and *d-wave* superconductors according to Equation (B-10). Dashed line: s-wave; Solid line: d-wave. Figure from Ref. [140]. (b) Normalized spin susceptibility versus reduced temperature for the underdoped high-T_c superconductor, $Gd : YBa_2Cu_4O_8$ (T_c = 82 K). The measurements in [138] confirmed the linear temperature dependence at low temperatures for a *d-wave* superconductor: $Gd : YBa_2Cu_4O_8$. Solid line: Fit to a d-wave coupling model with maximum gap $\Delta_0 = 2.3k_BT_c$; Dashed line: s-wave weak coupling Yosida function. Figure from Ref. [138].

Taking, for example, a *d-wave* superconductor, the supercurrent enhances the effective density of states near the gap nodes, therefore the effective value of χ_s is higher than expected. This is known as the Volovik effect. If one knows the current density distribution $J_s(\mathbf{r})$ in a superconductor, one can estimate the superfluid velocity, and therefore the influence of the Volovik effect on the NMR Knight shift data.

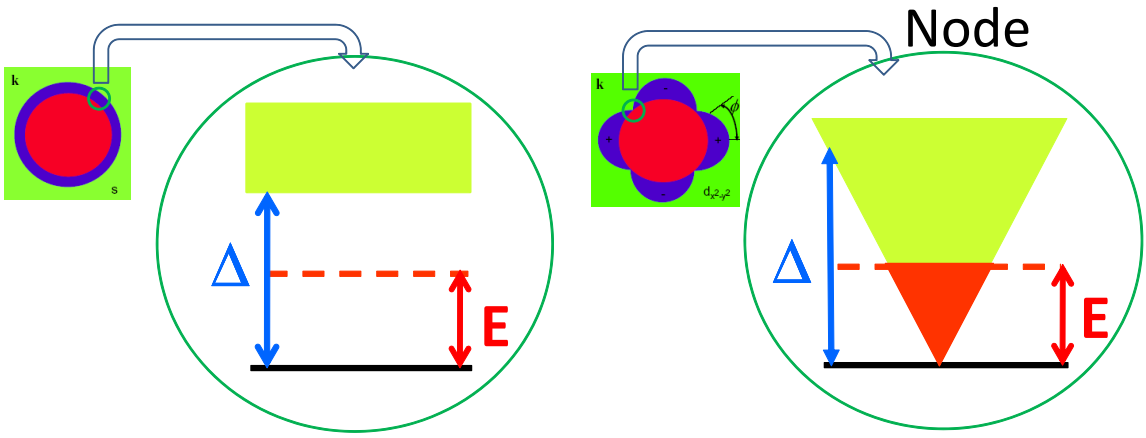

(a) (b)

Figure B-2: (a) *s-wave*: isotropic gap Δ. (b) *d-wave*: anisotropic gap $\Delta = \Delta_0 \cos(2\phi)$.

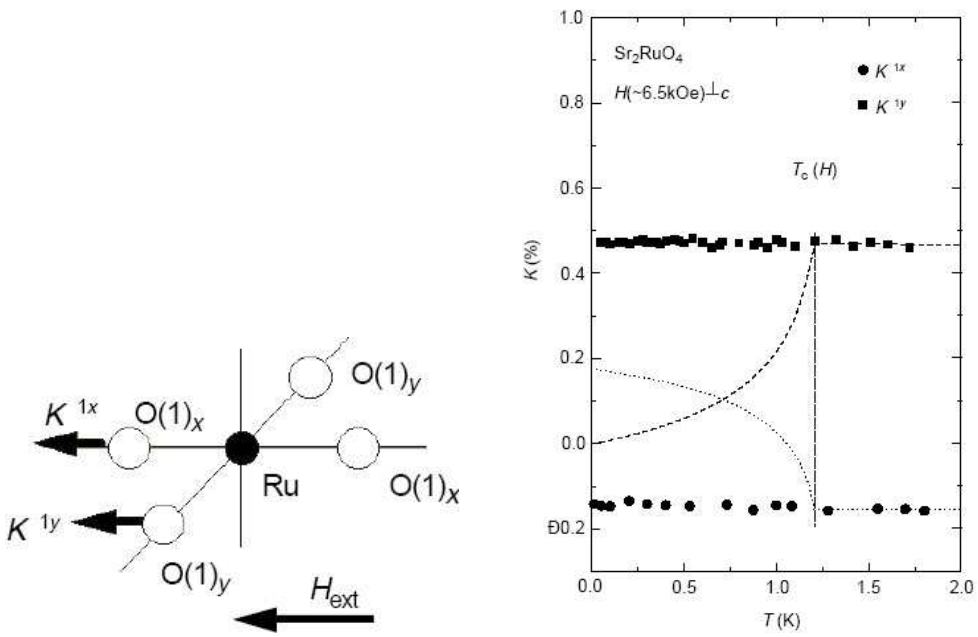

(a) (b)

Figure B-3: Knight shift measured for Sr_2RuO_4 (T_c = 1.4 K) with the field parallel to the *ab* plane. (a) Definition of K^{1x} and K^{1y}. (b) Temperature dependence of K^{1x} and K^{1y} at low temperatures. Broken lines below T_c indicate the calculation for the spin-singlet d-wave state in two dimensions with $d_{x^2-y^2}$ symmetry, using the parameters $\Delta(\phi) = \Delta_0 \cos(2\phi)$ and $2\Delta_0 = 8k_BT_c$ which are compatible with those of $YBa_2Cu_3O_7$. ϕ is the angle on the cylindrical Fermi surface of the CuO_2 plane. Figure from Ref. [41].

Bibliography

[1] H. Kamerlingh Onnes, Leiden Comm. **122b**, 124 (1911).

[2] W. Meissner and R. Ochsenfeld, Naturwiss. **21**, 787 (1933).

[3] J. Bardeen, L. N. Cooper, and J. R. Schrieffer, *Theory of superconductivity*, Phys. Rev. **108**, 1175 (1957).

[4] J. G. Bednorz and K. A. Müller, *Possible high T_c superconductivity in the Ba-La-Cu-O system*, Z. Physik, **64**, 189 (1986).

[5] M. K. Wu, J. R. Ashburn, C. J. Torng, P. H. Hor, R. L. Meng, L. Gao, Z. J. Huang, Y. Q. Wang, and C. W. Chu, *Superconductivity at 93 K in a new mixed-phase Y-Ba-Cu-O compound system at ambient pressure*, Phys. Rev. Lett. **58**, 908 (1987).

[6] H. Maeda, Y. Tanaka, M. Fukutumi, and T. Asano, *A new high-T_c oxide superconductor without a rare earth element*, Jpn. J. Appl. Phys. **27**, L209 (1988).

[7] V. L. Ginzburg and L. D. Landau, Zh. Eksp. Teor. Fiz. **20**, 1064 (1950).

[8] T. P. Orlando and K. A. Delin, *Foundations of Applied Superconductivity*, Addison-Wesley (1991).

[9] A. A. Abrikosov, *On the magnetic properties of superconductors of the second group*, Soviet Physics JETP **5**, 1174 (1957).

[10] M. Tinkham, *Introduction to Superconductivity*, 2nd. ed., McGraw Hill, (1996).

[11] C. A. Murray, P. L. Gammel, D. J. Bishop, D. B. Mitzi and A. Kapitulnik, *Observation of a hexatic vortex glass in flux lattices of the high-Tc superconductor* $Bi_{2.1}Sr_{1.9}Ca_{0.9}Cu_2O_{8+\delta}$, Phys. Rev. Lett. **64**, 2312 (1990).

[12] Z. Hao, J. R. Clem, M. W. McElfresh, L. Civale, A. P. Malozemoff, and F. Holtzberg, *Model for the reversible magnetization of high-κ type-II superconductors: Application to high-T_c superconductors*, Phys. Rev. B **43**, 2844 (1991).

[13] C. P. Bean and J. D. Livingston, *Surface barrier in type-II superconductors*, Phys. Rev. Lett. **12**, 14 (1964).

[14] E. Zeldov, A. I. Larkin, V. B. Geshkenbein, M. Konczykowski, D. Majer, B. Khaykovich, V. M. Vinokur, and H. Shtrikman, *Geometrical barriers in high-temperature superconductors*, Phys. Rev. Lett. **73**, 1428 (1994).

[15] E. H. Brandt, *Geometric barrier and current string in type-II superconductors obtained from continuum electrodynamics*, Phys. Rev. B **59**, 3369 (1999)

[16] E.H. Brandt, *Irreversibility in type-II superconductors: geometric barrier versus pinning*, Physica C, **341-348**, 1061 (2000).

[17] J. R. Clem, Chapter "*Magnetic flux penetration into the high temperature superconductors*", *«Physics and Materials Science of Vortex States, Flux Pinning and Dynamics»*, edited by Ram Kossowsky, Shyamalendu Bose, Vladimir Pan, and Zafer Durusoy, NATO Science Series E, Vol. **356**, (1999).

[18] D. T. Fuchs, E. Zeldov, M. Rappaport, T. Tamegai, S. Ooi and H. Shtrikman, *Transport properties governed by surface barriers in* $Bi_2Sr_2CaCu_2O_8$, Nature **391**, 373 (1998).

[19] J. Bardeen and M. J. Stephen, *Theory of the motion of vortices in superconductors*, Phys. Rev. **140**, A1197 (1965).

[20] C. P. Bean, *Magnetization of high-field superconductors*, Rev. Mod. Phys. **36**, 31 (1964).

[21] E. Zeldov, J. R. Clem, M. McElfresh and M. Darwin, *Magnetization and transport currents in thin superconducting films*, Phys. Rev. B **49**, 9802 (1994).

[22] C. J. van der Beek, M. Konczykowski, A. V. Samoilov, N. Chikumoto, S. Bouffard, and M. V. Feigel'man, *Defect-unbinding and the Bose-glass transition in layered superconductors*, Phys. Rev. Lett. **86**, 5136 (2001).

[23] S. Colson, M. Konczykowski, M. B. Gaifullin, Y. Matsuda, P. Gierlowski, M. Li, P. H. Kes, and C. J. van der Beek, *Vortex fluctuations in underdoped* $Bi_2Sr_2CaCu_2O_{8+\delta}$ *crystals*, Phys. Rev. Lett. **90**, 137002 (2003).

[24] E. Zeldov, D. Majer, M. Konczykowski, V. B. Geshkenbein, V. M. Vinokur and H. Shtrikman, *Thermodynamic observation of first-order vortex-lattice melting transition in* $Bi_2Sr_2CaCu_2O_8$, Nature **375**, 373 (1995).

[25] A. Schilling, R. A. Fisher, N. E. Phillips, U. Welp, D. Dasgupta, W. K. Kwok and G. W. Crabtree, *Calorimetric measurement of the latent heat of vortex-lattice melting in untwinned* $YBa_2Cu_3O_{7-\delta}$, Nature **382**, 7913 (1996).

[26] N. Chikumoto, M. Konczykowski, N. Motohira, and A. P. Malozemoff, *Flux-creep crossover and relaxation over surface barriers in* $Bi_2Sr_2CaCu_2O_8$ *crystals*, Phys. Rev. Lett. **69**, 1260 (1992).

[27] C. J. van der Beek, S. Colson, M. V. Indenbom, and M. Konczykowski, *Supercooling of the disordered vortex lattice in* $Bi_2Sr_2CaCu_2O_{8+\delta}$, Phys. Rev. Lett. **84**, 4196 (2000).

[28] N. Avraham, B. Khaykovich, Y. Myasoedov, M. Rappaport, H. Shtrikman, D. E. Feldman, T. Tamegai, Peter H. Kes, M. Li, M. Konczykowski, C. J. van der Beek and E. Zeldov, *Inverse melting of a vortex lattice*, Nature **411**, 451 (2001).

[29] P. Gammel, *Condensed-matter physics: why vortices matter?*, Nature **411**, 434 (2001).

[30] C. Jooss, J. Albrecht, H. Kuhn, S. Leonhardt and H. Kronmüller, *Magneto-optical studies of current distributions in high-*T_c *superconductors*, Rep. Prog. Phys. **65**, 651 (2002).

[31] C. J. van der Beek, J. Losco, M. Konczykowski, Patrick Pari, Takasada Shibauchi, Hiroaki Shishido and Yuji Matsuda, *Magneto-optical imaging of exotic superconductors*, J. Phys.: Conf. Ser. **150** 012052 (2009).

[32] M. C. Marchetti and D. R. Nelson, *Vortex physics in confined geometries*, Physica C **330**, 105 (2000).

[33] J. Larmor, *On the origin of magneto-optic rotation*, Nature **59**, 597 (1899).

[34] Rinke J. Wijngaarden, K. Heeck, M. Welling, R. Limburg, and M. Pannetier, K. van Zetten, V. L. G. Roorda, and A. R. Voorwinden, *Fast imaging polarimeter for magneto-optical investigations*, Rev. Sci. Instrum. **72**, 2661 (2001).

[35] S. Flament, Warsito, D. Bloyet, C. Cordier, L. Méchin and C. Gunther, *Magneto optical imaging of vortex penetration in patterned YBCO thin film near* T_c, Proceedings of NATO Advanced Research Workshop on "Magneto-Optical Imaging", Norway, published in NATO Science Series, Kluwer Academic Publishers (2003).

[36] A. Soibel, E. Zeldov, M. L. Rappaport, Y. Myasoedov, T. Tamegai, S. Ooi, M. Konczykowski and V. B. Geshkenbein, *Imaging the vortex-lattice melting process in the presence of disorder*, Nature **406**, 282 (2000).

[37] A. Soibel, Y. Myasoedov, M. L. Rappaport, T. Tamegai, S. S. Banerjee, and E. Zeldov, *Temperature variations of the disorder-induced vortex-lattice-melting landscape*, Phys. Rev. Lett. **87**, 167001 (2001).

[38] A. Soibel, Ph. D. thesis, *Visualization of vortex-lattice melting transition and transport current flow in $Bi_2Sr_2CaCu_2O_8$ with differential magneto-optical technique*, Weizmann Institute of Science, Israel (2001).

[39] J. Johnson, *Thermal agitation of electricity in conductors*, Phys. Rev. **32**, 97 (1928).

[40] H. Nyquist, *Thermal agitation of electric charge in conductors*, Phys. Rev. **32**, 110 (1928).

[41] K. Ishida, H. Mukuda, Y. Kitaoka, K. Asayama, Z. Q. Mao, Y. Mori and Y. Maeno, *Spin-triplet superconductivity in Sr_2RuO_4 identified by ^{17}O Knight shift*, Nature **396**, 658 (1998).

[42] N. J. Curro, T. Caldwell, E. D. Bauer, L. A. Morales, M. J. Graf, Y. Bang, A. V. Balatsky, J. D. Thompson and J. L. Sarrao, *Unconventional superconductivity in $PuCoGa_5$*, Nature **434**, 622 (2005).

[43] M. Takigawa, P. C. Hammel, R. H. Heffner, and Z. Fisk, *Spin susceptibility in superconducting $YBa_2Cu_3O_7$ from ^{63}Cu Knight shift*, Phys. Rev. B **39**, 7371 (1989).

[44] S. E. Barrett, D. J. Durand, C. H. Pennington, C. P. Slichter, T. A. Friedmann, J. P. Rice, and D. M. Ginsberg, *^{63}Cu Knight shifts in the superconducting state of $YBa_2Cu_3O_{7-\delta}$ (T_c = 90 K)*, Phys. Rev. B **41**, 6283 (1990).

[45] S. E. Barrett, J. A. Martindale, D. J. Durand, C. H. Pennington, C. P. Slichter, T. A. Friedmann, J. P. Rice, and D. M. Ginsberg, *Anomalous behavior of nuclear spin-lattice relaxation rates in $YBa_2Cu_3O_7$ below T_c*, Phys. Rev. Lett. **66**, 108 (1991).

[46] G. E. Volovik, *Superconductivity with lines of gap nodes: density of states in the vortex*, Pis'ma Zh. Eksp. Teor. Fiz. **58**, 457 (1993).

[47] C. J. van der Beek, V. B. Geshkenbein, and V. M. Vinokur, *Linear and nonlinear ac response in the superconducting mixed state*, Phys. Rev. B **48**, 3393 (1993).

[48] L. Fàbrega, J. Fontcuberta, S. Piñol, C. J. van der Beek, and P. H. Kes, *ac response of the vortex system in a $Pr_{1.85}Ce_{0.15}CuO_{4-y}$ single crystal*, Phys. Rev. B **47**, 15250 (1993).

[49] B. Dabrowski, K. Zhang, J. J. Pluth, J. L. Wagner and D. G. Hinks, *Single-crystal growth and characterization of $YBa_2Cu_4O_8$ with $T_c \approx 80$ K*, Physica C **202**, 271 (1992).

[50] Rinke J. Wijngaarden, H. J. Spoelder, R. Surdeanu and R. Griessen, *Determination of two-dimensional current patterns in flat superconductors from magneto-optical measurements: an efficient inversion scheme*, Phys. Rev. B **54**, 6742 (1996).

[51] T. H. Johansen, M. Baziljevich, H. Bratsberg, Y. Galperin, P. E. Lindelof, Y. Shen and P. Vase, *Direct observation of the current distribution in thin superconducting strips using magneto-optic imaging*, Phys. Rev. B **54**, 16264 (1996).

[52] G. P. Mikitik, E. H. Brandt, and M. Indenbom, *Superconducting strip in an oblique magnetic field*, Phys. Rev. B **70**, 014520 (2004).

[53] D. G. Gheorghe, M. Menghini, R. J. Wijngaarden, E. H. Brandt, G. P. Mikitik, and W. Goldacker, *Flux penetration into superconducting Nb_3Sn in oblique magnetic fields*, Phys. Rev. B **73**, 224512 (2006).

[54] D. T. Fuchs, E. Zeldov, M. Rappaport, T. Tamegai, S. Ooi and H. Shtrikman, *Transport properties governed by surface barriers in $Bi_2Sr_2CaCu_2O_8$*, Nature **391**, 373 (1998).

[55] M. Chiao, R. W. Hill, C. Lupien, B. Popić, R. Gagnon, and L. Taillefer, *Quasiparticle Transport in the Vortex State of $YBa_2Cu_3O_{6.9}$*, Phys. Rev. Lett. **82**, 2943 (1999).

[56] Y. Matsuda (private communication).

[57] C. Kallin and A.J. Berlinsky, *Is Sr_2RuO_4 a chiral p-wave superconductor?*, J. Phys.: Condens. Matter **21**, 164210 (2009).

[58] C. C. Tsuei, J. R. Kirtley, C. C. Chi, Lock See Yu-Jahnes, A. Gupta, T. Shaw, J. Z. Sun, and M. B. Ketchen, *Pairing symmetry and flux quantization in a tricrystal superconducting ring of $YBa_2Cu_3O_{7-\delta}$*, Phys. Rev. Lett. **73**, 593 (1994).

[59] H. Safar, P. L. Gammel, D. A. Huse, D. J. Bishop, J. P. Rice and D. M. Ginsberg, *Experimental evidence for a first-order vortex-lattice-melting transition in untwinned, single crystal $YBa_2Cu_3O_7$*, Phys. Rev. Lett. **69**, 824 (1992).

[60] W. K. Kwok, S. Fleshler, U. Welp, V. M. Vinokur, J. Downey, G. W. Crabtree, and M. M. Miller, *Vortex lattice melting in untwinned and twinned single crystals of $YBa_2Cu_3O_{7-\delta}$*, Phys. Rev. Lett. **69**, 3370 (1992).

[61] H. Pastoriza, M. F. Goffman, A. Arribére, and F. de la Cruz, *First order phase transition at the irreversibility line of $Bi_2Sr_2CaCu_2O_8$*, Phys. Rev. Lett. **72**, 2951 (1994).

[62] U. Welp, J. A. Fendrich, W. K. Kwok, G. W. Crabtree, and B. W. Veal, *Thermodynamic Evidence for a Flux Line Lattice Melting Transition in $YBa_2Cu_3O_{7-\delta}$*, Phys. Rev. Lett. 76, 4809 (1996).

[63] P. Kim, Z. Yao, and C. M. Lieber, *Vortex lattice structure in $Bi_2Sr_2CaCu_2O_{8+\delta}$ at high temperatures*, Phys. Rev. Lett. **77**, 5118 (1996).

[64] R. Cubitt, E. M. Forgan, G. Yang, S. L. Lee, D. McK. Paul, H. A. Mook, M. Yethiraj, P. H. Kes, T. W. Li, A. A. Menovsky, Z. Tarnawski and K. Mortensen, *Direct observation of magnetic flux lattice melting and decomposition in the high-Tc superconductor $Bi_{2.15}Sr_{1.95}CaCu_2O_{8+x}$*, Nature **365**, 407 (1993).

[65] M. Roulin, A. Junod, and E. Walker, *Flux line lattice melting transition in $YBa_2Cu_3O_{6.94}$ observed in specific heat experiments*, Science, Vol. **273**, Issue 5279, 1210 (1996).

[66] D. T. Fuchs, E. Zeldov, D. Majer, R. A. Doyle, T. Tamegai, S. Ooi and M. Konczykowski, *Simultaneous resistivity onset and first-order vortex-lattice phase transition in $Bi_2Sr_2CaCu_2O_8$*, Phys. Rev. B **54**, R796 (1996).

[67] W. K. Kwok, J. Fendrich, S. Fleshler, U. Welp, J. Downey, and G. W. Crabtree, *Vortex liquid disorder and the first order melting transition in $YBa_2Cu_3O_{7-\delta}$* Phys. Rev. Lett. **72**, 1092 (1994).

[68] T. T. M. Palstra, B. Batlogg, L. F. Schneemeyer, and J. V. Waszczak, *Thermally Activated Dissipation in $Bi_{2.2}Sr_2Ca_{0.8}Cu_2O_{8+\delta}$*, Phys. Rev. Lett. 61, 1662 (1988).

[69] L. Fábrega, L. Fábrega, J. Fontcuberta, S. Piñol, C. J. van der Beek, and P. H. Kes, *Thermally activated flux motion in $Nd_{1.85}Ce_{0.15}CuO_{4-y}$*, Phys. Rev. B **46**, 11952 (1992).

[70] S. Colson, C. J. van der Beek, M. Konczykowski, M. B. Gaifullin, Y. Matsuda, P. Gierlowski, Ming Li, and P. H. Kes, *Vortex solid-liquid transition in $Bi_2Sr_2CaCu_2O_{8+\delta}$ with a high density of strong pins*, Phys. Rev. B **69**, 180510 (2004).

[71] D. Majer, E. Zeldov, and M. Konczykowski, *Separation of the irreversibility and melting lines in $Bi_2Sr_2CaCu_2O_8$ crystals*, Phys. Rev. Lett. **75**, 1166 (1995).

[72] H. Pastoriza and P. H. Kes, *Direct shear probe of vortex lattice melting in $Bi_2Sr_2CaCu_2O_8$ single crystals*, Phys. Rev. Lett. **75**, 3525 (1995).

[73] G. P. Mikitik and E. H. Brandt, *Effect of pinning on the vortex-lattice melting line in type-II superconductors*, Phys. Rev. B **68**, 054509 (2003).

[74] S. P. Obukhov and M. Rubinstein, *Topological glass transition in entangled flux state*, Phys. Rev. Lett. **65**, 1279 (1990).

[75] D. R. Nelson and B. I. Halperin, *Dislocation-mediated melting in two dimensions*, Phys. Rev. B **19**, 2457 (1979).

[76] M. H. Theunissen, E. Van der Drift and P. H. Kes, *Size effects in flow of flux-line solids and liquids*, Phys. Rev. Lett. **77**, 159 (1996).

[77] M. Konczykowski and J. Gilchrist, *AC screening measurement for the characterization of ceramic superconductors: II. Electron irradiation effect on $YBa_2Cu_3O_7$*, Physica C, Vol. **168**, 131 (1990).

[78] M. Konczykowski, F. Rullier-Albenque, E. R. Yacoby, A. Shaulov, Y. Yeshurun, and P. Lejay, *Effect of 5.3-GeV Pb-ion irradiation on irreversible magnetization in Y-Ba-Cu-O crystals*, Phys. Rev. B **44**, 7167 (1991).

[79] M. Konczykowski, V. M. Vinokur, F. Rullier-Albenque, Y. Yeshurun, and F. Holtzberg, *Observation of flux creep through columnar defects in $YBa_2Cu_3O_7$ crystals*, Phys. Rev. B **47**, 5531 (1993).

[80] B. Khaykovich, M. Konczykowski, E. Zeldov, R. A. Doyle, D. Majer, P. H. Kes, and T. W. Li, *Vortex-matter phase transitions in $Bi_2Sr_2CaCu_2O_8$: effects of weak disorder*, Phys. Rev. B **56**, R517 (1997).

[81] J. A. Fendrich, W. K. Kwok, J. Giapintzakis, C. J. van der Beek, V. M. Vinokur, S. Fleshler, U. Welp, H. K. Viswanathan, and G. W. Crabtree, *Vortex liquid state in an electron irradiated untwinned $YBa_2Cu_3O_{7-\delta}$ crystal*, Phys. Rev. Lett. **74**, 1210 (1995).

[82] M. Konczykowski, C. J. van der Beek, A. E. Koshelev, V. Mosser, M. Li, and P. H. Kes, *Vortex matter of $Bi_2Sr_2CaCu_2O_8$ in the presence of pointlike disorder*, edited in Low Temperature Physics LT25 (2008).

[83] M. Menghini, Yanina Fasano, F. de la Cruz, S. S. Banerjee, Y. Myasoedov, E. Zeldov, C. J. van der Beek, M. Konczykowski, and T. Tamegai, *First-order phase transition from the vortex liquid to an amorphous solid*, Phys. Rev. Lett. **90**, 147001 (2003).

[84] S. S. Banerjee, A. Soibel, Y. Myasoedov, M. Rappaport, E. Zeldov, M. Menghini, Y. Fasano, F. de la Cruz, C. J. van der Beek, M. Konczykowski, and T. Tamegai, *Melting of porous vortex matter*, Phys. Rev. Lett. **90**, 087004 (2003).

[85] C. J. van der Beek, M. Konczykowski, V. M. Vinokur, T. W. Li, P. H. Kes, and G. W. Crabtree, *Vortex line pinning and Bose-glass dynamics in heavy-ion irradiated $Bi_2Sr_2CaCu_2O_{8+\delta}$ single crystals*, Phys. Rev. Lett. **74**, 1214 (1995).

[86] C. J. van der Beek, M. Konczykowski, V. M. Vinokur, G. W. Crabtree, T. W. Li, and P. H. Kes, *Vortex dynamics in a $Bi_2Sr_2CaCu_2O_8$ crystal with columnar defects*, Phys. Rev. B **51**, 15492 (1995).

[87] W. S. Seow, R. A. Doyle, A. M. Campbell, G. Balakrishnan, D. McK. Paul, K. Kadowaki, and G. Wirth, *Influence of columnar defects on vortex dynamics in $Bi_2Sr_2CaCu_2O_8$ from out-of-plane and flux transformer transport measurements*, Phys. Rev. B **53**, 14611 (1996).

[88] F. Rullier-Albenque, A. Legris, H. Berger and L. Forro, *Effect of electron irradiation in $Bi_2Sr_2CaCu_2O_8$ and $Bi_2Sr_2CuO_6$ superconductors*, Physica C, Vol. **254**, 88 (1995).

[89] T. Giamarchi and P. Le Doussal, *Elastic theory of flux lattices in the presence of weak disorder*, Phys. Rev. B **52**, 1242 (1995).

[90] T. Klein, I. Joumard, S. Blanchard, J. Marcus, R. Cubitt, T. Giamarchi and P. Le Doussal, *A Bragg glass phase in the vortex lattice of a type II superconductor*, Nature **413**, 404 (2001).

[91] D. Bourgault, D. Groult, S. Bouffard, J. Provost, F. Studer, N. Nguyen, B. Raveau, and M. Toulemonde, *Modifications of the physical properties of the high-Tc superconductors $YBa_2Cu_3O_{7-\delta}$ ($0.1 \leq \delta \leq 0.7$) by 3.5-GeV xenon ion bombardment*, Phys. Rev. B **39**, 6549 (1989).

[92] M. Leghissa, L. A. Gurevich, M. Kraus, G. Saemann-Ischenko, and L. Ya. Vinnikov, *Observation of a disordered vortex state in $Bi_2Sr_2CaCu_2O_{8+x}$ single crystals containing columnar defects*, Phys. Rev. B **48**, 1341 (1993).

[93] A. Legris, F. Rullier-Albenque, and P. Lejay, *Influence of columnar pins on the transport properties of $YBa_2Cu_3O_7$ single crystals*, Phys. Rev. B **48**, 10634 (1993).

[94] C. J. van der Beek, M. Konczykowski, T. W. Li, P. H. Kes, and W. Benoit, *Large effect of columnar defects on the thermodynamic properties of $Bi_2Sr_2CaCu_2O_8$ single crystals*, Phys. Rev. B **54**, R792 (1996).

[95] C. J. van der Beek, M. Konczykowski, R. J. Drost, P. H. Kes, N. Chikumoto, and S. Bouffard, *Entropy, vortex interactions, and the phase diagram of heavy-ion-irradiated $Bi_2Sr_2CaCu_2O_{8+\delta}$*, Phys. Rev. B **61**, 4259 (2000).

[96] D. R. Nelson and V. M. Vinokur, *Boson localization and pinning by correlated disorder in high-temperature superconductors*, Phys. Rev. Lett. **68**, 2398 (1992).

[97] A. I. Larkin and V. M. Vinokur, *Bose and vortex glasses in high temperature superconductors*, Phys. Rev. Lett. **75**, 4666 (1995).

[98] M. Konczykowski, C. J. van der Beek, E. Zeldov, Ming Li and P. H. Kes, *Persistence of the intrinsic transition in the vortex matter of disordered BSCCO:2212 crystals*, Physica C, Volumes **408-410**, 547 (2004).

[99] L. I. Glazman and A. E. Koshelev, *Thermal fluctuations and phase transitions in the vortex state of a layered superconductor*, Phys. Rev. B **43**, 2835 (1991).

[100] A. I. Larkin and Yu. N. Ovchinnikov, *Pinning in type II superconductors*, Journal of Low Temperature Physics **34**, 409 (1979).

[101] C. J. van der Beek, S. Colson, M. Konczykowski, M. V. Indenbom, R. J. Drost and P. H. Kes, *Magnetic relaxation in the Bragg-glass phase in BSCCO*, Physica C, Vol. **341-348**, 1279 (2000).

[102] M. V. Feigelman, V. B. Geshkenbein, A. I. Larkin, and V. M. Vinokur, *Theory of collective flux creep*, Phys. Rev. Lett. **63**, 2303 (1989).

[103] D. S. Fisher, M. P. Fisher, and D. A. Huse, *Thermal fluctuations, quenched disorder, phase transitions, and transport in type-II superconductors*, Phys. Rev. B **43**, 130 (1991).

[104] P. Le Doussal and T. Giamarchi, *Moving glass theory of driven lattices with disorder*, Phys. Rev. B **57**, 11356 (1998).

[105] D. T. Fuchs, E. Zeldov, T. Tamegai, S. Ooi, M. Rappaport, and H. Shtrikman, *Possible new vortex matter phases in* $Bi_2Sr_2CaCu_2O_8$, Phys. Rev. Lett. **80**, 4971 (1998).

[106] I. Joumard, T. Klein, and J. Marcus, *Evidence for diverging barriers in the disordered vortex solid in the* $(K,Ba)BiO_3$ *superconducting oxide*, Phys. Rev. Lett. **87**, 167002 (2001).

[107] J. Kierfeld, H. Nordborg, and V. M. Vinokur, *Theory of plastic vortex creep*, Phys. Rev. Lett. **85**, 4948 (2000).

[108] E. J. Kramer, *Microscopic and molecular fundamentals of crazing*, Advances in Polymer Science 52/53, Crazing in Polymers, Spring-Verlag, Berlin (1983).

[109] M. C. Marchetti and D. R. Nelson, *Patterned geometries and hydrodynamics at the vortex Bose glass transition*, Phys. Rev. B **59**, 13624 (1999).

[110] A. Pruymboom, P. H. Kes, E. van der Drift, and S. Radelaar, *Flux-line shear through narrow constraints in superconducting films*, Phys. Rev. Lett. **60**, 1430 (1988).

[111] D. R. Nelson, *Defects and geometry in condensed matter physics*, Cambridge University Press, (2002).

[112] N. Kokubo, T. G. Sorop, R. Besseling, and P. H. Kes, *Vortex-slip transitions in superconducting* $\alpha - NbGe$ *mesoscopic channels*, Phys. Rev. B **73**, 224514 (2006).

[113] A. P. Young, *Melting and the vector Coulomb gas in two dimensions*, Phys. Rev. B **19**, 1855 (1979).

[114] J. M. Kosterlitz and D. J. Thouless, *Ordering, metastability and phase transitions in two-dimensional systems*, Journal of Physics C: Solid State Physics, Vol. **6**, 1181 (1973).

[115] A. Zippelius, B. I. Halperin, and D. R. Nelson, *Dynamics of two-dimensional melting*, Phys. Rev. B **22**, 2514 (1980).

[116] S. A. Grigera, E. Morré, E. Osquiguil, C. Balseiro, G. Nieva and F. de la Cruz, *Bose-glass phase in twinned* $YBa_2Cu_3O_{7-\delta}$, Phys. Rev. Lett. **81**, 2348 (1998).

[117] D. T. Fuchs, R. A. Doyle, E. Zeldov, S. F. W. R. Rycroft, T. Tamegai, S. Ooi, M. L. Rappaport and Y. Myasoedov, *Transport properties of* $Bi_2Sr_2CaCu_2O_8$ *crystals with and without surface barriers*, Phys. Rev. Lett. **81**, 3944 (1998).

[118] T. W. Li, P. H. Kes, N. T. Hien, J. J. M. Franseb and A. A. Menovskyb, *Growth of* $Bi_2Sr_2CaCu_2O_{8+x}$ *single-crystals at different oxygen ambient pressures*, J. Cryst. Growth **135**, 481 (1994).

[119] M. Li, C. J. van der Beek, M. Konczykowski, H. W. Zandbergen, and P. H. Kes, *Self-doping caused by oxygen displacements in heavy-ion-irradiated* $Bi_2Sr_2CaCu_2O_{8+x}$ *crystals*, Phys. Rev. B **66**, 014535 (2002).

[120] J. F. Ziegler, J. P. Biersack and U. Littmark, *The Stopping and Range of Ions in Matter*, Vol. **1**, Pergamon Press, New York, (1985).

[121] A. E. Pashitski, A. Gurevich, A. A. Polyanskii, D. C. Larbalestier, A. Goyal, E. D. Specht, D. M. Kroeger, J. A. DeLuca and J. E. Tkaczyk, *Reconstruction of current flow and imaging of current-limiting defects in polycrystalline superconducting films*, Science, Vol. **275**, 367 (1997).

[122] N. Avraham, E. H. Brandt, G. P. Mikitik, Y. Myasoedov, M. Rappaport, E. Zeldov, C. J. van der Beek, M. Konczykowski, and T. Tamegai, *Influence of spatial variations in the lower critical field on the equilibrium field penetration into superconductors*, Phys. Rev. B **77**, 214525 (2008).

[123] M. Li, P. H. Kes, S. F. W. R. Rycroft, C. J. van der Beek and M. Konczykowski, *Origin of linear extended defects in single crystalline $Bi_2Sr_2CaCu_2O_8$*, Physica C, Vol. **408-410**, 25 (2004).

[124] S. F. W. R. Rycroft, R. A. Doyle, D. T. Fuchs, E. Zeldov, R. J. Drost, P. H. Kes, T. Tamegai, S. Ooi and D. T. Foord, *Bulk transport properties of $Bi_2Sr_2CaCu_2O_8$ crystals in the Corbino disk geometry*, Phys. Rev. B **60**, R757 (1999).

[125] A. Mazilu, H. Safar and D. López, *Experimental comparison of the effect that bulk pinning and surface barriers have on vortex motion in the vortex liquid state of $Bi_2Sr_2CaCu_2O_8$ single crystals*, Phys. Rev. B **58**, R8913 (1998).

[126] D. López, E. F. Righi, G. Nieva, and F. de la Cruz, *Coincidence of vortex-lattice melting and loss of vortex correlation along the c direction in untwinned $YBa_2Cu_3O_{7-\delta}$ single crystals*, Phys. Rev. Lett. **76**, 4034 (1996).

[127] B. Khaykovich, D. T. Fuchs, K. Teitelbaum, Y. Myasoedov, E. Zeldov, T. Tamegai, S. Ooi, M. Konczykowski, R. A. Doyle, and S. F. Rycroft, *Shear-induced vortex decoupling in $Bi_2Sr_2CaCu_2O_8$ crystals*, Phys. Rev. B **61**, R9261 (2000).

[128] B. Khaykovich, E. Zeldov, D. Majer, T. W. Li, P. H. Kes, and M. Konczykowski, *Vortex-lattice phase transitions in $Bi_2Sr_2CaCu_2O_8$ crystals with different oxygen stoichiometry*, Phys. Rev. Lett. **76**, 2555 (1996).

[129] A. F. Hebard and A. T. Fiory, *Critical-exponent measurements of a two-dimentional superconductor*, Phys. Rev. Lett. **50**, 1603 (1983).

[130] P. Berghuis, A. L. F. van der Slot, and P. H. Kes, *Dislocation-mediated vortex-lattice melting in thin films of $\alpha - Nb_3Ge$*, Phys. Rev. Lett. **65**, 2583 (1990).

[131] D. López, E. F. Righi, G. Nieva, F. de la Cruz, W. K. Kwok, J. A. Fendrich, G. W. Crabtree and L. Paulius, *Amplification of the c-axis vortex correlation by twin-boundary pinning at the vortex liquid-solid phase transition*, Phys. Rev. B **53**, R8895 (1996).

[132] E. F. Righi, S. A. Grigera, D. López, G. Nieva, F. de la Cruz, L. Civale, G. Pasquini, and P. Levy, *Enhancement of c-axis vortex correlation by twin boundaries and columnar defects in $YBa_2Cu_3O_{7-\delta}$*, Phys. Rev. B **55**, 5663 (1997).

[133] C. J. van der Beek, M. V. Indenbom, V. Berseth, T. W. Li, and W. Benoit, *Onset of bulk pinning in BSCCO single crystals*, Journal of Low Temperature Physics, Volume **105**, Issue 3-4, 1047 (1996).

[134] C. P. Slichter, *Principles of Magnetic Resonance*, 3^{rd} Edition, Springer (1990).

[135] C. H. Townes, Conyers Herring, and W. D. Knight, *The effect of electronic paramagnetism on Nuclear Magnetic Resonance frequencies in metals*, Phys. Rev. **77**, 852 (1950).

[136] C. Kittel, *Introduction to Solid State Physics*, 7^{th} Edition, John Wilet & Sons, Inc. (1996).

[137] W. Pauli, *The connection between spin and statistics*, Phys. Rev. **58**, 716 (1940).

[138] A. Jánossy, T. Fehér, G. Oszlányi, and G. V. M. Williams, *Linear low temperature spin susceptibility in the underdoped high T_c superconductor Gd* : $YBa_2Cu_4O_8$, Phys. Rev. Lett. **79**, 2726 (1997).

[139] K. Yosida, *Paramagnetic susceptibility in superconductors*, Phys. Rev. **110**, 769 (1958).

[140] H. Won and K. Maki, *d-wave superconductor as a model of high-Tc superconductors*, Phys. Rev. B **49**, 1397 (1994).